Scuola Normale Superiore di Pisa

PhD Thesis

Black Hole Accretion in Primordial Galaxies

Relatore:
Prof. Andrea Ferrara

Candidata:
Maria Carmela Orofino

Contents

Abstract

Supermassive black holes (SMBHs) with masses up to $10^{10} M_{\odot}$ are thought to power the emission from quasars and Active Galactic Nuclei. Surprisingly, these extremely massive, compact objects are already in place within the first billion years from the Big Bang, or redshift $z \geq 6$. In addition, a tight relation between the stellar and central black hole mass in galaxies has been established locally. The SMBH origin, evolution and relation to the host galaxy are key open problems in modern cosmology and astrophysics. They are the main subject of this Thesis.

As far as the origin is concerned, the most natural idea considers SMBHs as the end-product of accretion and merging on black hole remnants of massive stars. We have examined this possibility showing that this hypothesis entails several theoretical difficulties. To this aim, we have followed the accretion history of a $100 M_{\odot}$ stellar BH hosted by a typical $z = 10$ galaxy down to $z = 6$. We analysed the growth under different conditions linked to the galaxy geometry and BH orbital parameters. We conclude that in all cases, the BH mass can increase at most by 30%, thus making stellar seeds unsuitable to explain the observed masses of SMBH. As a by-product of the study, we have estimated the cumulative X-ray emission from an early BH population and the total energy released in the intergalactic medium. Given the above low accretion rates, we conclude that the X-ray emission from accreting BHs is negligible with respect to that provided by X-ray binaries in the same galaxy. Although sub-dominant, the X-ray preheating of the intergalactic medium by early BHs might have left a specific signature, potentially detectable with SKA, on the HI 21cm line power spectrum.

The above results forced us to look for alternative SMBH formation processes. Thus, we explored the scenario in which SMBHs grow by merging of more massive seeds, directly formed through non-stellar channels. These theoretically predicted, massive ($10^4 - 10^6 M_{\odot}$) "direct collapse" seeds provide a head-start of the SMBH build-up and overcome the inefficient stellar BH accretion. Lacking an observational confirmation of the existence of these putative SMBH progenitors, we first assessed whether these ancestors can be detected by the Chandra

X-ray Observatory, and used the upper limits provided by current observations to constrain theoretical model parameters. For this purpose, we exploit a semi-analytical model to predict the number density of progenitors of a $z = 6.4$ SMBH, their accretion and the amount of obscuring material in their host galaxies. For each ancestor we computed its X-ray spectrum accounting for interstellar absorption and compared it with current observations. Faint progenitors are found to be luminous enough to be detected in the X-ray band of current surveys. Even accounting for a maximum obscuration effect, the number of detectable BHs is reduced at most by a factor of 2. In our simulated sample, observations of faint quasars are mainly limited by their very low active fraction (about 1%), which is the result of short, super-critical growth episodes. We suggest that to detect high-z SMBHs progenitors, large area surveys with shallower sensitivities, such as COSMOS Legacy and XMM-LSS+XXL, are to be preferred with respect to deep surveys probing smaller fields, such as Chandra Deep Field South.

The models discussed so far imply that massive black holes ($\approx 10^8 M_\odot$) must be present also in galaxies routinely observed in the Epoch of Reionization, such as the so-called Lyman Break Galaxies (LBG) at $z > 6$. This is an important point because the presence of a (faint) AGN in these systems might substantially alter their physical and observable properties. We addressed this question by combining our semi-analytical model with tight constraints from the 7 Ms Chandra survey, and the known high-z SMBH population. Depending on the fraction of early halos planted with a BH direct collapse seed, the model suggests two possible scenarios: (a) if a maximal seeding occurs, massive BH in LBGs mostly grow by merging and must accrete at a low Eddington ratio not to exceed the experimental X-ray luminosity upper bound; (b) if the seeding is inefficient, direct accretion dominates and massive BH emission in LBGs must be heavily obscured. Scenario (a) poses extremely challenging, and possibly unphysical, requirements on seeds formation. Scenario (b) entails testable implications on the physical properties of LBGs involving far-infrared luminosity, emission lines, and presence of outflows that we discuss in detail.

1 Brief Overview

The presence of bright quasars in high-redshift observations (Fan et al., 2006, Willott et al., 2007a, Mortlock et al., 2011, Jiang et al., 2015, Wu et al., 2015) is still puzzling. As their huge luminosity ($\approx 10^{46}$erg s^{-1}) and the hardness of their spectra rule out the stellar nature of their central engine, quasars are thought to be powered by accreting super-massive black holes (SMBH). However, additional questions about their origin are left unanswered. For example, assembling the mass $M = 2 \times 10^9 M_\odot$ deduced for the quasar ULAS J1120+0641 at z = 7.085 (corresponding to 770 million years after the Big Bang; Mortlock et al. 2011) requires a SMBH "seed" with mass larger than $400 M_\odot$, growing at the limit of the feasible accretion rate (the Eddington rate) for almost 13 billion years. Unfortunately, both these statements are uncomfortably demanding and not in good agreement with current estimates of the mass of first stars (Omukai et al., 2010, Greif et al., 2011, Bromm and Yoshida, 2011) and to theorized limits of BH accretion (Johnson and Bromm, 2007, Alvarez et al., 2009).

A wide span of scenarios have been explored theoretically, to provide reliable models of SMBH seed formation, growth and evolution (we refer to Volonteri, 2010a, Volonteri and Bellovary, 2012, Haiman, 2013, Latif and Ferrara, 2016a for review on this topic). Currently, the most accredited hypotheses are founded on the monolithic gravitational collapse of pristine atomic gas, leading to a single $10^{4-6} M_\odot$ direct-collapse black hole (DCBH). Although this process would be the most fitting solution to the problem (see Rees, 1984 and Ferrara et al., 2014a), there are not undeniable observations of DCBHs, albeit there have been controversial claims on the nature of CR7, the brightest Lyman-α emitter known (see Pallottini et al., 2015a, Bowler et al., 2017 and Dijkstra et al., 2016 for further discussions). Remnants of massive stars are the most natural way to gain a SMBH seed: their mass depend on several factors (Ciardi and Ferrara, 2005), but is in any case much lighter than $10^3 M_\odot$. A light seed experiences a modest accretion history and this scenario is highly disfavored if merger episodes and/or super-Eddington accretion do not occur.

This Thesis is organized as follows:

- **Chapter 2**: we illustrate the standard cosmological ΛCDM model and describe the basis of structure formation in the Universe.
- **Chapter 3**: we focus on the large scale structure, defining the dark matter halo mass function and showing that structure formation occurs hierarchically. We then introduce a semi-analytical model to approach statistically the growth history of dark matter halos.
- **Chapter 4**: we catalog active galactic nuclei, summarizing their main observational features and discussing the origin of their hard emission. Black holes physics is analysed in detail, with particular regard to the accretion process.
- **Chapter 5**: we deal with the nature and growth of SMBH seeds, their tentative detection and experimental constraints.
- **Chapter 6**: we present a model for quasar X-ray emission, accounting for absorption in the inter-stellar medium, due to Compton and photoelectric effect, and compare our results with current quasar observations.
- **Chapter 7**: we analysed the most favorable conditions for the growth of light SMBH seeds in a primordial galaxy and estimated BH impact on the intergalactic medium.
- **Chapter 8**: we exploit our semi-analytical model to explore the formation of SMBH by merging of smaller progenitors. We then discuss the best strategy for the detection of SMBH progenitors in current X-ray surveys.
- **Chapter 9**: we use our semi-analytical model to study the possible presence of massive black holes in high-redshift Lyman-Break Galaxies.
- **Chapter 10**: we conclude with brief summary of the method and the results obtained, considering the limitation of our works and the prospects for the near future.

Throughout this work, when not otherwise specified, we assume a flat Universe with the following cosmological parameters: $\Omega_{\rm M}h^2 = 0.142$, $\Omega_\Lambda = 1 - \Omega_{\rm M}$, and $\Omega_{\rm B}h^2 = 0.022$, $h = 0.674$, $\sigma_8 = 0.811$, where $\Omega_{\rm M}$, Ω_Λ, $\Omega_{\rm B}$ are the total matter, vacuum, and baryonic densities, in units of the critical density; h is the Hubble constant in units of $100\,{\rm km\,s^{-1}\ Mpc^{-1}}$, and σ_8 is the late-time fluctuation amplitude parameter (Planck Collaboration et al., 2018).

2 Cosmological Background

In this Chapter we introduce the cosmological standard model and the structure formation in our Universe. In Sec. 2.1, we introduce the *cosmological principle*, the basis of modern cosmology, and the Friedmann equations, that describe the dynamics of the Universe. In Sec. 2.2 we study the evolution of gravitational collapses and the virialization of dark matter halos.

2.1 The expanding Universe

Observations of distant galaxies highlight that they recede from us with a velocity v proportional to their distance d, according to the law:

$$v = H_0 d, \tag{2.1}$$

where the quantity H_0 is called *Hubble constant*. This equation describes the *Hubble law*, formalized by Erwin Hubble in 1929 and easily explained by General Relativity, which correlates the geometry of the Universe to its matter content.

In the following, we describe the kinematics (Sec. 2.1.1) and the dynamics (Sec. 2.1.2) of a homogeneous and isotropic Universe [1] and contextualize this work.

2.1.1 The cosmological principle

Modern cosmology is founded on the assertion that the Universe appears the same to all observers, regardless their individual locations. This statement is the *the cosmological principle* and generalises the Copernican principle, implying that the Universe is homogeneous and isotropic. In General Relativity, three metrics only describe a homogeneous and isotropic Universe: the Robertson and Walker metrics,

$$ds^2 = c^2 dt^2 - a^2(t) \left(\frac{dx^2}{1 - kx^2} + x^2 (d\theta^2 + \sin^2 \theta d\phi^2) \right), \tag{2.2}$$

[1] this approximation is excellent on large scales and clearly fails on small ones

where x, θ, ϕ and t are spatial and temporal coordinates, ds is the differential line element, $a(t)$ is an overall scale factor describing the expansion of the spatial coordinates in time and k is the scalar curvature, which determines space geometry. In particular k can takes values -1 (corresponding to an open universe), 0 (flat), +1 (close): current observations support the statement that the Universe is flat and in this work we consider $k = 0$. Eq. (2.2) adopts comoving coordinates x, θ, ϕ, that are fixed in absence of peculiar motion. Due to expansion of the Universe, the corresponding physical (or *proper*) coordinates are $\vec{r}(t) = a(t)\vec{x}$ and are time dependent even in absence of peculiar motion.

The metric in Eq. (2.2) leads to interesting insights about light propagation. Examine a light ray emitted by a source at a time t_e and received by an observer at a time t_o in one spatial dimension ($d\theta = d\phi = 0$); since light rays have null geodesics ($ds^2 = 0$), $cdt = -a(t)dx$, the - sign accounting for the fact that light travels towards the observer. Time-interval between the wave fronts is Δt_e at the emission and Δt_o at the detection and the distance x travelled by the fronts must be the same:

$$x = \int dx = -\int_{t_e}^{t_o} \frac{cdt}{a(t)} = -\int_{t_e+\Delta t_e}^{t_o+\Delta t_o} \frac{cdt}{a(t)}, \tag{2.3}$$

that means:

$$\frac{\Delta t_o}{a(t_o)} = \frac{\Delta t_e}{a(t_e)} \tag{2.4}$$

and

$$\frac{a(t_o)}{a(t_e)} = \frac{\Delta t_o}{\Delta t_e} = \frac{\nu_e}{\nu_o} = 1 + z, \tag{2.5}$$

where ν is light frequency and $z = \frac{\nu_e - \nu_o}{\nu_o}$ is the redshift.

It is worth noting that Hubble law Eq. (2.1) states that the velocity v_i at which a galaxy i is moving away from us is proportional to its distance r_i from us: $v_i = H_0 r_i$ and velocity is the time derivative of the proper distance,

$$v_i = \frac{dr_i}{dt} = x_i \dot{a}(t)|_{t=t_0} = r_i \frac{\dot{a}(t_0)}{a(t_0)}, \tag{2.6}$$

giving $H_0 = \frac{\dot{a}(t_0)}{a(t_0)}$ or in general:

$$H = \frac{\dot{a}(t)}{a(t)}. \tag{2.7}$$

The time dependence of $a(t)$ also determines the flux f received by a source. We know that the luminosity (i.e. the power) emitted by a distant source is

diluted: because of the expansion of the Universe, the flux f does not obey to its usual x^{-2} dependence. Observing a light source with bolometric (i.e. emitted over the whole spectrum) luminosity L, at a comoving distance x:

- The geometry of the space-time modifies fluxes. However in a flat universe the surface involved in the calculation of the flux is the Euclidean $4\pi x^2$.
- The energy of the emitted photons redshifts in their travel:

$$h_p \nu_0 = \frac{h_p \nu_e}{1+z}. \tag{2.8}$$

- The arrival rate of the photons is stretched by $(1+z)$.

These statements mean that, for example, if a source at $z = 9$ from us emits 10 photons of energy 10 keV for unit time, we receive 1 photons of 1 keV in the same time interval. Given the bolometric luminosity L, the bolometric flux f_{bol} is:

$$f_{bol} = \frac{L}{4\pi x^2 (1+z)^2} = \frac{L}{4\pi d_L^2} \tag{2.9}$$

and the quantity $d_L = (1+z)x$ is known as *luminosity distance*. Similarly, if we consider the monocromatic flux f_ν, we get:

$$f_{\nu_0} = \frac{L_{\nu_e}(1+z)}{4\pi d_L^2}, \tag{2.10}$$

due to the redshift of the frequency.

Also the angular size of a source at redshift z behaves interestingly. Due to Universe expansion, the angle θ under which a source is seen increases by a factor $(1+z)$:

$$\theta = \frac{S(1+z)}{x} = \frac{S}{D_\theta}, \tag{2.11}$$

where S is the proper diameter of the source, x the comoving distance and $D_\theta = x/(1+z)$ is the *angular size distance*.

As a consequence of Universe expansion, astronomical objects appear bigger and less luminous. Note that, luminosity distance and angular size distance are linked to each other and $d_L = (1+z)^2 D_\theta$.

2.1.2 The Friedmann equations

General Relativity is essential to comprehend evolution of the Universe and in particular the time dependence of the scale factor a. Within this theory, space-

time geometry is strongly correlated to matter distribution through Einstein field equations:

$$R_{\mu\nu} - \frac{1}{2} g_{\mu\nu} R = \frac{8\pi G}{c^4} T_{\mu\nu}, \tag{2.12}$$

that relate a set of symmetric 4×4 tensors: the Ricci curvature tensor $R_{\mu\nu}$, the metric tensor $g_{\mu\nu}$ and the stress - energy tensor $T_{\mu\nu}$. R, G and c are the scalar curvature, the gravitational constant and the speed of light respectively. On the one hand, read left-to-right, Einstein equations mean that space-time geometry is affected by matter. On the other hand (right-to-left) they imply that space-time geometry determines the matter dynamics.

Since Robertson and Walker metric (Eq. (2.2)) states homogeneity and isotropy of the Universe, Eqs. (2.12) imply two independent equations only, known as Friedmann equations:

$$H^2 = \left(\frac{\dot{a}(t)}{a(t)} \right)^2 = \frac{8\pi G}{3} \rho - \frac{kc^2}{a(t)}, \tag{2.13}$$

$$\ddot{a}(t) = -\frac{4\pi G}{3} a(t) \left(\rho + \frac{3P}{c^2} \right), \tag{2.14}$$

describing the Universe evolution in terms of $a(t)$; P and ρ are the pressure and the energy density of the fluid composing the Universe, respectively. In particular, there is a *critical density* ρ_c for which the Universe is flat ($k = 0$):

$$\rho_c = \frac{3H^2}{8\pi G} \tag{2.15}$$

and a Universe with $\rho > \rho_c$ would be closed ($k > 0$), one with $\rho < \rho_c$ would be open ($k < 0$).

The assumption of homogeneity and isotropy rules out any heat transfer and the energy is conserved. In a volume $V = V_0 a^3(t)$, for a perfect fluid with equation of state $P(\rho) = wc^2\rho$, energy conservation is

$$c^2 d(\rho V) = -P dV, \tag{2.16}$$

that implies:

$$\frac{d\rho}{\rho} = -3(1+w)\frac{da}{a} \Longrightarrow \rho \propto a^{-3(1+w)}. \tag{2.17}$$

The generic equation of state of a perfect fluid is described in terms of a dimensionless parameter $w = \frac{P}{\rho}$, that characterizes the specific nature of the fluid. To date, the most accredited cosmological model, the ΛCDM (Λ Cold Dark Matter) states the presence of four components in the cosmological fluid:

1. **Baryonic matter** - includes both baryons and leptons (excluding neutrinos) and constitutes 4.8% of the total, according to the last Planck collaboration release (Planck Collaboration et al., 2018). In the redshift range considered in this Thesis, baryonic matter is not in relativistic regime, so that its pressure is negligible ($w = 0$) and Eq. (2.17) yields:

$$\rho_b(z) = \rho_{b,0}(1+z)^3, \tag{2.18}$$

as could be guessed since the density of the ordinary matter is diluted by Universe expansion.

2. **Radiation and relativistic matter** - including photons and neutrinos, whose density is $\approx 10^{-5}\rho_{tot}$ at the present time. For radiation $P = \rho/3$ and Eq. (2.17) gives:

$$\rho_r(z) = \rho_{r,0}(1+z)^4, \tag{2.19}$$

since the photons are subjected to the same dilution as baryonic matter and, moreover, subjected to redshift.

3. **Dark matter (DM)** - constitutes 26% of the matter of the Universe. The nature of this component is unknown and had been theorized to account for observatiional evidences of galaxies' dynamics. There are several speculations on its essence; among them: weakly-interacting particles and primordial black holes. As in the baryonic component, its density is supposed to evolve as

$$\rho_{DM}(z) = \rho_{DM,0}(1+z)^3. \tag{2.20}$$

4. **Dark energy (DE)** - this exotic fluid accounts for the 68% of the energy of the Universe (Planck Collaboration et al., 2018) and is meant to be responsible for the accelerated expansion ($\ddot{a}(t) > 0$) of the Universe. As for the DM, its nature is still unknown. From Eq. (2.14) it is clearly deduced that DE requires a negative pressure, that leads to an equation of state with $w = -1$ and

$$\rho_{DE}(z) = \rho_{DE,0}. \tag{2.21}$$

An appropriate model for DE is achieved if a *cosmological constant*, Λ, is introduced in Einstein's Eqs. (2.12).

The different components of the density are usually described as fractions of the

critical density, defining the parameters:

$$\Omega_{X,0} \equiv \frac{\rho_{X,0}}{\rho_c}. \tag{2.22}$$

The ΛCDM model states that the Universe has undergone three main phases:

1. At $z > 3300$ the Universe was *radiation dominated (RD)*, being the main contribution to the total density given by radiation and relativistic matter.

2. For redshift $1 < z < 3300$ (a range that include totally the interval of interest in this Thesis) the Universe was *matter dominated (MD)*. In this case, assuming no-baryonic components to be negligible, Eq. (2.13) gives the solution $a(t) \propto t^{2/3}$.

3. At $z < 1$ the Universe is dominated by the cosmological constant Λ and its expansion is accelerating.

Once the $z-$evolution of the density is achieved for the various components, the $z-$dependence of the Hubble parameter H is obtained from Eq. (2.13):

$$H(z) = H_0[\Omega_{m,0}(1+z)^3 + \Omega_{rad,0}(1+z)^4 + \Omega_{DE,0} + (1-\Omega)(1+z)^2]^{1/2}, \tag{2.23}$$

where $\Omega = \Omega_{m,0} + \Omega_{rad,0} + \Omega_{DE,0}$. According to Eq. (2.23) , we show the $z-$evolution of H is shown in Fig. 2.1. $H(z)^{-1}$ is the timescale of the expansion of the Universe at each z: if the time scale of a certain physical process is higher than $H^{-1}(z)$ than the process is not relevant at that z.

Eq. (2.7) and (2.23) yield the time interval $\tau(z)$ that has elapsed since the Big Bang and the comoving distance $x(z)$ that separate us from a source, at a given z:

$$\tau(z) = \int_z^\infty \frac{dz'}{(1+z')H(z')}, \tag{2.24}$$

$$x(z) = \int_0^z \frac{cdz'}{H(z')}, \tag{2.25}$$

and Fig. 2.2 shows the redshift dependence of $t(z)$ and $x(z)$ according to Eqs. (2.24) and (2.25).

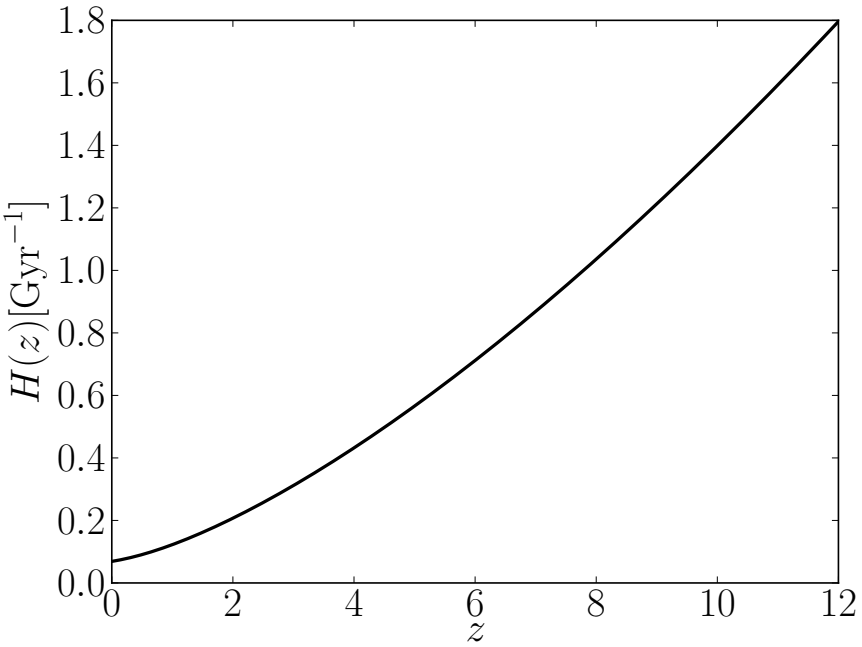

Figure 2.1: Hubble parameter as a function of redshift computed with the latest determination of $\Omega_{X,0}$ (Planck Collaboration et al., 2018).

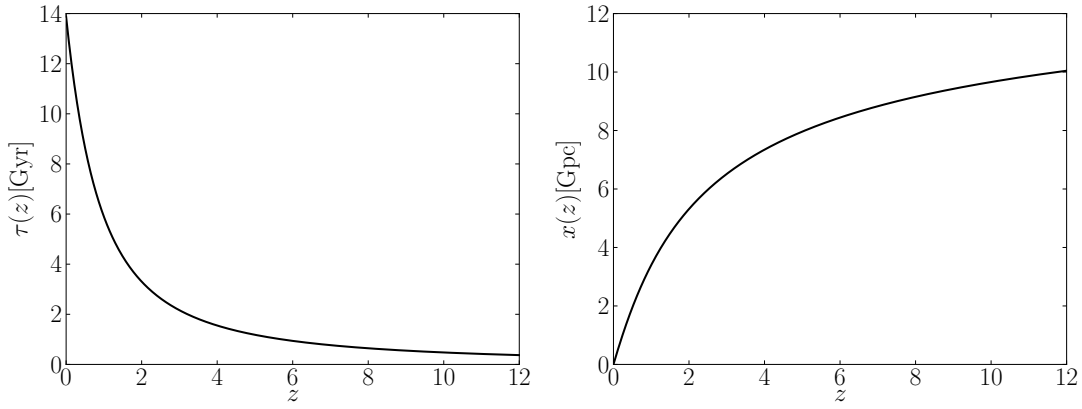

(a) Age of the universe **(b)** Comoving distance

Figure 2.2: *Left panel:* age of the Universe as a function of redshift z (Eq. (2.24)). *Right:* redshift evolution of the comoving distance from us (Eq. (2.25)).

2.2 Structure Formation

It is sufficient to compare the typical densities on the Earth ($\approx 1\,\mathrm{g\,cm^{-3}}$) and in the intergalactic medium ($\approx 10^{-30}\mathrm{g\,cm^{-3}}$) to comprehend that, at small scales, the assumption of a homogeneous and isotropic Universe, made in the previous Sec. 2.1, fails. Anyway, there is observational evidence that nearly four-hundred-thousand years after the Big Bang our Universe was almost homogeneous: the detection of a Cosmic Microwave Background (CMB) shows at that age only tiny density fluctuations (order of $\frac{\delta\rho}{\rho} \approx 10^{-5}$), widened with time due to gravitational instabilities and eventually collapsed to form large scale structures in local Universe.

In this Section we introduce structure formation, from the evolution of the first density perturbations in the linear regime (Sec. 2.2.1), to their growth in non-linear regime (Sec. 2.2.2), discussing the main characteristics of a collapsed object (Sec. 2.2.3).

2.2.1 Growth of linear perturbations

In this Section we analyse the linear evolution of density fluctuations. As discussed in Sec. 2.1, in high-z Universe the cosmological constant Λ can be neglected: we discuss the importance of Λ in Sec. 3.2, where we show that it suppresses the growth of perturbations. The fluctuation field is represented by the *overdensity* (or *contrast*) δ:

$$\delta(\mathbf{x},t) = \frac{\rho(\mathbf{x},t)}{\rho(t)} - 1 \ll 1. \tag{2.26}$$

Equations of classical fluidodynamics,

$$\begin{gathered}\left(\frac{\partial\rho}{\partial t}\right)_{\mathbf{r}} + \nabla_{\mathbf{r}}\cdot(\rho\mathbf{v}) = 0 \\ \left(\frac{\partial\mathbf{v}}{\partial t}\right)_{\mathbf{r}} + (\mathbf{v}\cdot\nabla_{\mathbf{r}})\mathbf{v} = -\frac{\nabla_{\mathbf{r}}P}{\rho} - \nabla\phi \\ \nabla^2_{\mathbf{r}}\phi = 4\pi G\rho,\end{gathered} \tag{2.27}$$

are suitable to describe fluctuations with

- wavelength λ smaller than the Hubble radius $\frac{c}{H}$,
- non-relativistic peculiar velocity $\mathbf{u}$.

The evolution of this system is due to the matter fluid dynamics on the one hand and to the expansion of the Universe on the other hand. To disentangle these two different aspects, we use comoving coordinates $\mathbf{x} = \mathbf{r}/a(t)$, where differential operators are:

$$\left(\frac{\partial f}{\partial t}\right)_{\mathbf{r}} = \frac{\partial f}{\partial t} - \frac{\dot{a}}{a}\mathbf{x}\cdot\nabla f \tag{2.28}$$
$$\nabla = a\nabla_{\mathbf{r}},$$

and divide the total velocity $\mathbf{v}$ as composition of expansion velocity and the fluid peculiar velocity: $\mathbf{v} = \dot{a}\mathbf{x} + \mathbf{u}$. The potential ϕ can be described as the composition of an unperturbed potential and perturbation $\delta\phi$:

$$\phi = \frac{2}{3}\pi G\bar{\rho}a^2\mathbf{x}^2 + \delta\phi \tag{2.29}$$

These description in terms of the overdensity, combined with the fluid equation of state $\nabla P = \frac{dP}{d\rho}\nabla\rho = c_s^2\bar{\rho}\nabla\delta$ (where c_s is the speed of sound in the fluid) yields a second order differential equation for δ, the Jeans equation:

$$\frac{\partial^2\delta}{\partial t^2} + 2\frac{\dot{a}}{a}\frac{\partial\delta}{\partial t} = 4\pi G\bar{\rho}\delta + \frac{c_s^2}{a^2}\nabla^2\delta. \tag{2.30}$$

Eq. (2.30) shows that fluctuations evolution is determined by two conflicting contributions of gravity and pressure. The term $\propto \frac{\dot{a}}{a}$ is a drag term due to Universe expansion, slowing down the perturbations growth. As explained in Sec. 2.1.2, in the matter dominated Universe the pressure term is negligible and $a(t) \propto t^{2/3}$, yielding:

$$\frac{\partial^2\delta}{\partial t^2} + \frac{4}{3t}\frac{\partial\delta}{\partial t} = \frac{2}{3t^2}\delta, \tag{2.31}$$

that has only one independent non-vanishing solution:

$$\delta \propto t^{2/3} \propto a(t). \tag{2.32}$$

As a consequence, in an Einstein-de Sitter Universe (i.e. both k and Λ are null), density contrast grows proportionally to a growth factor $D(z) = 1/(1+z)$ (in the next Sec. 3.2 (Eq. (3.11)) we show that this growth is in general more complicated). In Fourier Transform, Jeans Eq. (2.30) are easily solved:

$$\frac{\partial^2\delta_{\mathbf{k}}}{\partial t^2} + 2\frac{\dot{a}}{a}\frac{\partial\delta_{\mathbf{k}}}{\partial t} = \left(4\pi G\bar{\rho} - \frac{k^2c_s^2}{a^2}\right)\delta_{\mathbf{k}}; \tag{2.33}$$

the right term in Eq. (2.33) highlights a characteristic scale k_J (whose dimensions are the inverse of a length), such that a characteristic scale length λ_J (the Jeans length) can be defined,

$$\lambda_J = \frac{2\pi a}{k_J} = \left(\frac{\pi c_s^2}{G\overline{\rho}}\right)^{1/2}. \tag{2.34}$$

In particular, perturbations with wavelength $\lambda < \lambda_J$ do not collapse, since give oscillatory solutions of Eq. (2.33); on the contrary, perturbations characterized by $\lambda > \lambda_J$ collapse. Alternatively, a typical scale mass (Jeans mass) can be defined,

$$M_J = \frac{4\pi}{3}\overline{\rho}\lambda_J^3 = \frac{4\pi}{3}\left(\frac{\pi c_s^2}{G\overline{\rho}^{1/3}}\right)^{3/2} \tag{2.35}$$

such that the criterion for a perturbation to collapse is that its mass M has to overcome M_J.

The analysis on perturbation growth made so far, does not concern fluctuations on scales larger than the Hubble radius. Further calculations include general relativity and are far more complex: a complete description lies outside the goals of this Thesis and we present only the results from Padmanabhan, 1993 in Tab. 2.1. We only stress that in the radiation dominated epoch perturbations grow until they enter the Hubble radius and, in this phase, small scale perturbations are suppressed with respect to large scale ones.

Epoch	radiation	DM	baryons
$t < t_{\rm enter} < t_{\rm eq}$	$\propto a^2$	$\propto a^2$	$\propto a^2$
$t_{\rm enter} < t < t_{\rm eq}$	osc	$\propto \ln a$	osc
$t_{\rm eq} < t < t_{\rm dec}$	osc	$\propto a$	osc
$t_{\rm dec} < t$	osc	$\propto a$	$\propto a$

Table 2.1: Evolution of linear fluctuations at different epochs. $t_{\rm enter}$ is the time at which a fluctuation enter the Hubble radius, $t_{\rm eq}$ is the time at which transition between a radiation and a matter dominated universe occurs, $t_{\rm dec}$ is the time of decoupling of radiation and baryons.

2.2.2 Spherical collapse

When the overdensity $\delta \simeq 1$, the linear theory described in Sec. 2.2.1 is no longer suitable and given the complexity of the problem, a numerical approach is required in the general case. Here we limit to the special case of a perfectly spherical collapse and neglect the effect of the cosmological constant. We distinguish

the background density ρ_b and the initial overdensity $\bar{\delta}_i$ of the fluctuation,

$$\bar{\delta}_i = \frac{3}{4\pi r_i^3} \int_0^{r_i} 4\pi \delta_i(r) r^2 dr, \tag{2.36}$$

r_i being the initial size of the fluctuation. The final mass of the collapsed matter is

$$M = \rho_b \frac{4\pi}{3} r_i^3 (1 + \bar{\delta}_i). \tag{2.37}$$

For $r_i \ll c/H$ relativistic effects are negligible and the collapse is well described by with Newtonian gravity: the energy per unit mass of a point particle at the proper coordinate r is, then,

$$E = \frac{1}{2}\left(\frac{dr}{dt}\right)^2 - \frac{GM}{r}. \tag{2.38}$$

If $E \geq 0$ the system does not stop its expansion and does not collapse, if $E < 0$ there is a characteristic coordinate $r = r_{ta}$ (turn around point) in which the kinetic energy vanishes and the system contracts and collapses. E is the sum of kinetic K_i and potential U_i energy:

$$K_i = \frac{\dot{r}_i^2}{2} = \frac{H_i^2 r_i^2}{2} \tag{2.39}$$

$$U_i = \frac{GM}{r_i} = \frac{4\pi G}{3} \rho_b(t_i) r_i^2 (1 + \bar{\delta}_i) = K_i \Omega_i (1 + \bar{\delta}_i) \tag{2.40}$$

where $\Omega_i = \rho_b(t_i)/\rho_c(t_i)$ and H_i is Hubble constant at initial time. The condition for collapse is, then, $\bar{\delta}_i > (\Omega_i^{-1} - 1)$.

In the flat, matter-dominated universe $\Omega_i = 1$, $H_i t_i \approx 2/3$ and $\delta_i \propto t_i^{2/3}$ and all the overdense regions collapse. However, at low redshift[2] not all the overdense regions are collapsed, since the collapse time depends on the initial overdensity and tends to infinity for $\bar{\delta}_i \to 0$.

The solutions of the equations for collapse have parametric form:

$$r = A(1 - \cos\theta), \tag{2.41}$$

$$t = B(\theta - \sin\theta), \tag{2.42}$$

[2]It is worth to remember that the cosmological constant cannot be neglected at $z < 1$.

with:

$$A = \frac{3r_i}{10\bar{\delta}_i}, \tag{2.43}$$

$$B = \frac{3t_i}{4(5\bar{\delta}_i/3)^{3/2}}. \tag{2.44}$$

At $t \approx t_i$ the overdensity expands with the Hubble flow and, according to the previous equations, the expansion progressively slows, till it reaches the turn-around radius $r_{ta} = 2A$ at $t_{ta} = \pi B$. We assume that different fluid shells do not cross during the collapse, although this is no longer valid in the late phases of collapse, and identify $\theta = 2\pi$ as condition for collapse to occur. This is considered a good approximation, since leads to conclude that the collapse occur in a time $t_{coll} = 2t_{ta}$, when more refined models suggest that the structure is already virialized (Sec. 2.2.3). For future purposes, we evaluate the density contrast that linear theory predicts at the collapse time; since $\delta_l(t) = \delta_i a(t)/a(t_i) \approx \delta_i (t/t_i)^{2/3}$:

$$\delta_l(t_{ta}) = \delta_i \left(\frac{t_{t_a}}{t_i}\right)^{2/3} = 1.06 \tag{2.45}$$

$$\delta_l(t_{\rm coll}) = 2^{2/3}\delta_l(t_{\rm ta}) = 1.686. \tag{2.46}$$

We discuss these results in Sec. 3.2 since the Press-Schechter theory states that a region collapses once its overdensity reaches the amplitude $\delta_l(t_{\rm coll})$.

2.2.3 Virialized dark matter halos

In principle, a spherical symmetric region collapses to a point mass. Indeed, violent dynamical relaxation processes create an equilibrium called *virialization*. Virialized dark matter halos are the basic structures of galaxies, since baryons within these halos can collapse and form stars.

According to the *virial theorem*, all dynamically relaxed, self-gravitating structures obey to the virial theorem[3]:

$$2K + U = 0, \tag{2.47}$$

where K and U are, respectively, the kinetic and potential energy of the baryonic

[3] In this statement, the term relative to cosmological constant U_Λ is neglected.

matter (of mass M_{gas}) in a virialized halo of mass M and typical radius r_{vir}:

$$K = \frac{3}{2}\frac{M_{gas}}{\mu m_p}k_B T$$
$$U = -\frac{3}{5}\frac{GM_{gas}M}{r_{vir}}, \tag{2.48}$$

m_p is the proton mass, k_B is the Boltzmann constant, T and μ are the temperature and the molecular weight [4] of the gas. The virial theorem yields:

$$k_B T_{vir} = \frac{\mu m_p GM}{5r_{vir}}. \tag{2.49}$$

Note that, as calculated in the previous Sec. 2.2.2, the virial radius r_{vir} can be determined as one half of the turnaround radius. The overdensity of the virialized halo is $\Delta_c(z) = \frac{\rho_{vir}(z)}{\bar{\rho}(z)} \approx 178$. Eq. (2.49) yields the temperature of a virialized halo of mass M at redshift z:

$$T_{vir}(M,z) \approx 19800K \left(\frac{\mu}{0.6}\right)\left(\frac{M}{10^8 h^{-1}M_\odot}\right)^{2/3}\left(\frac{\Omega_{m,0}\Delta_c(z)}{18\pi^2}\right)^{1/3}\left(\frac{1+z}{10}\right). \tag{2.50}$$

[4] μ is strongly dependent on the ionization fraction of the gas. In particular, in a fully ionized primordial gas $\mu \approx 0.6$ and in a fully neutral primordial gas $\mu \approx 1.2$.

3 Large Scale Structure

In Chapter 2 we described the ΛCDM model, the collapse of gravitational instabilities and the virialization of dark matter halos. Here we present the large scale structures that we observe in our Universe, describing statistically the density fluctuations (Sec. 3.1), introducing the *halo mass function* (Sec. 3.2), a qualitative analysis of its features, useful applications and an extended theory (Sec. 3.3 and 3.4) to calculate the mass distribution of a dark matter halo's progenitors.

3.1 Statistical properties of the density fluctuations

Reconstructing the actual realisation of the overdensity $\delta(\mathbf{x})$ at a given time in each point of the Universe is not feasible and the overdensity field is generally statistically treated. A statistical approach is not wrongly stated: on the one hand, only one Universe is known, but on the other hand if the Universe is divided in regions of volume V sufficiently large, the cosmological principle assures that they are perfectly equivalent and constitute a statistical ensemble. Hence, the probability distribution function (PDF) to find at a given position $\mathbf{x}_i$ and at a given time a value of the overdensity field between δ_i and $\delta_i + d\delta_i$ can be calculated. Once its statistical moments are known, the statistics of the density field is completely determined. We approximate the PDF with a multivariate Gaussian [1], a distribution that is totally specified by its second momentum, the two-points correlation function $\xi(r) =< \delta(x)\delta(x+r) >$. In the Fourier space, single modes evolve independently, the k-space PDF is still a Gaussian and its second momentum (the power spectrum) is:

$$P(k) = \sigma_k^2 =< \delta_{\mathbf{k}}\delta_{\mathbf{k}}^* >, \tag{3.1}$$

[1] This approximation is supported by inflationary models and it is in good agreement with experimental data from the CMB.

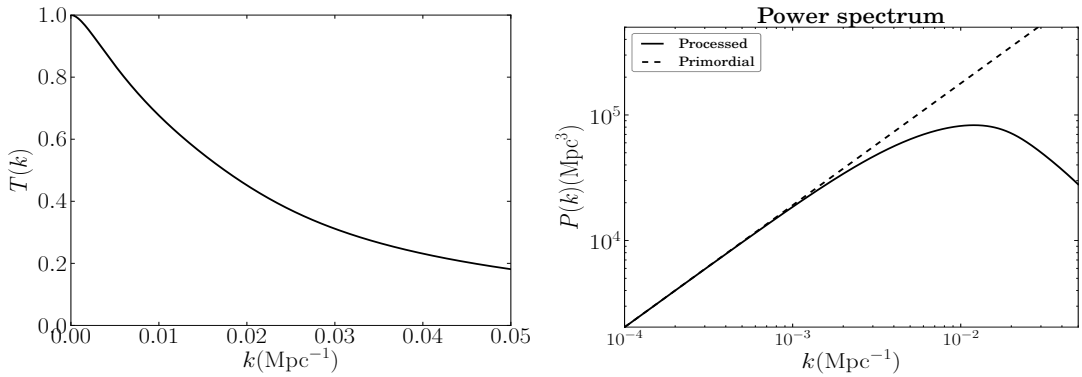

(a) Transfer function **(b)** Power spectrum

Figure 3.1: Fig. (a) shows the transfer function from Eisenstein and Hu, 1998. Fig. (b) shows the primordial power spectrum (dotted line) and the processed one (solid line). The transfer function suppresses the scales above $k \approx 0.01$.

being the Fourier transform of $\xi(r)$. The shape of $P(k)$ has been proposed by the Harrison and Zel'dovich ansatz:

$$P_i(k) \propto k^n, \tag{3.2}$$

in good agreement with experimental data if $n = 0.965 \pm 0.004$ (Planck Collaboration et al., 2018). The power spectrum is normalized from results of galaxy surveys, as we discuss in the next Sec. 3.2. In Sec. 2.2.1 we stressed that in the radiation dominated era, fluctuations grow as long as they enter the Hubble horizon, implying that different modes have different evolution; in particular, the power spectrum seeded structure formation is not the primordial one and the *processed* power spectrum is

$$P(k) \propto k^n T^2(k); \tag{3.3}$$

the *transfer function* $T^2(k)$ suppresses the small scale fluctuations with λ smaller than the Hubble radius, at the transition between the radiation dominated and the matter dominated era (that is $\approx$ 100Mpc). The transfer function by Eisenstein and Hu, 1998 and the power spectrum are shown in Fig. 3.1.

3.2 The halo mass function

Theory of structure formation allows to predict the number density of dark matter halos as a function of mass and z. Press and Schechter, 1974 (hereafter, PS) developed an analytic model for distribution function of collapsed halos,

based on the ansatz that once a region reaches the threshold amplitude for collapse (Eq. (2.46)) calculated according to the linear theory, it virializes. The theory considered a smoothed density field on a scale R:

$$\delta_R(\mathbf{x}) = \int \delta(\mathbf{x}+\mathbf{x}')W(R,\mathbf{x})d^3\mathbf{x}', \tag{3.4}$$

where W is the *window function*,

$$W(R,\mathbf{x}) = 4\pi R^3 \frac{\sin kR - kR\cos kR}{(kR)^3}, \tag{3.5}$$

a top-hat in the $\mathbf{k}-$space that sharply cuts out details on scales smaller than R. The equivalent volume of this window is $V_W = \int d^3\mathbf{x}W(\mathbf{x}) = \frac{4\pi}{3}$ and the excess of mass around a point $\mathbf{x}$ is

$$\delta M(x) = \int d^3\mathbf{y}\delta\rho(\mathbf{y})W(\mathbf{x}-\mathbf{y}) = \int \frac{d^3\mathbf{k}}{(2\pi)^3}\tilde{\delta}_{\mathbf{k}}\bar{\rho}\tilde{W}(\mathbf{k})e^{i\mathbf{k}\cdot\mathbf{x}}. \tag{3.6}$$

Applying the central limit theorem it is easily seen that $\delta M/M$ has a Gaussian distribution and a standard deviation,

$$\sigma_M^2(R) = \langle|\delta M/M|^2\rangle = \frac{1}{2\pi^2 V_W^2}\int_0^\infty k^2 dk\sigma_k^2\tilde{W}_k^2, \tag{3.7}$$

in terms of the power spectrum: the power spectrum normalization is experimentally fixed from the observational value of σ_M on the scale of $R = 8h^{-1}$Mpc, briefly indicated with $\sigma_8 = 0.811$ (Planck Collaboration et al., 2018). The theory of Press and Schechter, 1974 predicts that the fraction of mass elements in collapsed objects with mass greater than M at redshift z is equal to the probability that the present day linear extrapolated density, δ_M, is greater than $\delta_c = 1.686$ (see Sec. 2.2.2):

$$F(>M,z) = \frac{1}{2}\mathrm{erfc}(\nu_c) \tag{3.8}$$

where $\nu_c = \delta_c/\sigma(M,z)$. This distribution is not correctly normalized to one and $F(>0,z) = 1/2$. This is due to the *cloud-into-cloud problem*, since Eq. (3.8) ignores regions that are not part of a collapsed object greater than M_1 but are part of a collapsed object greater than $M_2 > M_1$; i.e. ignores overdensities with $\delta_{M_1} < \delta_c$, smoothed on a scale M_1, and with $\delta_{M_2} > \delta_c$, smoothed on a scale $M_2 > M_1$. In the original Press and Schechter, 1974, theory the problem is

solved by multiplying $F(>M,z)$ for a factor 2. The PS mass function, then, is

$$\frac{dn(M,z)}{dM} = -\frac{\overline{\rho}}{M}\frac{\partial F(M,z)}{\partial M} = \frac{\bar{\rho}}{M^2} f_{PS} \left| \frac{d\ln\nu}{d\ln M} \right| \tag{3.9}$$

with

$$f_{PS}(\nu_c) = \sqrt{\frac{2}{\pi}}\nu_c \exp\left(-\frac{\nu_c^2}{2}\right). \tag{3.10}$$

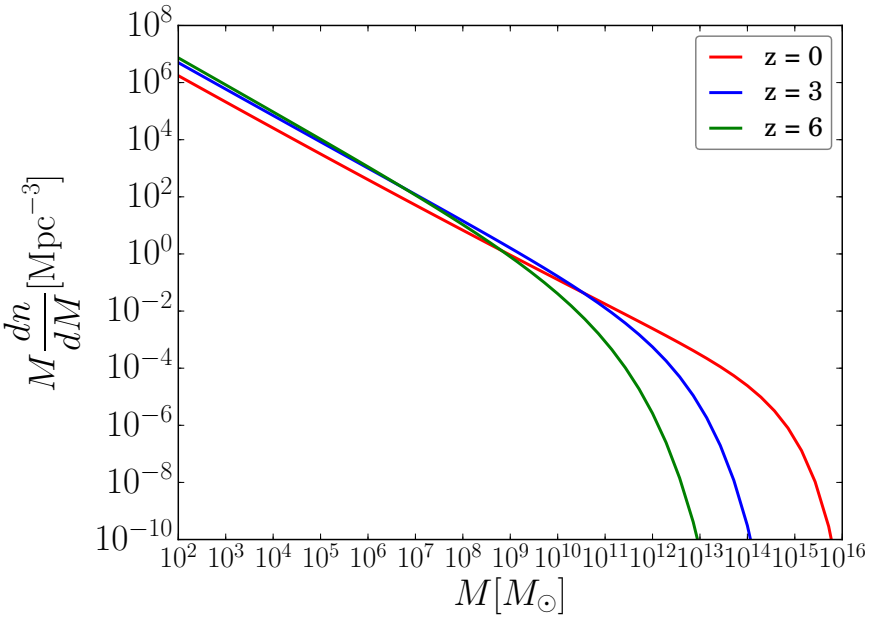

Figure 3.2: Press-Schechter mass function at redshift $z = 0, 3, 6$. Population of halos at higher redshift is skewed in favour of lower mass halos, with respect the one at $z = 0$ suggesting that the structures formation occurred hierarchically.

Fig. 3.2 shows the PS mass function in units of Mpc^{-3} for different redshift values, $z = 0, 3, 6$. It clearly emerges that the population of halos at higher redshift is skewed in favour of lower mass halos, with respect the one at $z = 0$. This represents a hint that the structures formation occurs *bottom − up* (i.e. hierarchically). As is shown in Fig. 3.3a, σ_M is a decreasing function of mass, because $\sigma_M^2 \sim k^{3+n} \sim R^{-(n+3)} \sim M^{-\frac{n+3}{3}}$.

In Sec. 2.2.1 it is stressed that in matter dominated epoch the fluctuations grow with a scale factor $\delta \propto D(z) = 1/(1+z)$, but when the cosmological constant cannot be neglected, the growth is inhibited and the analytical form of the growth factor $D(z)$ is far more complex. In particular, according to the fitting function by Carroll et al., 1992,

$$D(z) = \frac{g(z)}{g(0)(1+z)}, \tag{3.11}$$

and

$$g(z) = \frac{5}{2}\omega_m(z)\left[\omega_m(z)^{4/7} - \Omega_{DE}(z) + \frac{1+\omega_m(z)/2}{1+\Omega_{DE}(z)/70}\right]^{-1}. \quad (3.12)$$

$g(z)$ is plotted in Fig. 3.3b and compared with the growth factor in the Einstein-de Sitter regime.

The formulation above implies that,

$$\sigma_M(M,z) = D(z)\left(\frac{M}{M^*}\right)^{-(n+3)/3} = \left(\frac{M}{M_{NL}(z)}\right)^{-(n+3)/3}, \quad (3.13)$$

where M_{NL}, the mass scale at which fluctuations become non linear,

$$M_{NL}(z) = \frac{M^*}{D(z)^{(n+3)/3}}, \quad (3.14)$$

is a decreasing function of redshift (the work by Eisenstein and Hu, 1998 states that $n > -2$): so that smaller scales enter this regime before larger ones. As a consequence, the structures formation is *bottom-up*: smaller halos form first and merge together to form more massive halos. This statement is at the basis of the analysis in Chapters 8 and 9, in which we explore the possibility that massive black holes form by merging of smaller progenitors.

In Fig. 3.2, the heavy-end cut-off occurs at lower mass with respect to $z = 0$ and halos with mass larger that $10^{13}M_\odot$ are indeed very rare at $z > 6$. Consider for example the case of a very well-studied quasar at $z = 6.4$, SDSS J1148+5251, supposed to be powered by a black hole of mass $M_\bullet \approx 10^9 M_\odot$. If we extrapolate up to $z = 6.4$ the correlation observed at lower redshift (Magorrian et al., 1998; Häring and Rix, 2004) between the black hole mass with the bulge of the host galaxy ($M_\bullet \approx 10^{-3} M_{bulge}$), we can estimate that the halo hosting the quasar has a mass of order $10^{13}M_\odot$. Nevertheless, integrating Eq.(3.9) we found that less than 10^{-3} DM halos with mass higher than $10^{13}M_\odot$ per Gpc^3 are expected at $z = 6.4$. High-z luminous quasars are theoretical supposed to be indeed very rare and the problems related their puzzling presence are still open questions. This issue is widely discussed from Chapter 5 on.

3.3 Conditional Mass Function

PS formalism do not analyse correlations between different halos or different mass scales. They are necessary to study how halos in a given time are related to the ones in previous time.

The *excursion set formalism* (ES) (Bond et al., 1991) is a a more corrected, self-consistent formalism to compute the mass function. It provides new insights on the spatial distribution and history of dark matter halos and allows to study of the growth of the halos by accretion and mergers. Furthermore, in the extended theory, the derivation of the factor 2 in the Eq. 3.9 is better justified. Similarly to the PS theory, the ES is based on the existence at a given redshift of a critical value for δ_M for a halo to virialize. The main concept of this approach is to smooth the density field around a certain point on different mass scales. On sufficiently large mass scale $\delta_M \to 0$ and, on smaller scales, δ_M vary from zero, with variance equal to σ_M^2. This concept is more clear in Fourier-space: when smaller scales are considered, more Fourier modes become important, adding fluctuations to the density field; the ensemble of the modes determines the shape of δ_M as a function of the smoothing scale M. Since each of the modes are independent and evolve separately, the δ_M can be analysed with the same statistic of a diffusion process: every mode added at smaller scales is a *step* in the *random walk* of the density field and the abundance of the halos is determined by the distribution of these random walks. A point in the random walk belongs to a halo of mass M if its trajectory first overcomes the virialization threshold at the mass M. This procedure is not completely flawless: for most choices of the window function, δ_M are correlated one to another and the statistics is extremely complex. Fortunately, we can choose the window function as a sharp $k-$space top-hat, which functional form is given by Eq. (3.5) in $x-$space and

$$W_k = \begin{cases} \text{const} & k < k_c \\ 0 & \text{otherwise} \end{cases} \tag{3.15}$$

in the Fourier space. In this case each step corresponds to increasing k_c and the statistics is simpler, since each of the modes evolves independently. With this filter the steps are uncorrelated to each other. At the end, the fraction of mass elements contained in a collapsed object with mass smaller than M is given by the probability that a random walk remains below the threshold for every $k_c < K_c$, where K_c its the cut-off correspondent to M. This is the unity minus the sum of two probabilities:

- the probability that $\delta_M \geq \delta_c$, which since δ_M has a Gaussian distribution with zero mean and variance σ_M^2 is:

$$p = \frac{1}{\sqrt{2\pi\sigma_M^2}} \int_{\delta_c}^{\infty} d\delta \exp\left(-\delta^2/2\sigma_M^2\right); \tag{3.16}$$

- the probability that $\delta_M < \delta_c$, but $\delta_{M'} \geq \delta_c$ for some $M' > M$; this is again equal to p, since each random walk of this second case can be obtained by a random walk of the first case reflected around its first overcoming δ_c;

so that, analogously to Eq.(3.8):

$$F(< M) = 1 - 2p. \tag{3.17}$$

The latter, once differentiated, lead to the PS Eq.(3.9) (the factor of two arises by the physical consideration that some of the mass elements can appear in local underdensities but belong to larger virialized halo).

This method allows to compute also conditional mass distributions, such as the one of the *progenitors* of a certain dark matter halo. Consider a collapsed region of mass M_1 at redshift z_1 so that it has a linearly extrapolated density contrast $\delta_1 = \delta_c(z_1)$; then, the δ_M corresponds to an element in the halo that first crossed δ_1 at k_{c_1} (at scale mass M_1). The probability distribution for the point of the random walks in which the trajectory first overcome some δ_2 ($z_2 > z_1$) at some $M_2 < M_1$ can be calculated by translating the origin of the random walks from $(k_c, \delta_M) = (0, 0)$ to (k_{c_1}, δ_1); the mass distribution of the progenitors of M_1 at $z_2 > z_1$ is the *conditional mass function*

$$n(M_2, z_2|M_1, z_1)dM_2 = \frac{M_1}{M_2^2}\left|\frac{d\ln\nu_{12}}{d\ln M_2}\right| dM_2, \tag{3.18}$$

where

$$\nu_{12} = \frac{\delta_2 - \delta_1}{\sqrt{\sigma^2(M_2) - \sigma^2(M_1)}}. \tag{3.19}$$

3.4 The Merger-Tree method

In the limit $z_2 \to z_1$ (i.e. for a redshift interval $\Delta z \to 0$), Eq. (3.18) yields:

$$\frac{dN}{dM_2}(z_2 \to z_1) = \frac{M_1}{M_2^2}\frac{df_{PS}(\nu_{12})}{dz_2}\left|\frac{d\ln\nu_{12}}{d\ln M_2}\right| \Delta z, \tag{3.20}$$

proportional to the mean number of progenitors of mass M_2, in which a parent halo of mass M_1 is split in the redshift interval $z_1 \longrightarrow z_2 = z_1 + \Delta z$. Lacey and Cole, 1993 developed a computational approach to study hierarchical models of structures formations, the *merger tree method*, based on an algorithm that reconstructs statistically the genealogical tree of halos: given a root DM halo of mass M_1 at $z = z_1$, the algorithm proceeds backward in time and calculates its

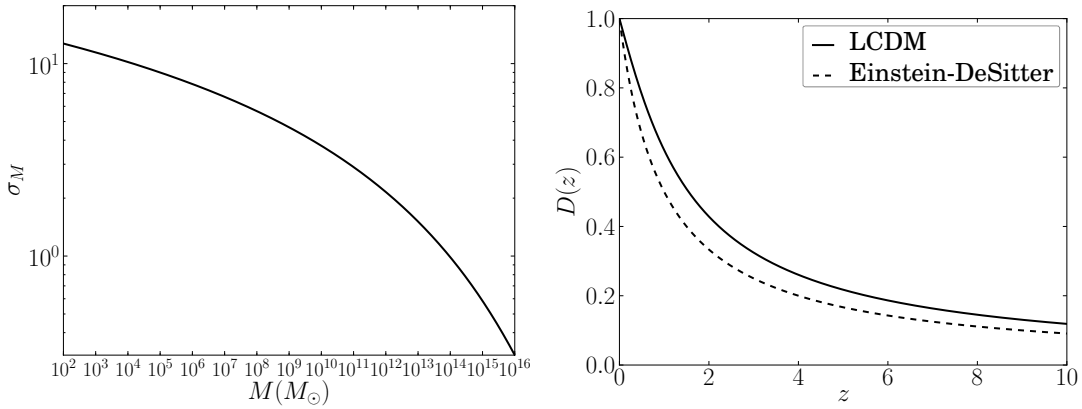

(a) Standard deviation **(b)** Growth factor

Figure 3.3: Fig. (a) shows the standard deviation $\sigma_M(z = 0)$. Fig. (b) shows the growth factor in an Einstein-de Sitter universe (dashed line) and the one from Carroll et al., 1992 (solid line): as can be seen, the presence of a cosmological constant slows the growth of the perturbations.

statistical merger history.

Given the numerical nature of this approach it is necessary to fix a mass resolution M_{res} to keep the computational time affordable (all details of $M < M_{res}$ are ignored). Lacey and Cole, 1993 defined the mean number of progenitors, P, and the mass fraction of the root halo F that is in details smaller than M_{res}:

$$P = \int_{M_{res}}^{M_1/2} \frac{dN}{dM_2} dM_2, \tag{3.21}$$

$$F = \int_{0}^{M_{res}} \frac{dN}{dM_2} \frac{M_2}{M_1} dM_2. \tag{3.22}$$

Setting the initial condition (M_1, z_1) the algorithm goes backward in time of a redshift interval Δz small enough to ensure that the splitting is at most binary (i.e. $P \ll 1$). A random number $0 < R < 1$ is generated and is compared to P:

- if $R > P$, the halo does not split in two progenitors and its mass at redshift $z_1 + \Delta z$ is $M_1(1 - F)$, i.e. the ignored details below M_{res} are assumed to be gravitational captured mass in the time interval corresponding to $-\Delta z$.
- if $R \leq P$, the halo split in two progenitors: one of mass M_2 (randomly generated in the mass interval $M_{res} < M_2 < M_1/2$) and one of mass $M_1(1 - F) - M_2$.

This procedure is iterated for every progenitor halo, at increasing z up to a final redshift z_{end}, generating the merger tree.

In the description of a merger tree algorithm, the following parameters have to be specified: $M_{res}, \Delta z, z_1, z_{end}, M_1$. In Fig. 3.4 is represented an example of merger tree.

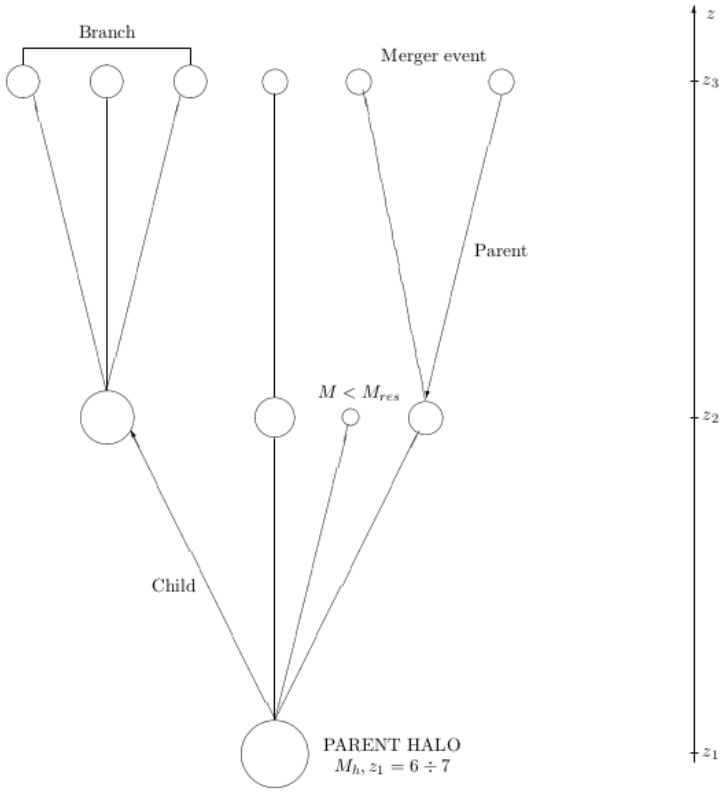

Figure 3.4: Example of merger tree with 3 levels and 11 nodes. The "parent" halo splits in 3 progenitors of $M > M_{res}$ at redshift z_2 (courtesy of A. Petri, master Thesis).

4 Active Galactic Nuclei

In this Chapter we describe the family of active galactic nuclei (AGN) and we discuss their central engine. In Sec. 4.1 we present a brief introduction to active galaxies with their observational features. In Sec. 4.2 and 4.3 we describe black holes and focus on their physical processes that determines galaxies activity.

4.1 Active Galaxies

In the local Universe (i.e. $z \leq 0.1$) about 1 out of 50 galaxies contains a fast accreting supermassive black hole (SMBH) and about 1 out of 3 contains a slowly accreting one (Netzer, 2013) . These galaxies are referred in general as *active galaxies* and their central nuclei are called *active galactic nuclei* (AGN), although many names were attributed to them in the 1960s - 1970s, due their various observational features. In particular:

- **Seyfert galaxies** show relevant surface and nuclear brightness, with the presence of strong ionization lines. Subcategories of these galaxies are usually distinguished since part of them presents strong and broad emission lines (**Type I** Seyfert galaxies) that are not revealed in others (**Type II** Seyfert galaxies).

- **Quasars (QSOs)** are characterized by very strong broad emission lines and (in contrast to Seyfert galaxies) their host galaxies are not clearly revealed. In this Thesis, we follow the common use to refer to high-redshift as "quasars".

- **Blazars** are the only AGN detected in the γ-ray band. Blazars are very rare, since γ-ray emission occurs only when relativistic outflows from the nucleus oriented along the detection line of sight are present.

- **LINERs** (low-ionization nuclear emission-line region) show low-ionized or neutral atom lines and have faint active nuclei.

Seyfert, quasars, blazars and liners include several other subcategories, that we do not describe in detail in this Thesis.

Observational differences in active galaxies are explained by the unified AGN model, that states that different features arise from a difference of perspective: different viewing angle and potential obscurers along the line of sight determine the peculiarity of each type of active galaxies. In particular, AGN can be divided in two wide groups:

- *type-I AGN*, not obscured along the lines of sight that go through their center;
- *type-II AGN*, with heavy dimming along the line of sight, specifically for the optical-UV radiation coming from the inner region.

Fig. 4.1 shows a scheme of the unified model, that describes AGN as:

- the central engine, composed of a SMBH surrounded by an *accretion disk* (see Sec. 4.3.2).
- The *dusty torus*: an opaque structure of dimming material that embeds the accretion disk and is responsible for the obscuration that characterizes type II AGN; its typical size is of the order of 1 pc and covers a wide part of the solid angle.
- The *broad line region* (BLR) within the torus, containing fast rotating line emitting clouds. For the fast Keplerian rotation of the clouds around the SMBH, emission lines are subjected to Doppler broadening.
- The *narrow line region* (NLR) from a few to several thousand parsecs from the SMBH; since these clouds are farther from the center, emission lines experience a weaker Doppler broadening.
- The *relativistic jets*: twin fast outflows, pointing in opposite directions, detectable only if they point along our line of sight. They are found only in one AGN out of 10 and are frequently associated to radio emission.
- The *host galaxy*, often unresolved, contributes to the obscuration, with processes that occurs in its interstellar medium (ISM, Sec. 6.2).

The spectral energy distribution (SED) of AGN is usually expressed as monochromatic luminosity per unit frequency ($L_\nu[\mathrm{erg\,s^{-1}\,Hz^{-1}}]$), wavelength ($L_\lambda[\mathrm{erg\,s^{-1}\,cm^{-1}}]$) or energy ($L_E[\mathrm{erg\,s^{-1}\,erg^{-1}}]$). In contrast to stars, AGN emission occurs in the whole electromagnetic spectrum and in particular in the bands:

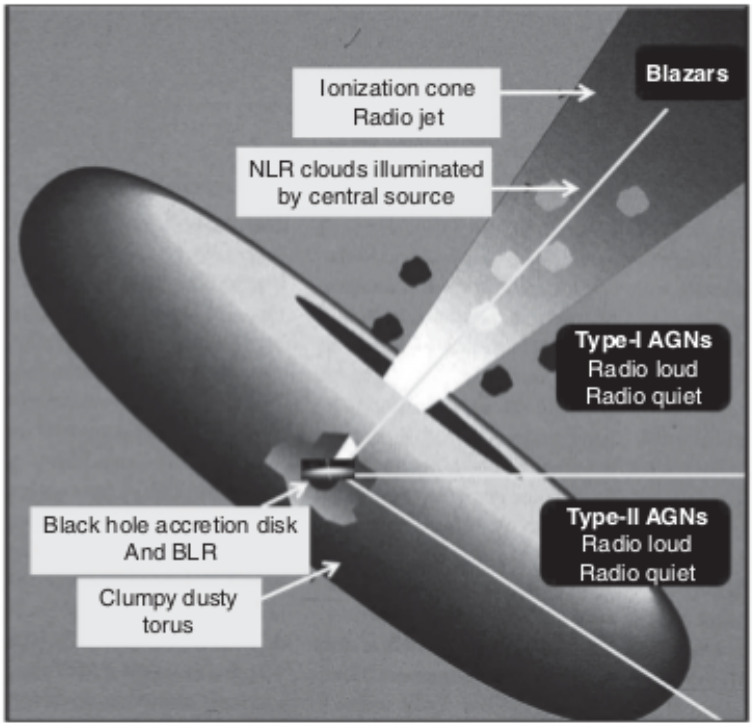

Figure 4.1: A side view of AGNs showing the main concepts of the unification scheme, by Netzer, 2013 .

- *Radio*: several AGN show radio lobes structures (single or double) that can overcome the dimension of the host galaxies and radio cores and/or radio jets from the nucleus. Radio emission divides AGN is two categories: the *radio-loud*, with with monochromatic luminosity at 5 GHz ten times stronger than the monochromatic luminosity in the B optical band, and the*radio-quiet*, without this feature. Statistically, 1 AGN out of 10 is radio-loud and several AGN are identified in deep radio surveys; since stellar sources present weak radio emission, optical pointlike sources that show significant radio emission are good radio-loud AGN candidates.

- *IR*: the majority of the near infra-red (NIR) and the mid-infra-red (MIR) is caused by secondary (i.e. not due to the accretion itself) thermal emission from the dusty torus, which temperature is of the order of 100 K. The far infra-red (FIR) is due to thermal emission of colder dust, heated by young stars in the host. Highly obscured AGN cannot be detected in optical and X-ray bands but are observed for their high IR emission, making IR observations a complementary approach to reveal AGN.

- *Optical and UV*: optical emission of type-I AGN can overcome the whole

stellar emission of the host galaxy, even if local AGN are usually much fainter than the host. Stellar emission can be easily discriminated in optical observation, since AGN optical emission differs from the stellar for the shape of the SED and for the lack of typical stellar absorption lines.

- *X-rays*: For decreasing wavelengths the contamination by stellar sources is less relevant since, unlike stars, almost every AGN is a powerful X-ray emitter. X-ray emission is widely treated in this Thesis: in Chapter 6 we construct a X-ray emission model applied to quasars observed at high-z (Sec. 6.3) and used to make forecasts of quasars' progenitors (Chapter 8). In fact, over the energy range 0.2-20 keV AGN emitted spectrum is well-fitted by a single power-law $L_\nu \propto \nu^{-\alpha_X}$, where the parameter $\alpha_X \sim 1$ is experimentally constrained (Piconcelli et al., 2005). Very distant sources (above $z \sim 7$) with strong 0.5-2 keV emission are well in reach of current surveys, in contrast to faint type-II AGN with column densities $N_{HI} > 10^{22}\mathrm{cm}^{-2}$ of obscuring material. To date, the most sensitive surveys have been done with the Chandra Space Telescope, whose resolution is ~ 1 arcsec and a passband that reach 20 keV.

- $\gamma-$*rays*: only 1 out of 10 AGN show strong emission above 100 keV. Current $\gamma-$ray observatories (e.g. Fermi Gamma-Ray Space Telescope) probe high-energy emission up to 300 GeV, but do not have a good angular resolution and the detected AGN appear as point-like sources.

In the following Section we describe AGN energy source: accreting black holes.

4.2 Black Holes

Current paradigm of AGN states that they are powered by an accreting supermassive black hole (SMBH). In this Section we present a black holes (BH) in the context of general relativity. Historically, BH (as well as pulsars and neutron stars) had been deemed as a pure theoretical oddity for a long time. The concept of an object so massive that light itself cannot escape to its gravity is ascribed to John Michell and Pierre-Simone Laplace in the XVIII century; the first inherent document is a letter from John Michell to Henry Cavendish in 1783 to the Royal Society:

If the semi-diameter of a sphere of the same density as the Sun were to exceed that of the Sun in the proportion of 500 to 1, a body falling from an infinite height

towards it would have acquired at its surface greater velocity than that of light, and consequently supposing light to be attracted by the same force in proportion to its vis inertiae, with other bodies, all light emitted from such a body would be made to return towards it by its own proper gravity.

The concept of "dark stars", promoted in 1796 by Laplace in his text *Exposition du systéme du Monde*, had nothing to do with space and time, considered as absolute concepts: dark stars were conceived in the framework of the Newtonian theory of matter and gravitation, with a rigid object beyond the horizon, stable against the collapse. Only in the XIX century, BH were studied in general relativity as solution of Einstein's field equations.

4.2.1 Black Holes as solution of Einstein equations

The formulation of general relativity by Albert Einstein (1907-1915) completely overturned the classical theory of space and time. For the first time, the concepts of space and time were treated as a single entity and represented as a single mathematical structure. In a certain fixed position and time a physical event is described as a four-vector x^μ, i.e. an element of of a 4-D real manifold, such that x^0 represents the time coordinate and x^i, with $i = 1, 2, 3$ are the spatial coordinates. The calculation of space-time distance between two events requires a geometrical structure on the manifold, i.e. a metric tensor $\delta_{\mu\nu}$. For example, the metric tensor in the Euclidean space is a Kronecker delta function and in the Minkowskian space is:

$$\delta_{\mu\nu} = \begin{pmatrix} 1 & 0 & 0 & 0 \\ 0 & -1 & 0 & 0 \\ 0 & 0 & -1 & 0 \\ 0 & 0 & 0 & -1 \end{pmatrix}; \tag{4.1}$$

hence the infinitesimal space-time distance ds between two events is:

$$ds^2 = \delta_{\mu\nu} dx^\mu dx^\nu. \tag{4.2}$$

As introduced in Sec. 2.1.2, general relativity relates gravity to the curvature of the space-time and the space-time geometry (so the metric) to gravitational sources (see Eqs. (2.12)). A complete discussion on the Einstein equations solution lies outside the goals of this work; here we focus on the particular solutions that describes black holes. In particular, the Schwarzschild metric (formulated in 1916 by Karl Schwarzschild) represents the space-time geometry in a vacuum

region that embeds a static, spherical object whose whole mass M is concentrated at its center $r = 0$. The Schwarzschild metric in spherical coordinates (t, r, θ, ϕ) is:

$$ds^2 = (1 - \frac{2GM}{rc^2})c^2dt^2 - (1 - \frac{2GM}{rc^2})^{-1}dr^2 - r^2(d\theta^2 + \sin^2\theta d\phi^2), \qquad (4.3)$$

where G and c are the gravitational constant and the speed of light, respectively. Schwarzschild metric has two singular point:

1. $r = 0$, that is a physical and unavoidable singularity;
2. $r_S = \frac{2GM}{c^2}$, that is proper of the Schwarzschild metric and can be eradicated with a change in the coordinates.

The radial distance r_S, the *Schwarzschild radius*, represents the surface of the *horizon of events*: no light can escape from the inside (for a complete description of the horizon, we refer to Schutz, 1985 and Romero and Vila, 2013). Indeed, a Schwarzschild radius can be calculated for every object of mass M, but if density of the structure is ordinary, r_S is far smaller that the geometrical radius: for example, r_S of the Sun is about 3 km and r_S of the Earth is of the order of a centimeter.

Other solutions of the Einstein equations have been calculated in order to describe BH phenomenology, for example the Kerr metric (1963) that represents a rotating BH (Romero and Vila, 2013; Schutz, 1985).

4.3 BH accretion

The *no-hair theorem* states that a black hole is totally described by three physical quantities: mass, spin and electric charge. However, electric charge can be neglected, since astronomic objects are nearly neutral, and the angular momentum is null for a Schwarzschild black hole (nevertheless, rotating BH are predicted by the Kerr metric, mentioned in the previous Sec.).

In spite of the simplicity of this description, a BH has a remarkable impact of the region it is settled in. In particular, black hole gas accretion generates, through several processes, a majestic release of energy: as a gas particle falls toward the BH, its potential energy is converted to kinetic energy and dissipated in thermal energy with a huge radiation emission. The emission occurs with high efficiency η, in the range $\eta = 0.057$ to 0.32, the minimum occurring for a static BH and the maximum for a maximally rotating BH (Thorne, 1974). In comparison,

energy release by nuclear fusion reaction occurs with matter-radiation conversion factor lower than 0.01.

Nevertheless, the accretion process is self-regulating: the emitted luminosity affects the gas layers around the black hole, eventually blocking further gas infall. Consider the spherically symmetric accretion of metal-free, completely ionized gas. If the energy release in this process is constituted by photons with energy < 100keV, the photons interacts with the gas mainly by Thomson scattering. Be L the emitted luminosity, so that the momentum carried by the photons for unit time is L/c and the momentum for unit time and surface (at distance r from the center) is $L/4\pi r^2 c$. Thomson scattering is isotropic and on average an electron gains all the momentum of the incident photon. In principle, not every electron is scattered, the probability given by the the Thomson cross-section σ_T. The force on the gas as a function of distance r is:

$$F_r = \frac{L}{4\pi r^2 c}\sigma_T n_e, \tag{4.4}$$

where n_e is the electron density in the gas. In the gas flow electrons and protons are electrostatically coupled. F_r mostly acts on electrons, because $\sigma_T \propto m^{-2}$ and $m_p \gg m_e$, while gravity acts mostly on protons:

$$F_g = n_e \frac{GMm_p}{r^2}. \tag{4.5}$$

The luminosity in equilibrium state ($F_g = F_r$) is known as the *Eddington luminosity*:

$$L_E \equiv \frac{4\pi c G M m_p}{\sigma_T} \approx 1.5 \times 10^{38} \frac{M}{M_\odot} \mathrm{erg} \cdot \mathrm{s}^{-1}, \tag{4.6}$$

directly proportional to the BH mass M. The Eddington luminosity is the upper limit for stationary sources: if $L \gg L_E$ the accretion flux (fueling luminosity itself) is blocked by the radiation pressure.

The radiative efficiency η of the process is defined as the matter-radiation conversion factor:

$$L \equiv \eta \dot{M} c^2, \tag{4.7}$$

where $\dot{M}$ is the matter flux falling on the BH. A commonly used value for radiative efficiency is$\eta = 0.1$ (Vietri, 2006, Petri et al., 2012a, Volonteri and Stark, 2011 and Frank et al., 2002). The *Eddington accretion rate* is the upper limit of a BH accretion rate and is defined as the matter flux that produces an Eddington

luminosity:

$$\dot{M}_E \equiv \frac{L_E}{\eta c^2} = 2.5 \times 10^{-8} \frac{M}{M_\odot} \frac{0.1}{\eta} M_\odot \mathrm{yr}^{-1}. \tag{4.8}$$

Assuming that the fraction of mass that is not converted in radiation is actually accreted by the compact object (that in our case of interest is a BH), the growth rate of the black hole is: Consider the gas flux $\dot{M}$ towards the BH, a fraction of the matter for unit time $\eta\dot{M}$ is converted in radiation and the remaining $\dot{M}_\bullet = \dot{M}(1-\eta)$ is actually captured by the BH. The BH bolometric luminosity Eq. (4.7) is then:

$$L = \dot{M}_\bullet \frac{\eta c^2}{1-\eta}. \tag{4.9}$$

Assuming a BH to grow at its Eddington rate, the time scale for its growth is defined as: $\tau_E = M_\bullet/\dot{M}_\bullet = t_E \eta/(1-\eta)$, where the quantity t_E is known as *Eddington time*.

In the majority of the astrophysical processes, the gas has got enough angular momentum to not allow a radial fall on the BH. In particular, in general relativity an innermost stable orbit is predicted: this corresponds to the minimum angular momentum $j_{min} = qGM/c$ (Vietri, 2006), being q an adimentional parameter of order of unity[1]. Thus, all the accreting elements that possess an angular moment $j > j_{min}$ arrange themselves in a disk perpendicular to the rotational axis. Indeed, consider a BH of mass $\approx 10^8 M_\odot$ in the center of a galaxy; the gas infall is supplied from the whole galaxy and it rotates at distance and velocity of the order of 10^3 pc and 100 km/s. The angular momentum j is of the order of $3 \times 10^{28} \mathrm{cm}^2\mathrm{s}^{-1}$ and $j_{min} \approx 4 \times 10^{23} \mathrm{cm}^2\mathrm{s}^{-1} \ll j$.

The formation of an accretion disk is theoretically predicted but still controversial (see Chisholm et al., 2003 and Davies and Pringle, 1980 for arguments in favor of disk-like or spherical accretion geometry, respectively). In Chapter 7 we use the results by Beskin and Karpov, 2005 stating that, for nearly any BH velocity, neither ISM turbulent motions nor density fluctuations can prevent the realization of the spherical accretion regime around a stellar-mass BH wandering in the host galaxy. Spherical and disk-like accretion are, indeed, subject of the next Sections.

4.3.1 Bondi accretion

Consider the case in which the accretion on the BH has got spherical symmetry and assume that the gas is represented by a polytropic relation $PV^\gamma = constant$

[1] $q = 2\sqrt{3}$ in a Schwarzschild black hole (Vietri, 2006).

(where γ is the gas adiabatic index) and that accretion is stationary (such that $\partial/\partial t = 0$). Then, the mass conservation law yields:

$$\frac{\partial \rho}{\partial t} + \nabla \cdot (\rho \vec{v}) = \frac{1}{r^2}\frac{\partial}{\partial r}(r^2 \rho v_r) = 0, \tag{4.10}$$

where, ρ is the gas density, r is the radial coordinate and v_r is the average radial velocity of the gas. From the integration of the previous equation, the mass that falls on the BH for unit time is:

$$\dot{M} = 4\pi \rho v_r r^2. \tag{4.11}$$

To calculate $\dot{M}$ it is necessary to fix boundary conditions; far from the BH center, the density and the pressure of the gas are ρ_∞ and P_∞, respectively, and the gas it at rest. Bernoulli theorem states that the sum $\frac{v_r^2}{2} + w + \phi$ is conserved along the flux, being $w = \epsilon + P/\rho = \gamma P/((\gamma - 1)\rho)$ is the specific enthalpy, ϵ the internal energy of the gas for unit mass and ϕ the gravitational potential. Then,

$$\frac{v_r^2}{2} + w - \frac{GM}{r} = w_\infty, \tag{4.12}$$

where w_∞ is the specific enthalpy to infinity.

For the sake of clarity is useful to introduce different units, expressing velocity in units of the speed of sound to infinity $c_{s_\infty}^2 = \gamma P_\infty/\rho_\infty$, density in units of ρ_∞ and radial distance in units of the accretion radius $r_a = 2GM/v_s^2$, where the sound speed is equal to the free fall speed. With this choice of coordinates, $\dot{M}$ is totally determined by a parameter λ such that:

$$\dot{M} = 4\pi\lambda \frac{G^2 M^2 \rho_\infty}{c_{s_\infty}^3}. \tag{4.13}$$

Eqs. (4.13) and (4.12) give only one value of λ that obeys to the condition of continuity at the sonic point (i.e. r such that $v_r = c_s$):

$$\lambda = \left(\frac{1}{2}\right)^{\frac{\gamma+1}{2(\gamma-1)}} \left(\frac{5-3\gamma}{4}\right)^{-\frac{5\gamma-3}{2(\gamma-1)}}. \tag{4.14}$$

This λ value is the one that gives the *Bondi accretion rate* (from Eq. (4.13)). The Bondi rate is dependent on the mass M, on the adiabatic index γ and on the initial density and pressure.

The radiative efficiency of Bondi accretion is tiny, being $\eta_{Bondi} \approx 10^{-4}$ (Shapiro, 1973). Indeed, the BH surface is not solid and there are not any shock waves that

can accelerate electrons so that there is not a population of non-thermal electrons in the flow. The only radiative process in the flow is, then, *bremsstrahlung* but, on the one hand if the gas is dense, the time scale in which photons diffuse outward is longer than the free fall time; on the other hand if the gas is rarefied, the cooling time is longer than the free fall time. In practice, on both hands, the majority of the gas potential energy is not dissipated in thermal energy and it is not radiated away.

Nevertheless, there is growing evidence that strong magnetic fields are present in high-z galaxies (Bernet et al., 2008, Robishaw et al., 2008, Murphy, 2009); these fields are thought to be generated through turbulent amplification of weak magnetic seed fields (Sur et al., 2010, Federrath et al., 2011, Banerjee et al., 2012), probable relics of the very early Universe (Turner and Widrow, 1988). In the case of low accretion rates then the dominant radiative process is synchrotron emission: this is indeed the case if $M_\bullet < 10^4 M_\odot$ (Shvartsman, 1971). The evaluation of the synchrotron spectrum is particularly complex and involves the calculation of the particle energy distribution in the inflowing plasma. The particle energy distribution is determined by the superposition of three contributions: adiabatic heating, synchrotron cooling and non-thermal heating, the latter being a consequence of the Shvartsman, 1971 equipartition theorem of thermal, gravitational and magnetic energy density. For this equipartition to be valid, there must be a dissipation mechanism of the magnetic field; therefore, the field is no longer frozen-in: the conductivity decreases, relative motions between the magnetic field and the plasma develop and currents begin to flow and heat the gas. This process dissipates about 25% of the rest energy of the infalling material (Beskin and Karpov, 2005) as a result of the formation of turbulent current sheets, that cause fast magnetic field lines reconnection and energy release[2]. About the 10% of the energy released in reconnection goes in excitation of plasma oscillations, whereas the remaining 90% accelerates the particles up to a maximum Lorentz factor $\gamma_{max} \simeq 10^5$. In conclusion, the total particle energy distribution[3] can be expressed as the sum of a thermal and a non-thermal component:

$$f(R,\gamma) = f_t(R,\gamma) + \zeta f_{nt}(R,\gamma) \propto \frac{d^2N}{dRd\gamma}, \tag{4.15}$$

where $R = r/r_g$, and ζ expresses the ratio between the non-thermal and thermal

[2] A similar process is responsible for the origin of solar flares.
[3] The distribution is not normalized and only the shape has physical meaning.

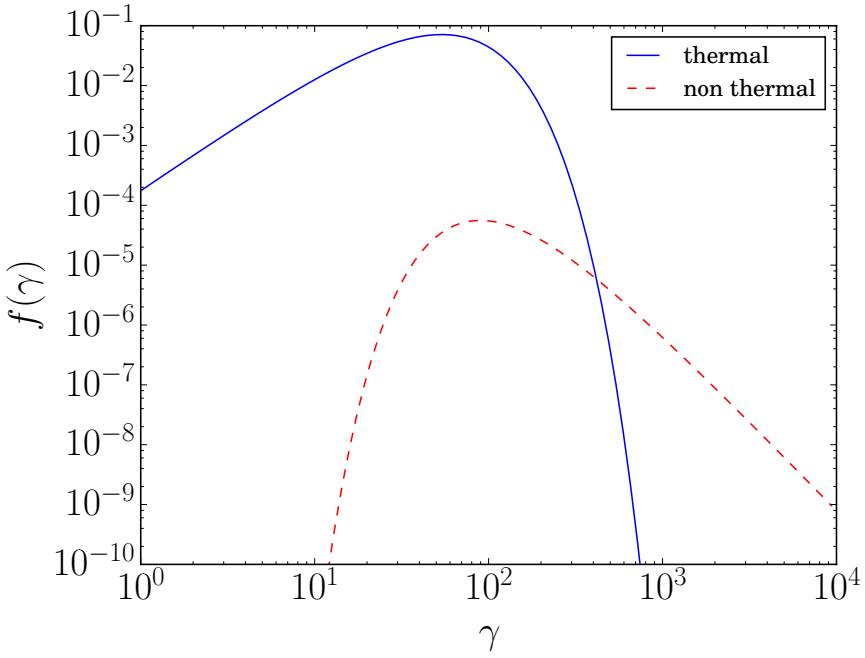

Figure 4.2: Thermal and non-thermal component of the particle energy distribution of the infallig gas, calculated at $R = 50$.

electrons densities:

$$\frac{n_{nt}(R)}{n_t(R)} = \zeta \frac{f_{nt}(R)}{f_t(R)} \tag{4.16}$$

and $f(R) = \int f(R,\gamma)d\gamma$. f_t and f_{nt} for $R = 50$ are shown in Fig. 4.2; for their derivation and analytical expression, we refer to Beskin and Karpov, 2005.

Consider a particle free-falling in the black hole. Knowing the (isotropic) emissivity of the particle in its own rest frame, $j_{\nu'}$ and accounting for relativistic time contraction, gravitational redshift, Doppler effect and the fraction of the emission disappearing in the event horizon, we can compute the single-electron emission spectrum seen from an observer at infinity (Shapiro, 1973). This is:

$$L_\nu^{e^-} = 2\pi \int_{-1}^{\cos\theta^*} j_{\nu'} \frac{1-\beta^2}{(1-\beta\cos\theta)^2} d\cos\theta \ \ \text{erg s}^{-1}\,\text{Hz}^{-1}, \tag{4.17}$$

where

$$|\cos\theta^*| = \sqrt{1 - \frac{27}{4R^2}\left(1 - \frac{1}{R}\right)} \tag{4.18}$$

is the event horizon angular size for a free-falling emitter (Zel'dovich and Novikov, 1971),

$$\beta = \frac{dr}{dt}\frac{1}{1-r_g/r} = \frac{v/c}{(v^2/c^2 + 1 - r_g/r)^{1/2}} \tag{4.19}$$

is the free-falling velocity of the particle in the distant observer rest frame, and

the frequency shift is:

$$\nu' = \nu \frac{1 - (v/c)\cos\theta}{\sqrt{1 - (v^2/c^2)(1 - 1/R)}}. \tag{4.20}$$

Synchrotron emissivity[4] is (Rybicki and Lightman, 1979):

$$j_\nu = \frac{\sqrt{3} e^3 B}{4\pi m_e c^2} F\left(\frac{\nu}{\nu_c}\right) \tag{4.21}$$

$$F(x) = x \int_x^\infty K_{5/3}(\xi) d\xi \tag{4.22}$$

$$\nu_c = \frac{3\gamma^2 eB}{4\pi m_e c}, \tag{4.23}$$

where $K_{5/3}$ is the modified Bessel function, and

$$B = 8 \times 10^4 \left(\frac{10^5 \dot{M}_g}{\dot{M}_E}\right)^{1/2} \left(\frac{M_\bullet}{10 M_\odot}\right)^{-1/2} R^{-5/4} \mathrm{G} \tag{4.24}$$

for the Shvartsman equipartition theorem.

$\dot{M}_E = L_E/c^2 = 1.4 \times 10^{19} (M_\bullet/100 M_\odot)\,\mathrm{g\,s^{-1}}$ is the Eddington rate and $\dot{M}_g = \dot{M}_\bullet/(1-\eta)$ is the gas mass flowing onto the BH per unit time: only a fraction $1-\eta$ of this matter is accreted by the BH, whereas a fraction η is converted in energy and radiated away through synchrotron process. Clearly, if $\eta \ll 1$, then $M_g \approx M_\bullet$. With the electron energy distribution Eq. (4.15), the accretion flow emission spectrum is then:

$$L_\nu = A \int_1^\infty dR \int_1^\infty d\gamma\; f(R,\gamma)\; L_\nu^{e^-}, \tag{4.25}$$

$$A = 4\pi r_g^3 \left(4.33 \times 10^{18}\right) \left(\frac{\dot{M}_g}{\dot{M}_E}\right) \left(\frac{M_\bullet}{M_\odot}\right)^{-1}. \tag{4.26}$$

4.3.2 Accretion disks

In this Sec., we want to investigate the structure and the emissivity of a Keplerian, thin disk: since spherical accretion is not radiatively efficient (Sec. 4.3.1), processes involved in disk-like accretion provide the majority of AGN emission.

[4] We implicitly assumed the particle velocity to be orthogonal to the magnetic field: in fact adiabatic compression increases only the perpendicular component of the particle momentum.

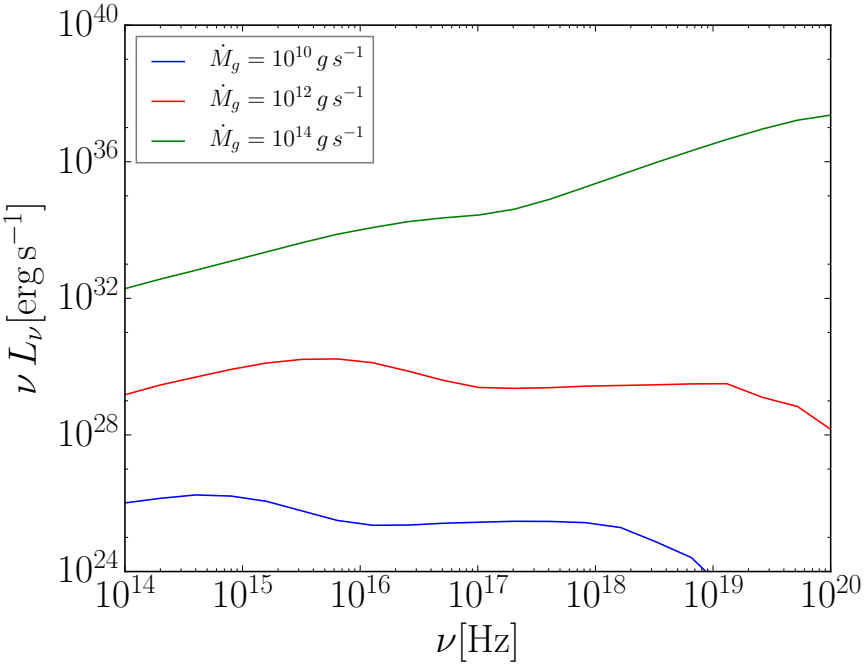

Figure 4.3: Synchrotron spectrum of the acretion flow for different values of the accretion rate.

In a perfectly Keplerian system the only gravity acts on the gas. Gravitational force is *central*, i.e. angular momentum is conserved, implying that for the accretion to occur, physical processes that produce a rearrangement of the angular momentum of the gas has to take place. A classical analogue is constituted by two solid rings in centrifugal equilibrium, which have angular velocity $\omega_K = GM/r^3$: the rings rotate at different velocity, sliding one against the other. Friction force acts between the two rings: the total angular momentum of the system is conserved, but the angular momentum lost by the inner ring is gained by the outer one. The same concepts apply to a disk-like system: infall occurs only if angular momentum is carried outward. In particular, two conditions have to occur in the disk:

- the gas must loose angular momentum and the total torque $G(r)$ that the gas outside the radius r applies on the gas inside r must be:

$$G(r) < 0. \tag{4.27}$$

- Consider a gas ring of infinitesimal thickness dr centered in r: this ring exercises a torque on the immediately inner ring and is subjected to a torque from the immediately outer ring. The total torque on the ring in r

is $\partial G(r)/\partial r$ and, if angular momentum is lost:

$$\frac{\partial G(r)}{\partial r} < 0. \tag{4.28}$$

If both conditions on the torque are satisfied, angular momentum is carried outward through the disk.

Consider an infinitely thin disk and its surface density Σ. The disk has got axial symmetry and in cylindrical coordinates the continuity equation is:

$$\frac{\partial \Sigma}{\partial t} + \frac{1}{r}\frac{\partial}{\partial r}(r v_r \Sigma) = 0. \tag{4.29}$$

If a gas element is subjected to a torque G, the conservation of the angular momentum L along the rotational axis $\vec{z}$ yields:

$$\frac{\partial L_z}{\partial t} + \frac{1}{r}\frac{\partial}{\partial r}(r v_r L_z) = \frac{1}{2\pi r}\frac{\partial G}{\partial r} \tag{4.30}$$

In the stationary case, the integration of Eqs. 4.29 and 4.30 yields:

$$\dot{M} = -2\pi r v_r \Sigma \tag{4.31}$$

and

$$F_L = -r^2 \omega \dot{M} - G(r). \tag{4.32}$$

Here $\dot{M}$ is BH accretion rate and F_L is the flux of angular momentum. F_L is the sum of a negative quantity due to the advection term (in fact the gas that falls on the BH maintains some of its angular momentum) and a positive quantity due to the torques between the disk elements (see Eq. 4.27).

In the case that the gas maintains its whole angular momentum, then $F_L = \dot{M}(GMr)^{1/2}$; while

$$F_L = \beta \dot{M}(GMr)^{1/2} \tag{4.33}$$

if only a fraction β of the angular momentum is kept. In this case, Eq. (4.32), yields:

$$r^2 \omega \dot{M} R(r) = -G(r), \tag{4.34}$$

where $R(r) \equiv 1 - \beta \frac{r_m^2 \omega_m}{r^2 \omega}$ and r_m is the last stable orbit, ω_m is the Keplerian velocity at r_m.

Consider again the classical case of two solid rings, exercising a mutual torque N; the equation of motion of the rings is $\frac{dJ_1}{dt} = -N$, $\frac{dJ_2}{dt} = N$, where J_i $(i = 1, 2)$ are the moment of inertia of the rings 1 and 2, respectively. If moment of inertia

are constant, the kinetic energy loss is:

$$\frac{d}{dt}\left(\frac{\omega_1 J_1 + \omega_2 J_2}{2}\right) = -N(\omega_1 - \omega_2) \approx dr\frac{dN}{dr}N < 0. \tag{4.35}$$

The internal torque then heats the gas in the disk. Eq. (4.35) allows to calculate the heating for unit time and surface:

$$Q = \frac{G}{2\pi r}\frac{d\omega}{dr}, \tag{4.36}$$

which, from Eq. (4.34), yields:

$$Q = \frac{3GM\dot{M}}{4\pi r^3}R(r). \tag{4.37}$$

None of these relations strictly depend on the nature of the torque.

The internal torque G is due to a magneto-hydrodynamic effect. The stress tensor of a magneto-hydrodynamic system has a term known as the Maxwell stress tensor, due to the magnetic field. In particular, the M_{ij} component of the Maxwell stress tensor describes the flux of the $i-$component of the momentum along the $\hat{j}$ direction:

$$M_{ij} = -\frac{1}{4\pi}\left(E_i E_j + B_i B_j - \frac{\delta_{ij}}{2}(E^2 + B^2)\right), \tag{4.38}$$

where E_i and B_i $(i = r, \phi, z)$ are the $i-$component of the electric and magnetic field respectively and δ_{ij} is the delta of Kronecker. Here, the terms relative to E can safely be neglected, since in astrophysical system the electrical conductivity is infinite: $\vec{E} = -\frac{\vec{v}}{c}\wedge\vec{B}$ and both the $E-$terms are quadratic in v/c. The quantity $rM_{r\phi}$ is the flux of L_z through a surface perpendicular to $\hat{\phi}$: indeed it represents the angular momentum lost by the gas within the radius r and gained by the gas outside r.

The torque G is, then:

$$G = \int d\phi r \int dz r M_{r\phi} = \frac{r^2}{2}\int dz B_r B_\phi. \tag{4.39}$$

It is worth to notice that, if hydromagnetic turbulence occurs, B_r and B_ϕ are uncorrelated and their average product vanishes. In this case, no angular momentum is lost. For the angular momentum to flow outside is needed that the product $B_r B_\phi$ is negative along all the lines given by $r = constant$, due to a magnetohydrodynamical instability known as BHVC or MRI.

For the sake of clarity, consider a $S-$shape magnetic field line along z, completely inside the disk at distance r_0 from the BH. The electric resistance is zero and the magnetic field is frozen out: then the central point of the S, in r_0, rotates at constant speed; on the contrary the curves of the S settle in points that rotate faster or slower than r_0. As a consequence, the line is stretched in both radial and tangential direction and the shape of the S gets more and more prominent, in spite of the magnetic field that acts in order to rectify the S. Dividing the $S-$shape in four pieces (concave or convex), it can be demonstrated that in each piece the sign of the product $B_r B_\phi$ is the same and an outward flux of angular momentum occurs.

To conclude this Chapter we comment on the radiative emission of the disk. The luminosity of the disk can be estimated as a function of the parameter β, in the hypothesis that all the energy converted in heat is radiated away. By integration on from r_m to ∞:

$$L = \left(\frac{3}{2} - \beta\right) \frac{GM\dot{M}}{r_m}. \tag{4.40}$$

The radiation efficiency [5] is:

$$\eta \equiv \frac{L}{\dot{M}c^2} = \frac{GM}{2r_m c^2} = \frac{r_S}{2r_m}. \tag{4.41}$$

For a Schwarzschild BH $r_m \approx 3r_S$ (Vietri, 2006) and the efficiency is 1/6. Then, if in spherical accretion the majority of the potential energy is not converted in radiative emission, in disk-like accretion at least (in the case $\beta = 1$) the 50% of the potential energy converted in radiation and the remaining 50% goes in rotational kinetic energy, as stated by the virial theorem.

The temperature T and the spectrum of the disk can be calculated in the assumption of local thermal equilibrium:

$$Q = 2\sigma_{SB} T^4, \tag{4.42}$$

where, σ_{SB} is the Stefan-Boltzmann constant. Then, from Eq. 4.37:

$$T = \left(\frac{3GM\dot{M}R(r)}{8\pi\sigma_{SB} r^3}\right)^{1/4}. \tag{4.43}$$

[5] No relativistic effects are included in this calculation. A complete analysis accounting for relativistic effects is dependent on the BH spin (see Vietri, 2006).

Expressing the radial coordinate in units of the Schwarzschild radius, $x \equiv r/r_S$, from Eqs. (4.6) and (4.7):

$$T = 8 \times 10^7 K \left(\frac{0.1}{\eta}\right)^{1/4} \left(\frac{L}{L_E}\right)^{1/4} \left(\frac{10^{38}\mathrm{erg\,s^{-1}}}{L_E}\right)^{1/4} \left(\frac{R(x)}{x^3}\right)^{1/4}. \tag{4.44}$$

Previous equation along with Eq. (4.6), show that the higher the BH mass, the colder the accretion disk. Local thermal equilibrium implies that the spectrum is locally the one of a black body; the total spectrum is then the sum of several black body spectrum:

$$L_\epsilon = 4\pi r_S^2 \int x dx \frac{2\epsilon^3}{h^3 c^2} \frac{1}{e^{\epsilon/kT(x)} - 1}, \tag{4.45}$$

where h is the Planck constant and ϵ is the energy of the emitted photons.

Eq. (4.44) states that in disks around stellar mass BH most of the emission occurs in the X-rays. On the contrary, accretion disks of SMBH are predicted to emit mostly in the UV, although a characteristic strong X-ray emission in observed in AGN. The nature of this emission is still controversial. The most accredited theory predict that UV photons radiated from the disk are upscattered to X-ray frequency by inverse Compton effect, occurring in a rarefied hot corona. The presence of the corona can be explained by an high density gradient in the disk, heated both by the strong magnetic field and the radiation from the disk. In Fig. 4.4 possible geometry of the corona are shown. On the right side, a model such that photons from the corona interact with the disk. This occurrence would change the local energy balance, making the physics of the disk more complex.

Figure 4.4: Two schematic corona structures, showing probable geometry of the corona. The scattering geometry of the disk-produced and corona-produced photons are depicted. Figure from Netzer, 2013.

To conclude, as X-ray photons travel through the host galaxy, they have a non-null probability to interact with the ISM by Compton or photoelectric effect [6]. These interaction attenuate or totally block the radiation, removing photons from our line of sight. In a beam of photons travelling through the ISM along

[6] In particular, photoelectric absorption extracts of an electron from the K-shell of the atoms in the ISM (Morrison and McCammon, 1983; Yaqoob, 1997).

the infinitesimal path dl the number of photons in a beam N decrease as: $dN = -Nn\sigma dl$, where σ is the total cross-section for the attenuation processes and n is the gas number density. Then if N_0 photons are emitted, N photons survive after the travel along our line of sight:

$$N = N_0\, e^{-\int n\,\sigma\, dl} = N_0 e^{-\tau}, \tag{4.46}$$

the quantity τ is known as *optical depth*.

5 Quasar seeds

In this Chapter we introduce the most accredited theories about the formation and the growth of SMBH that power high-z quasars. Indeed, the presence of such massive black holes in the early Universe (i.e. less then one billion year after the Big Bang) is an open problem in cosmology. In Sec. 5.1 we introduce the scientific issue, while in Sec. 5.2, we describe the formation of SMBH seeds; finally in outstanding issues related to their accretion are commented Sec. 5.3 we analyse the main models of seeds accretion.

5.1 The problem

The paradigm that identifies SMBH as central engine of AGN has been described in Chapter 4. Nevertheless, the detection of high-z quasars leaves many open questions about their birth, growth and evolution. As an example, ULAS J1120+0641 (Mortlock et al., 2011), one of the most distant quasars known to date, has $z = 7.085$, suggesting that the quasar was present in the very young Universe, about 800 millions years after the Big Bang. Assuming that the BH gains a mass fraction $(1 - \eta)$ at the Eddington rate (Petri et al., 2012a, see Sec. 4.3), its mass increase is determined by:

$$\frac{d \ln M}{dt} = \frac{1-\eta}{\eta} \frac{1}{t_E} \tag{5.1}$$

where $t_E \approx 0.45$Gyr is the Eddington time (Sec. 4.3). Then at a given redshift z the BH mass is:

$$M(z) = M_0 e^{\frac{1-\eta}{\eta} \frac{t(z)}{t_E}}. \tag{5.2}$$

For $\eta = 0.1$, the quasar necessitate an initial mass $M_0 \geq 500 M_\odot$ [1] to reach $M = 2 \times 10^9 M_\odot$ (Mortlock et al., 2011) at $z \sim 7$. This value for M_0 is much larger than the mass $M_{stars} < 100 M_\odot$ estimated for the first stars (Greif et al., 2011). However, the fact that accretion occurred at the Eddington rate for almost

[1] This is a lower bound, since is calculated in the assumption that the time available for the growth is 0.77 Gyr, the whole age of the Universe at $z = 7$.

1 Gyr is not a straightforward assumption.

In particular, the primary problems about high$-z$ quasars consist in:

1. the nature of their SMBH *seeds* (i.e. the initial BH of mass M_0);
2. the physical processes that increase *seeds* mass up to a billion of solar masses.

The first point is analysed in Sec. 5.2; the second one in Sec. 5.3.

5.2 Seed formation models

The nature of SMBH seeds is still debated. Three main hypothesis on their mass are considered (Volonteri, 2010b):

- *light* seeds of mass $M_0 \approx 10^2 M_\odot$, born in the redshift interval $z \simeq 20 - 50$;
- *intermediate* seeds, $M_0 \approx 10^3 M_\odot$, formed between $z \simeq 10 - 15$;
- *heavy* seeds, $M_0 \approx (10^4 - 10^6) M_\odot$, formed between $z \simeq 5 - 10$.

In principle, light seeds form very early, hence, in principle, can rely on more time to grow and to merge; however, since accretion rate is proportional to BH mass (Eq. 4.8) the accretion is much slower. In contrast heavier seeds can rely on less time to grow, but they start with bigger initial mass and have higher accretion rates.

In the following, we describe three main hypothesis: that the SMBH seeds form from direct gravitational collapse (Sec. 5.2.1), that they are massive star *remnants* (Sec 5.2.2) and that they from in dense stellar clusters (Sec. 5.2.3).

5.2.1 Direct collapse

The direct gas collapse on a single point is theoretically predicted: if particular conditions occurs, heavy BH seeds can be created through general relativity instabilities.

Consider a neutral gas cloud, its temperature is $T < 10^5$ K and the main cooling processes are:

- if metal in the gas are such that $M_{metals}/M_{gas} > 10^{-4}$, the cooling is dominated by dust thermal emission and molecular and atomic line emission.

- If the gas is metal-free and the gas temperature is higher than $T_{H_2} = 10^2 - 10^3$ K, the cooling is due to the relaxation of the H_2 rotational bands. Nevertheless, H_2 molecule is dissociated by $Lyman - Werner$ photons (11.2-13.6 eV); if the background flux in this band is of the order of $10^{-18} - 10^{-16}\,\mathrm{erg\,cm^{-2}\,s^{-1}\,Hz^{-1}}$ (Bromm and Loeb, 2003a), cooling occurs only through atomic hydrogen.

- In a pristine atomic gas cloud, the cooling is dominated by Lyman$-\alpha$ emission of neutral Hydrogen. This process occurs only if the temperature is above $\approx 10^4$ K.

Then, for the monolithic direct collapse to occur, three conditions must simultaneously occur:

1. the gas must be pristine with only trace amount of metals. According to numerical simulations (Omukai et al., 2008) if gas metallicity overcomes $10^{-4} Z_\odot$, cooling leads to fragmentation in low mass systems ($\sim 0.1 M_\odot$).

2. The host halo must be massive enough so that its virial temperature must be $T_{vir} > 10^4$ K (see Eq. 2.50) and the atomic cooling channel is enabled.

3. A strong Lyman-Werner background must be present, to inhibit molecular cooling. Indeed fragmentation leads to star formation, in competition with a massive seed formation.

If these conditions are satisfied the gas directly flows to the center and eventually experience a general relativity instability leading to a DCBH.

Since DCBHs would be ideal to account for the observed rapid growth of the SMBHs (see e.g. Ferrara et al. 2014a; Rees 1984 for a discussion), they are a popular solution to seeds formation: anyway, this scenario is still awaiting for a solid observational confirmation. The detection of powerful Lyα line emission, combined with the initial claim of a prominent HeII line (unconfirmed by the SILVERRUSH project (Shibuya et al., 2017)) and absence of detectable metal lines, in the $z = 6.6$ galaxy CR7 raised hopes that a DCBH was finally identified. The peculiar emission properties of CR7 (Sobral et al., 2015) could in principle arise from sources formed by pristine gas: either a cluster of Population III stars (see next Sec.) or a DCBH. Following Pallottini et al., 2015a, who compared the spectrum expected from a $10^5 M_\odot$ DCBH with the one of CR7, several authors (Agarwal et al., 2016a; Dijkstra et al., 2016; Hartwig et al., 2016; Smidt et al., 2016; Smith et al., 2016; Visbal et al., 2016) investigated the possible identification of CR7 with a DCBH. Although photometric observations by Bowler et al.,

2017 in the optical, near-IR and the mid-IR bands seem to favour a faint-AGN nature of CR7, Pacucci et al., 2017 confirm that those observations are still consistent with a DCBH and suggest that future spectroscopic observations with the James Webb Space Telescope (JWST) are required to solve the puzzle. To date, although Pacucci et al., 2016a proposed two good candidates ($z > 6$ objects in the CANDELS/GOODS-S field with X-ray counterpart revealed by Chandra), no detection of early SMBH progenitors has been confirmed.

5.2.2 Massive star remnants

Another popular scenario interprets SMBH seeds as remnants of old massive stars. Stars are cataloged in three main groups, according to their metal abundance:

- *population I (PopI)* stars are metal-rich; they are the younger star population, being assembled by gas polluted with metals ejected by earlier giant stars populations. The Sun belongs to this group. PopI stars are found in low-z galaxies and they are not good seed candidates.

- *Population II (PopII)* stars settle in high-z galaxies. They have low heavy elements content, since their formation occurs in regions that are not metal-contaminated. Since PopII stars are more massive and they represent plausible seed candidates.

- *Population III (PopIII)* stars contain no metal, since they form in pristine regions. As explained above, beyond a temperature threshold H_2-cooling is enabled and the gas fragments forming stars. Numerical simulations suggest that PopIII stars are indeed very massive ($M_* \approx 100 M_\odot$, Carr et al., 1984) making good candidates for seed forming. We refer to Sobral et al., 2015 for popIII star observation claims.

The lifetime of massive stars is of the order of 10^6 years. In particular, their fate strictly depends on their mass M_*:

- if $25 < M_*/M_\odot < 140$, a pristine star directly ends in a BH. Due to the low mass of the remnant, $< 100 M_\odot$, these stars are not probable to leave a SMBH seed.

- If $140 < M_*/M_\odot < 260$, once He$-$burning is completed, stars produce in their cores electron-positron pairs. The end of nuclear fusion generates a

pair-instability: the decrease of the radiation pressure causes a violent collapse of the star. The collapse is blocked when O and Si−burning generate energy enough to reverse the process. These stars are eventually destroyed in nuclear powered explosions and do not leave remnants.

- If $M_*/M_\odot > 260$, stars do not experience pair-instability and leave black holes with mass $> 100 M_\odot$, that are good seed candidate. This scenario is the main topic of Chapter 7.

The mass intervals considered above provide a general and reasonable scheme describing stars final fates. Nevertheless, both metallicity and rotational speed of the stars affect their final state. On the one hand, these factors reduce the final stellar mass:

- when gas collapses, gravitational potential energy is converted in heat, that can affect the collapse. Several cooling processes are relevant, such as atomic fine structure line emission, molecular rotational or vibrational line emission, or thermal emission from dust grains. Even if a small amount of metals is present ($\approx 10^{-5} Z_\odot$), dust cooling can trigger mass fragmentation leading to low mass stars (Dopcke et al., 2011, 2013; Ferrara et al., 2000; Omukai et al., 2005; Schneider et al., 2003, 2006; Smith et al., 2015).

- High spin of the collapsing cloud affects star formation: it increases fragmentation and decreases the mass accretion on the protostar (Dutta, 2016; Hirano et al., 2014).

On the other hand, they affect stellar evolution by increasing mass loss by stellar winds:

- mass loss is expected to scale as $\propto \sqrt{Z}$ (Baraffe et al., 2001; Heger et al., 2003; Kudritzki and Puls, 2000; Meynet and Maeder, 2005; Nugis and Lamers, 2000);

- fast rotating stars of $60 M_\odot$ and $10^{-8} - 10^{-5} Z_\odot$ are expected to loose up to 55% of they initial mass (Chiappini et al., 2011; Heger et al., 2000; Meynet and Maeder, 2000; Meynet et al., 2006a,b).

5.2.3 Dense stellar clusters

Alternatively, heavy seeds formation could occur in low-metallicity, dense stellar clusters where, due to the energy equipartition theorem, the most massive

members tend to sink to its center. According to several authors (Begelman and Rees, 1978; Lee, 1987; Quinlan and Shapiro, 1990; Spitzer, 1969; Vishniac, 1978), if such mass segregation occurs within a time-scale of 3 Myr, a very massive star can be assembled, eventually leading to the formation of an intermediate mass BH at the end of its evolution. Omukai et al., 2008 and Devecchi and Volonteri, 2009 calculated that these dense, low-metallicity clusters could form at $z \sim 15$ in dark matter halos of about $10^8 M_\odot$. Moreover, Davies et al., 2011 suggested that runaway merger of stellar mass BHs in clusters driven by free-fall inflow of self-gravitating gas can produce a BH seed above $10^5 M_\odot$. Lupi et al., 2014 found that this route is feasible, peaks at $z < 10$ and it is independent on the metal content of the parent cluster.

5.3 Seeds growth

The calculation in Sec. 5.1 highlights that a $10^2 - 10^3 M_\odot$ BH seed born at $z = 20$ can reach a mass of order $10^7 - 10^8 M_\odot$ at $z = 7$, provided that it always accretes at the Eddington rate (Eq. (4.8)). Anyway, it is not easy to justify the permanent occurrence of the maximum accretion rate: indeed, this scenario is not explained by numerical simulations. Some authors, for example Willott et al., 2010, studied the possibility of the formation of SMBHs starting from small ($M < 100 M_\odot$) seeds, provided they experience several mergers and periods of super-Eddington accretion; in fact, current observations support the fact that sporadic events of super-Eddington accretion can occur at $z \sim 6$: in these conditions, low mass seeds can still generate a SMBH. Others, for example Petri et al., 2012a, explored the possibility that the growth occurs through merging of heavier seeds.

In Sec. 3.2 we explained that the structure formation through the growth of perturbations in the cosmic density field occurs *bottom − up*: smaller structures form first, gradually leading to formation of more massive structures. The detection of high redshift interacting galaxies suggests the possibility that already virialized halos merge to form the big DM halos that embed low-redshift galaxies. We expect that the hierarchical build-up of galaxies through mergers produce black hole binaries, more and more tightened due to the gas dynamical friction, that finally coalesce. Some authors (e.g. Berti et al., 2006) claimed that, with our current experimental instruments, it is feasible to identify SMBHs' seeds during their mergers by the gravitational-wave emission predicted by general relativity. On the theoretical side, the merging of virialized halos can be studied with the mass function formalism described in Sec. 3.2: the probability distribution

function in Eq. (3.18) is converted to a Monte Carlo code through merger-tree procedure (Sec. 3.4).

5.3.1 Direct accretion

SMBH growth from light seeds has already been considered by other authors. For example, Alvarez et al., 2009 studied stellar BH accretion including radiative feedback effect in an adaptive mesh refinement cosmological simulation; due to radiative feedback, their black holes do not gain mass at a sufficiently high rate to grow into a fully-fledged SMBH. Lupi et al., 2016 presented results from a suite of numerical high-resolution simulations aimed at investigating the growth of stellar-mass BHs at super-Eddington accretion; they found that some of their BHs reach $10^3 - 10^4 M_\odot$, making them good seeds candidates. Clearly, due to their computational complexity, numerical simulations can explore only a narrow region of the parameter-space; here we propose a semi-numerical approach that allows a much wider investigation on the physical parameter-space of the problem.

5.3.2 Merging

Many autors (e.g. Natarajan, 2011; Volonteri et al., 2003a,b) considered SMBHs to form by both direct gas accretion and merging of heavy seeds. He exploited the Monte Carlo method based on the Press-Schechter ansatz developed by Parkinson et al., 2008a to statistically simulate mass distribution and merger history of DM halos from $z = 20$ to $z = 6$. Evolution is obtained coupling simple analytical prescriptions to the dark matter merger tree. Petri et al., 2012a, concentrated on the high-mass tail of SMBHs mass function at $z = 6$ and proposed a model in which the hole can grow by a combined action of gas accretion and mergers of both heavy and light seeds: heavy seeds settle in the center of their host galaxy and grow by gas accretion, whereas light seeds are diffuse in rarefied regions and are not efficient at accreting gas. Their aim was to predict the final central object mass, to see if it is consistent with $10^{8-9} M_\odot$ and if it harmonizes with the local empirical correlation between the BH mass and the mass of the galaxy bulge: interestingly, the quantity crucial to SMBHs formation by $z = 6 - 7$ is the fraction of simulated halos that can form heavy seeds.

5.4 Tentative detection and constraints

To understand formation of luminous high-z quasars, would be crucial to detect of their faint progenitors. Weigel et al., 2015 analysed the *Chandra* Deep Field South (CDF-S) in search of fine candidates at $z > 5$, but the estimation of their sources photometric redshift (achieved by combining GOODS, CANDELS and *Spitzer* data) leaves no compelling progenitors. Independently, Georgakakis et al., 2015 combined deep *Chandra* and wide-area/shallow XMMNewton survey fields to investigate evolution of X-ray luminosity function at $3 < z < 5$: extrapolating to $z > 5$ they predict less than one candidate can be found in the CDF-S. Furthermore, Treister et al., 2013 found out that, from a sample of selected $6 < z < 8$ galaxies from the *Hubble Space Telescope* Ultra Deep Field (HUDF) and CANDELS, none is detected in the 4 Ms CDF-S.

Vito et al., 2016 studied the X-ray emission of galaxies in the CANDELS field at redshift $3.5 \leq z \leq 6.5$. In the hypothesis that X-ray emission comes from X-ray binaries, they find model a star formation rate density coherent with UV constraints. They deduced that the bulk of unresolved X-ray emission is emitted by binaries. Nevertheless other source detection methods (Fiore et al., 2012; Giallongo et al., 2015; Pacucci et al., 2016b) suggest that also AGNs X-ray emission has to be accounted for. These results are questioned by other groups (i.e. Cappelluti et al., 2016) and therefore there is not a broad consensus in the scientific community. This topic is currently investigated by several groups and further studies are expected to clarify this issue thoroughly.

6 High-z quasars: a model for their X-ray emission

In this Chapter we build a model for a BH X-ray emission (Sec. 6.1); we the evaluate dimming of the emission by photoelectric and Compton effect in the ISM (Sec. 6.2). In Sec. 6.3 we test this model by a comparison with current quasar observations; the results of this study are published in Gallerani et al., 2017

6.1 Intrinsic flux density

BH accretion efficiently produces electromagnetic radiation. As highlighted in Chapter 4 (Sec. 4.3) the resulting bolometric luminosity shows linear dependence on the black hole accretion rate $\dot{M}_\bullet$:

$$L_{bol} = \dot{M}_\bullet \frac{\eta c^2}{1-\eta}. \tag{6.1}$$

If we assume the standard value of the radiation efficiency $\eta = 0.1$ (Vietri, 2006, Petri et al., 2012a, Volonteri and Stark, 2011 and Frank et al., 2002), the previous equation yields:

$$L_{bol}(\dot{M}_\bullet) = 6.4 \times 10^{45} \left(\frac{\dot{M}_\bullet}{1 M_\odot/\mathrm{yr}} \right) \mathrm{erg} \cdot \mathrm{s}^{-1}. \tag{6.2}$$

The bolometric luminosity L_{bol} is the integral of the spectrum emitted in the accretion disk and the hot corona; to distinguish the luminosity in a particular band of the electromagnetic spectrum (for example the soft and the hard X-ray bands), it is necessary to use a suitable bolometric correction. In particular, bolometric corrections are function of the bolometric luminosity, as the following one (Marconi et al., 2004a):

$$\log[L/L(2-10\mathrm{keV})] = 1.54 + 0.24\tilde{\mathrm{L}} + 0.012\tilde{\mathrm{L}}^2 - 0.0015\tilde{\mathrm{L}}^3, \tag{6.3}$$

$$\log[L/L(0.5-2\mathrm{keV})] = 1.65 + 0.22\tilde{\mathrm{L}} + 0.012\tilde{\mathrm{L}}^2 - 0.0015\tilde{\mathrm{L}}^3, \tag{6.4}$$

where $\tilde{\mathrm{L}} = (\log L - 12)$ and $L = L_{bol}/L_{\odot}$. More recent derivations of bolometric corrections are, for example, Hopkins et al., 2007 and Lusso et al., 2012; a brief discussion of the mutual consistence of these models can be found in Sec. 6.3.

BH X-ray emission is well modelled by a single power law:

$$F_\nu = F_{0_\nu}\left(\frac{\nu}{\nu_0}\right)^{-\alpha} \tag{6.5}$$

where the power index α is experimentally fixed ($\alpha = 0.9 \pm 0.1$, Piconcelli et al., 2005) and the intrinsic flux density F_ν is related to luminosity through the relation (Eq. 2.10):

$$F_\nu = \frac{(1+z) f_\nu L_{bol}}{4\pi d_L(z)^2}, \tag{6.6}$$

$d_L(z)$ is the luminosity distance (see Sec. 2.1.1) and f_ν is the bolometric correction.

Fig. 6.1 shows the X-ray intrinsic flux density F_ν of a BH with accretion rate $\dot{M}_\bullet = 1 M_\odot/\mathrm{yr}$; the shaded region shows the change in the flux density as the slope α spans over $\pm 3\sigma$ around the fiducial value $\alpha = 0.9$.

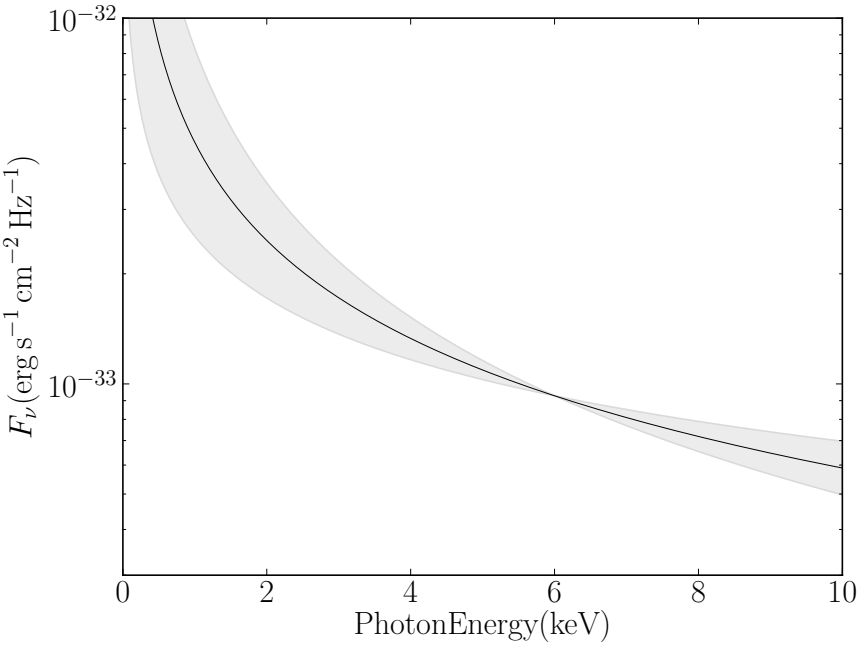

Figure 6.1: Intrinsic flux density for a BH with accretion rate $1 M_\odot/\mathrm{yr}$. The black line corresponds to the fiducial value $\alpha = 0.9$ (Piconcelli et al., 2005), while the shaded region spans over $\alpha \pm 3\sigma$. Since the shaded region depends only on the parameter α, we put it arbitrarily to zero at 6 keV.

6.2 Absorption from obscuring material

We already highlighted (Sec. 4.3.2) that absorbtion of X-ray photons occur in the ISM. The most important involved processes are the photoelectric absorption and the Compton scattering. According to Eq. 4.46, the resulting flux is:

$$F_\nu^{obs} = F_\nu e^{-\tau}, \tag{6.7}$$

being the total optical depth $\tau = (1.2\sigma_T + \sigma_{ph})N_H$ (Yaqoob, 1997), where N_H is the hydrogen column density, σ_{ph} is the photoelectric cross-section and σ_T is the Thomson cross-section.

The expression for τ contains a factor 1.2, because X-rays doubly ionize He and in the gas the number of free electrons is:

$$n_{e^-} = n_H + 2n_{He} = n_H(1 + 2\frac{n_{He}}{n_H}) \simeq n_H(1 + \frac{Y}{2X}), \tag{6.8}$$

where X (Y) the the H (He) mass to the total mass gas and:

$$n_{He} = \frac{M_{He}}{\mu_{He} m_u} \approx \frac{Y\, M_{gas}}{4mp}, \tag{6.9}$$

$$n_H = \frac{M_H}{\mu_H m_u} \approx \frac{X\, M_{gas}}{mp}. \tag{6.10}$$

μ_H , μ_{He} is the atomic weight of H and He respectively and m_u the atomic mass unit. In the primordial Universe $X \approx 0.76$ and $Y \approx 0.24$ and $n_{e^-} \simeq 1.16 n_H$; heavier elements are produced in stars, modifying X and Y. Adopting solar values $X = 0.70$ and $Y = 0.30$, then $n_{e^-} \simeq 1.2 n_H$ (Yaqoob, 1997). Actually, the choice of n_{e^-} does not affect our results: we verified that the contribution of the Compton effect to the total optical depth is about 0.2% at both 1 keV and 10 keV and the process is widely dominated by photoelectric effect.

The photoelectric cross-section has been calculated by Morrison and McCammon, 1983 as a function of energy. The calculation, spans over the range $(0.03 - 10)$ keV and metallicity $Z_\odot^{1982} = 0.0263$, is assumed. Indeed, that was the metallicity of the Sun estimated in 1982. [1] For future purposes, we need a metallicity dependent cross-section: if we break the photoelectric cross-section in three terms and distinguish the H, He and metal contribution, respectively:

$$\sigma_{ph} = \sigma_H + \sigma_{He} + \sigma_{metals}. \tag{6.11}$$

[1] The current value for the solar metallicity is $Z_\odot = 0.0122$, from Asplund et al., 2009

Only σ_{metals} depends on metallicity. We compute σ_H and σ_{He} and yield σ_{metals}^{MMCC} for the metallicity used by Morrison and McCammon, 1983:

$$\sigma_{metals}^{MMCC} = \sigma_{ph} - (\sigma_H + \sigma_{He}). \tag{6.12}$$

However, σ_{metals} is proportional to Z and the relation

$$\sigma_{metals}(Z) = \sigma_{metals}^{MMCC} \left(\frac{Z}{Z_{\odot}^{1982}} \right) \tag{6.13}$$

allows to compute σ_{ph} for any Z. Both hydrogen ionization threshold (≈ 13.6 eV) and the helium second ionization threshold (≈ 54.4 eV) lie much below typical X-ray energy (order of keV), therefore σ_H and σ_{He} are calculated in Born approximation (Shu, 1991): in Born approximation, the photoelectric cross-section for an hydrogen-like atom is:

$$\sigma_{Shu} = \frac{8\pi}{3\sqrt{3}} \frac{\tilde{Z}^4 m_e e^{10}}{c\hbar^3 (\hbar\omega)^3} \sqrt{\frac{48\tilde{Z}e^2}{2a_Z \hbar\omega}}, \tag{6.14}$$

where $\tilde{Z}$ is the atomic number of H and He (1 and 2, respectively), m_e and e the electron mass and charge, c the speed of light, $\hbar$ the reduced Planck constant, and $a_Z = \hbar^2/\tilde{Z} m_e e^2$.

Fig. 6.2 shows the original photoelectric cross-section by Morrison and McCammon, 1983 (dashed line) and the one scaled for the current $Z_{\odot}$. In particular:

- several jumps are present in the function: they correspond to the K-shell energy of the various elements. Indeed, an element contributes to the cross-section only if the energy of the photons is greater than the K-shell energy. The depth of a jump depends both on the abundance of the corresponding element and on its $\tilde{Z}$: the deepest jump correspond to the Fe.

- the cross-section is a decreasing function of the photon energy (note the factor E^3 in Fig. 6.2). Softer X-ray photons are subjected to a heavier attenuation with respect to the harder one.

We then compute the observed flux density $F_\nu^{obs} = F_\nu e^{-\tau}$: the resulting F_ν^{obs} is shown in Fig. 6.3. We assumed the hydrogen column density and the metallicity of the system to be $10^{22}\mathrm{cm}^{-2}$ and 10^{-3} respectively. The red shaded region spans over the values that the flux density takes between $\pm 3\sigma$ around the fiducial value $\alpha = 0.9$ Piconcelli et al., 2005. The attenuation is heavier in the soft X-ray band ($0.5 - 2$keV), being 26% at the center of the band (1.25 keV). Hard radiation

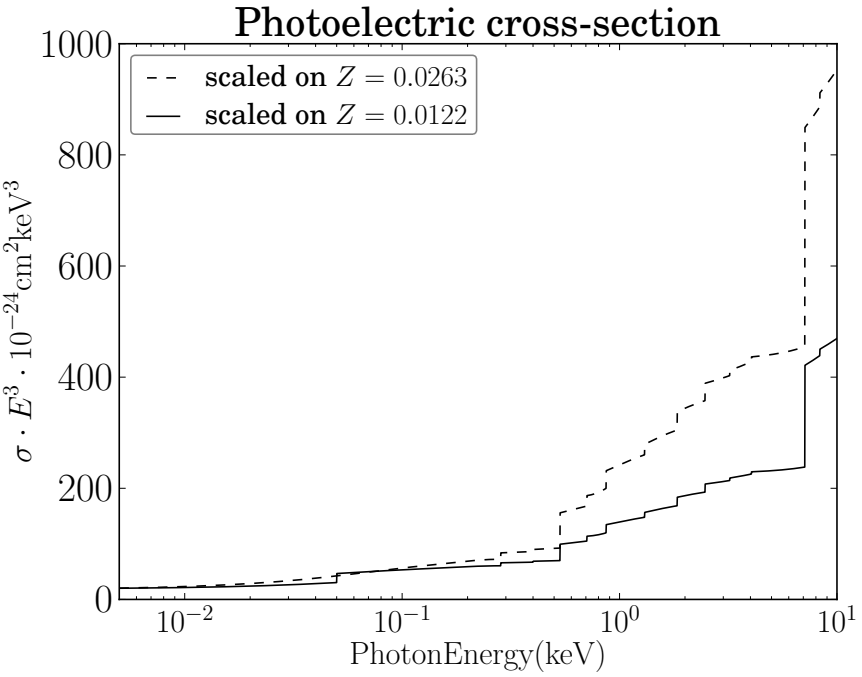

Figure 6.2: The photoelectric cross-section. The dashed line shows the cross-section calculated by Morrison and McCammon, 1983, while the solid line shows the cross-section evaluated as in Eq. 6.12 and scaled for solar metallicity $Z_\odot$.

$(2 - 10\mathrm{keV})$ undergoes a very light attenuation, 0.1% at the center of the band (6 keV). Fig. 6.4 shows the attenuation of the intrinsic flux density of a BH accreting $1 M_\odot\,\mathrm{yr}^{-1}$ as a function of column density (metallicity is 10^{-3}).

6.2.1 Dust

In the calculation of the photoelectric cross-section, the contribution of dust is neglected: according to Fireman, 1974 condensation into grains reduces the photoelectric cross-section. The dust correction is calculated by Ride and Walker, 1977 and Morrison and McCammon, 1983 in the hypothesis that, except H, He, Ne, Ar and 75% of O, all the other elements are condensed in dust: their result is shown in Morrison and McCammon, 1983, Fig.1, page 2, dashed line. Indeed the correction is negligible at low energy, where the attenuation in mainly due to H and He, and at high energy, where the grains are transparent. The dust contribution is relevant only above the carbon edge (≈ 0.3 keV), where the cross-section is reduced by 11%.

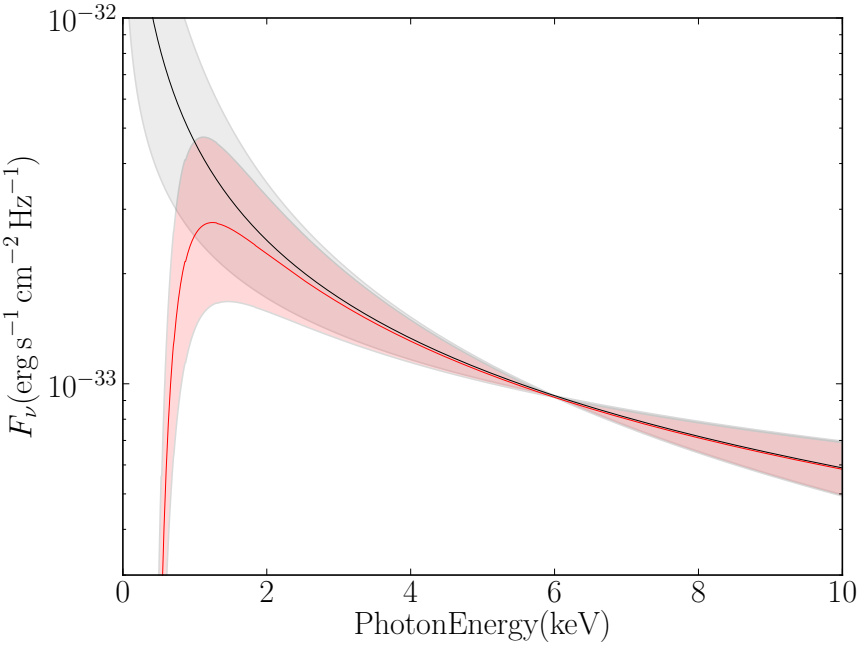

Figure 6.3: Radiative flux density of a BH accreting $1M_\odot/yr$, after the interaction with the surrounding material. Hydrogen column density and metallicity of the system are $10^{22}\mathrm{cm}^{-2}$ and 10^{-3} respectively. The red shaded region spans over $\pm 3\sigma$ around the fiducial value $\alpha = 0.9$ Piconcelli et al., 2005. The attenuation is heavier in the soft X-ray band ($0.5 - 2$keV, 26% at the center of the band). Hard radiation ($2 - 10$keV) crosses the obscuring material with very little attenuation (0.1% at the center of the band).

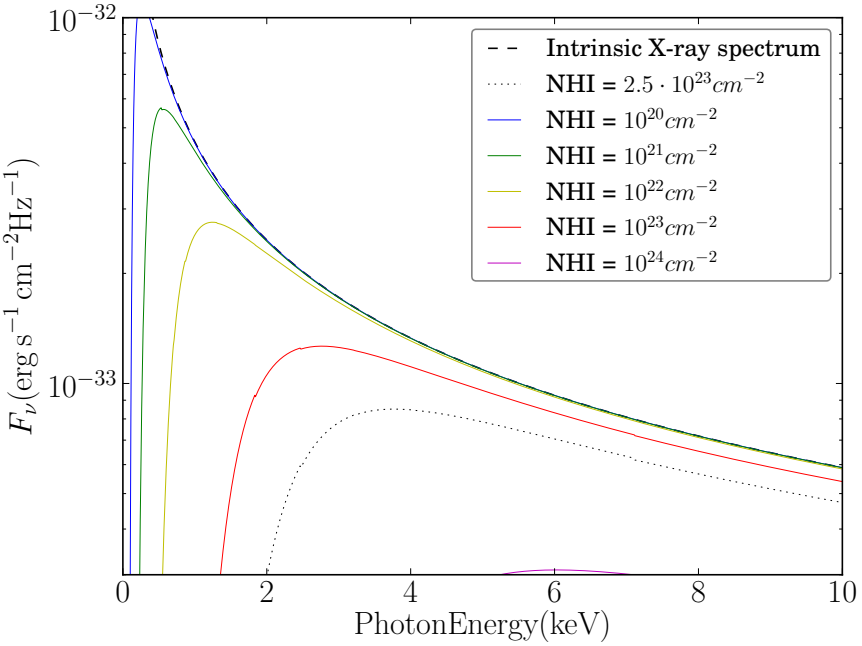

Figure 6.4: Attenuation of the intrinsic flux density of a BH accreting $1M_\odot/yr$ as a function of N_{HI}. The metallicity of the system is 10^{-3}. For hydrogen column densities larger than $N_{HI} = 2.5 \times 10^{23}\mathrm{cm}^{-2}$ (dotted line) the whole emission in the soft X-ray band ($0.5 - 2$keV) is suppressed.

6.3 Testing the model: SDSS J1148+5251

The X-ray emission model developed in this Chapter has several applications. We made a test to verify that our results are in good agreement with quasar observations. We use Chandra Space Telescope (CST) observations of the $z = 6.4$ quasar J1148+5251, detected in 2003 (Fan et al., 2003 and White et al., 2003). J1148+5251 is one of the best studied high-z AGN and it has been observed in a wide range of wavelenghts (Gallerani et al., 2008, Juarez et al., 2009, Riechers et al., 2009, Gallerani et al., 2010, Maiolino et al., 2012, Gallerani et al., 2014, Cicone et al., 2015, Stefan et al., 2015). The observations of Barth et al., 2003, Willott et al., 2003 (Mg_{II} and C_{IV} emission lines) and the ones by Riechers et al., 2009, Gallerani et al., 2014 and Stefan et al., 2015 (CO lines) imply that the quasar is powered by a $M_\bullet = (2-6) \times 10^9 M_\odot$ SMBH and suggest the presence of a surrounding molecular hydrogen mass $M_{H_2} \approx 2 \times 10^{10} M_\odot$ on a scale $R_{H_2} \approx 2.5\,\mathrm{kpc}$.

We present CST data and use our emission model to interpret them, finding independent constraints on $M_\bullet$ and M_{H_2}. The results of this Section are published in the paper Gallerani et al., 2017. We used 42 background-subtracted counts of X-photons from the 2015 September 2^{nd} observation of J1148+5251. We assume:

- the quasar to shine at its Eddington luminosity, $L_{bol} \equiv L_E \propto M_\bullet$ (see e.g. Willott et al., 2003 and Schneider et al., 2015);
- the presence of molecular clouds (MC) uniformly distributed on kpc scales obscuring the line of sight (los).

Hydrogen column density N_H is a function of the properties of a single molecular cloud (mass m_c, density n_c, size r_c) and the size of the region they are confined within R_{H_2}:

$$N_H = 2\mathcal{N}_c^{los} N_c, \tag{6.15}$$

where $N_c = (4/\pi) r_c n_c$ is the cloud column density and $\mathcal{N}_c^{los}$ is the number of clouds we expect to meet along a los,

$$\mathcal{N}_c^{los} = \frac{1}{2} \frac{M_{H_2}}{m_c} \frac{1}{V_{H_2}} \pi r_c^2 R_{H_2}, \tag{6.16}$$

being V_{H_2} the volume occupied by molecular hydrogen. Thus:

$$N_H = 5 \times 10^{22} \left(\frac{M_{H_2}}{10^{10} M_\odot} \right) \left(\frac{R_{H_2}}{2.5\,\mathrm{kpc}} \right)^{-2}. \tag{6.17}$$

Our emission/absorption model depends on several parameters: BH mass $M_\bullet$, bolometric correction f_X, slope of the intrinsic spectrum α for the intrinsic emission, molecular hydrogen mass M_{H_2}, gas metallicity Z ad the size of the H_2 region R_{H_2}. An analysis of the full parameter space is impossible (especially since some of them are degenerate, such as $M_\bullet$ and f_X); we fix most parameters (that we collectively label $\bar{x}$) from previous results and study $M_\bullet$ and M_{H_2} as the only free parameters of the theory. The spectrum power index is $\alpha = 0.9$ from Piconcelli et al., 2005. The bolometric correction (Lusso et al., 2012) $f_X = 230^{+170}_{-100}$. f_X is extrapolated from results at luminosity lower than the one measured for J1148+5251 ($\approx 10^{14} L_\odot$), but it is consistent within $\sim 1\sigma$ with both Marconi et al., 2004a ($f_X = 114$) and Hopkins et al., 2007 ($f_X \approx 150 \pm 50$). High angular resolution observations of the CO(3 − 2) emission (Walter et al., 2004) suggest $R_{H_2} = 2.5 \pm 1.1$ kpc. NIR observations of $3.9 < z < 6.4$ QSOs (Juarez et al., 2009; Nagao et al., 2006) show metallicity $Z = 7 \pm 3 Z_\odot$, but since these observations refer to the BLRs, that may be characterized by larger metallicity with respect to our assumption of 2.5 kpc sphere, we take $Z = Z_\odot$ as the hypothesized lower limit of J1148+5251 metallicity.

We then constrain $M_\bullet$ and M_{H_2}. We fit the theoretical $\mathcal{E}_i = \mathcal{E}_i(M_\bullet, M_{H_2}, \bar{x})$, $i = (1, 2, 3)$ with the observed $\mathcal{O}_i$, minimizing the function:

$$\chi^2 = \sum_{i=1}^{3} \frac{(\mathcal{O}_i - \mathcal{E}_i)^2}{\mathcal{E}_i}, \tag{6.18}$$

$M_\bullet = (2.7 \pm 0.4) \times 10^9 \mathrm{M}_\odot$ and $M_{H_2} = (1.6 \pm 0.7) \times 10^{10} \mathrm{M}_\odot$. The H_2 mass range corresponds to a column density $N_H = (0.8 \pm 0.3) \times 10^{23} \mathrm{cm}^{-2}$. $M_\bullet$ and M_{H_2} are perfectly consistent with previous black hole mass estimates by Willott et al., 2003 and Barth et al., 2003 and the H_2 mass inferred by Walter et al., 2003. Fig. 6.6 shows our emission/absorption model compared with the observed X-ray counts (grey circles) in the source rest frame energy range. Orange squares denote the data re-binned so that that each bin contains at least 12-14 background subtracted counts and the yellow shaded region shows the intrinsic X-ray spectrum predicted if the black hole mass is the best fitting value, within its confidence region. The blue region represents the attenuation model that considers absorption from an hydrogen column density corresponding to the best-fit value of M_{H_2}.

To conclude this study, we changed the fiducial value of all the parameter of the set $\bar{x} = (\alpha, f_X, Z, R_{H_2})$, one by one, leaving the other unchanged. The results of this speculation are reported in Tab. 6.1, that shows that both $M_\bullet$ and M_{H_2} can vary by almost a factor of ten if parameters are altered.

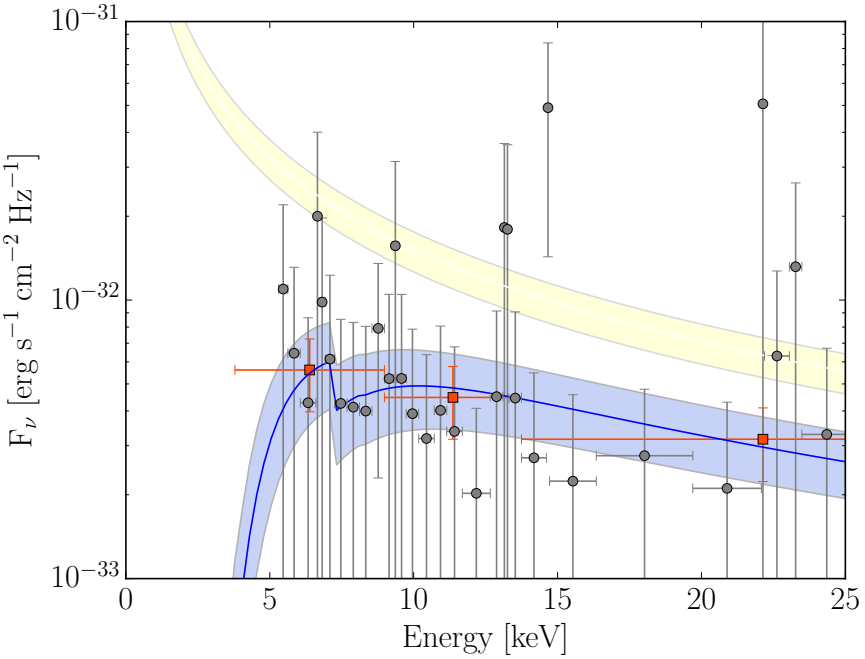

Figure 6.5: Emission/absorption theoretical model compared with the observed X-ray counts (grey circles) in the source rest frame energy range. Orange squares denote the data re-binned so that that each bin contains at least 12-14 background subtracted counts; the yellow shaded region shows the intrinsic X-ray spectrum predicted for an Eddington-luminous quasar with mass of $M_\bullet = 2.7 \pm 0.4 \times 10^9 \mathrm{M}_\odot$; the blue region represents our best fitting attenuation model that considers absorption from an hydrogen column density $N_H = 7.8 \pm 3.0 \times 10^{22} \mathrm{cm}^{-2}$ due to a molecular hydrogen mass of $M_{H_2} = 1.6 \pm 0.7 \times 10^{10} \mathrm{M}_\odot$.

	$M_\bullet$ $[10^9 \mathrm{M}_\odot]$	M_{H_2} $[10^{10} \mathrm{M}_\odot]$	N_{H} $[10^{23} \mathrm{cm}^{-2}]$
Fiducial model	2.7 ± 0.4	1.6 ± 0.7	0.8 ± 0.3
$\Gamma = 3.3$	29 ± 5	6.4 ± 0.7	3.2 ± 0.3
$\Gamma = 1.7$	1.9 ± 0.3	0.8 ± 0.6	0.4 ± 0.3
$f_X = 130$	1.5 ± 0.2	1.5 ± 0.6	0.7 ± 0.3
$f_X = 400$	4.7 ± 0.7	1.6 ± 0.6	0.8 ± 0.3
$Z = \mathrm{Z}_\odot$	3.5 ± 0.5	8 ± 3	4 ± 1
$Z = 10\ \mathrm{Z}_\odot$	2.5 ± 0.4	1.1 ± 0.4	0.5 ± 0.2
$R_{\mathrm{H}_2} = 1.4$ kpc	2.8 ± 0.4	0.5 ± 0.1	0.9 ± 0.3
$R_{\mathrm{H}_2} = 3.6$ kpc	2.7 ± 0.4	3.2 ± 1.6	0.8 ± 0.4

Table 6.1: Best values of the black hole mass $M_\bullet$, molecular hydrogen mass M_{H_2} and hydrogen column density N_{H} obtained for the fiducial model ($\Gamma = 1.9$, $f_{\mathrm{X}} = 230$, $Z = 7\ \mathrm{Z}_\odot$, $R_{\mathrm{H}_2} = 2.5$ kpc), and by varying the adopted parameters.

7 Growth problems of stellar black holes in early galaxies

As highlighted in Chapter 4 the nature of the seeds of the observed high-z (SMBH) is still unknown. Different options have been proposed, involving e.g. intermediate mass direct collapse black holes, but BH remnants of massive stars remain the most natural explanation. To identify the most favorable conditions (if any) for their rapid growth, we study the accretion rate of a $M_\bullet = 100 M_\odot$ BH formed in a typical $z = 10$ galaxy under different conditions (e.g. galaxy structure, BH initial position and velocity). We model the galaxy baryonic content and follow the BH orbit and accretion history for 300 Myr (the time span in $10 > z > 7$), assuming the radiation-regulated accretion model by Park and Ricotti, 2013a.

We find that, within the limits of our model, BH seeds cannot grow by more than 30%, suggesting that accretion on light-seed models are inadequate to explain high-z SMBH. We also compute the X-ray emission from such accreting stellar BH population in the $[0.5 - 8]$ keV band and find it comparable to the one produced by high-mass X-ray binaries. This study suggests that early BHs, by X-ray pre-heating of the intergalactic medium at cosmic dawn, might leave a specific signature on the HI 21 cm line power spectrum potentially detectable with SKA. The results of this study[1] are published in Orofino et al., 2018a.

The Chapter is organized as follows: in Sec.7.1 we present our approach to the problem, Sec.7.2 contains the results and finally Sec.7.3 focuses on the BH emission in the accretion process.

7.1 Model

Our main aim is to model the accretion and growth history of a stellar mass black hole orbiting in a model galaxy at high redshift ($7 < z < 10$).In the following we describe how we set up the galaxy density within the host dark matter halo

[1]The cosmological parameter used in the paper are from Planck Collaboration et al., 2016

(Sec. 7.1.1). Next, in Sec. 7.1.2 and 7.1.3 we focus on black hole accretion and dynamics, respectively.

7.1.1 Host galaxy structure

The black hole accretion rate (i.e. the mass accreted per unit time) strongly depends on the density of the surrounding material. Hence, accretion models have to define the gas distribution in the host galaxy. Our analysis focuses on spherical and disk galaxies, hosted in $z = 10$ dark matter (DM) halos. The structural relations among the virial halo mass (M_{vir}), the virial temperature (T_{vir}) and radius (r_{vir}) at $z = 10$ are as follows:

$$M_{vir} = 0.54 \times 10^8 h^{-1} \left(\frac{T_{vir}}{19800\mathrm{K}} \right)^{3/2} M_\odot \tag{7.1}$$

$$r_{vir} = 1.05\ h^{-2/3} \left(\frac{M_{vir}}{10^8 M_\odot} \right)^{1/3} \mathrm{kpc}, \tag{7.2}$$

where we have assumed a gas mean molecular weight $\mu = 1.2$ appropriate for a neutral, primordial gas. We assume that, within r_{vir}, virialized dark matter halos have an universal (spherically averaged) density profile, according to the numerical simulations of Navarro et al., 1995 (NFW, hereafter):

$$\rho_{NFW}(r) = \frac{\rho_c \delta_c}{cx(1+cx)^2}, \tag{7.3}$$

where $x = r/r_{vir}$, $\rho_c = 3H^2/8\pi G$ is the critical density, and c is the halo concentration parameter taken from Prada et al., 2012; $\delta_c = 200c^3/3F(c)$ is a characteristic overdensity and

$$F(c) = \ln(1+c) - \frac{c}{1+c}. \tag{7.4}$$

Outside the virial radius, a cut-off on the mass is assumed. The values of M_{vir}, r_{vir} and c for the reference $T_{vir} = (0.5, 1, 5, 10) \times 10^4$K DM halos are given in Tab. 7.1. According to Di Matteo et al., 2017 massive BHs (up to $10^8 M_\odot$) at $z = 8$ are hosted in halos with virial temperature above 10^6 K, however these haloes are far less abundant then the 10^{4-5} K haloes considered in this work. The halo mass contained within a radius r,

$$M(r) = \int_0^r 4\pi r'^2 \rho(r') dr' = M_{vir} \frac{F(cx)}{F(c)}, \tag{7.5}$$

$T_{vir}[10^4\mathrm{K}]$	$M_{vir}[10^7 M_\odot]$	$r_{vir}[\mathrm{kpc}]$	c
0.5	1.0	0.6	4.3
1	2.9	0.9	4.1
5	32.7	2.0	4.0
10	92.4	2.9	3.9

Table 7.1: Parameters of dark matter halos considered in this work.

can be translated into a circular velocity

$$v_c^2(r) = \frac{GM(r)}{r} = v_c^2 \frac{F(cx)}{xF(c)}, \tag{7.6}$$

where $v_c^2 = GM_{vir}/r_{vir}$. The escape velocity from radius r is[2]

$$v_e^2(r) = 2\int_r^{r_{vir}} \frac{GM(r')}{r'^2} dr' \approx 2v_c^2 \frac{F(cx) + \frac{cx}{1+cx}}{xF(c)} \tag{7.7}$$

and reaches a maximum $2v_c^2[c/F(c)]$ at the halo center.

After virialization, the gas attains an isothermal equation of state (i.e. $P \propto n^\gamma$, with adiabatic index $\gamma = 1$). This entails a sound speed $c_s = (\gamma k_B T_{vir}/\mu m_p)^{1/2} = 8.3 T_{vir,4}^{1/2}\,\mathrm{km\,s^{-1}}$, where m_p is the proton mass[3]. The gas settles in approximate hydrostatic equilibrium in the dark matter potential, and its density profile is (Makino et al., 1998)

$$\rho_g = \rho_0 \exp\left\{-\frac{\mu m_p}{2kT_{vir}}\left[v_e^2(0) - v_e^2(r)\right]\right\}; \tag{7.8}$$

the central density $\rho_0 = 840 h^{-2}\rho_c$ has been obtained by imposing that the gas mass fraction within r_{vir} is equal to Ω_b/Ω_m. The gas density profile $\rho_g(r)$ in a DM halo with $T_{vir} = 10^4$K is shown in Fig. 7.1.

The dissipational collapse of a fraction of the baryonic component (whose specific angular momentum is assumed to be the same as the DM one, J_{vir}) leads to the formation of a disk. In an almost neutral, primordial composition[4] gas, cooling is essentially provided by H_2 rotational lines, which are excited above 300 K. However, H_2 molecules can be dissociated by an intense Lyman-Werner background (Bromm and Loeb, 2003b); in this case, cooling process is mainly provided by the Lyα emission of neutral H. Such process works above some min-

[2] The approximation in Eq. (7) comes from the integral up to infinity. This approximation slightly overestimates the value of the escape velocity, but the density profile Eq. (8) is correct within 1%.

[3] Throughout the paper we use the notation $Y_x = Y/10^x$

[4] Heavy element and dust cooling become important only for metallicities $Z \gtrsim 10^{-4}$.

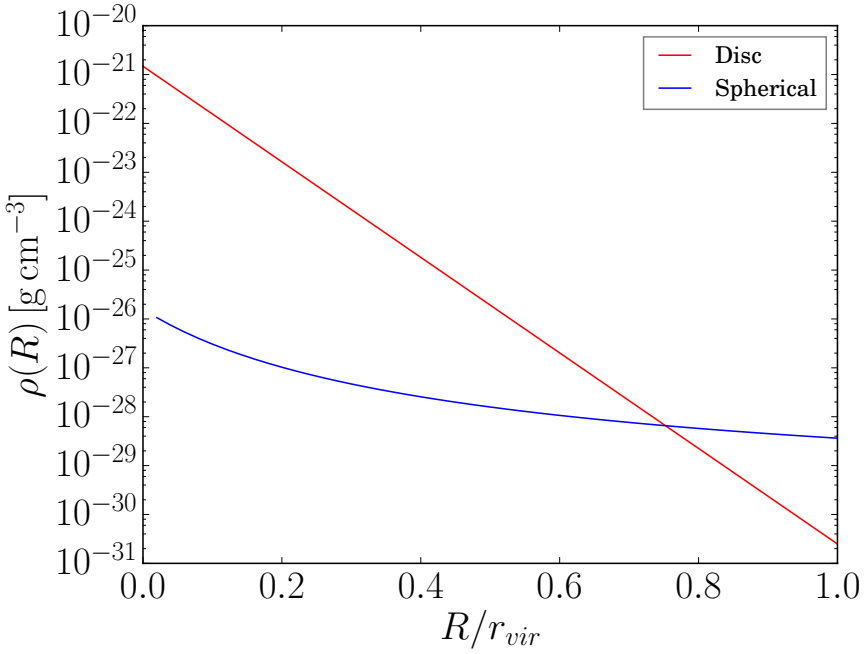

Figure 7.1: Gas density profile in a $T_{vir} = 10^4$K DM halo for the spherical (blue line, Eq. 7.8), and disk-like galaxy model (red line). Note that the disk central density is about 10^5 times higher than the spherical case.

imum temperature $\approx 8000\,\mathrm{K}$. In this work, we assume that the disk can cool down to $T_d = 300\,\mathrm{K}$ due to H_2 cooling. [5] We refer to Omukai et al., 2005 for a detailed description of the cooling process.

Following Mo et al., 1998 and Mao et al., 1998, let us assume the disk settles onto an exponential surface density profile

$$\Sigma(R) = \Sigma_0 e^{-R/R_d}, \tag{7.9}$$

where $R = \sqrt{x^2 + y^2}$ is the radial coordinate on the disk plane, R_d the scale length, and $M_d = 2\pi\Sigma_0 R_d^2$ the total mass of this disk (taken to be 5% of the total mass, see below). We further assume that baryons not ending up in the disk retain the hydrostatic distribution (Eq. 7.8). The disk gravity induces a contraction of the DM, whose modeling is particularly challenging. It is also possible that violent baryonic processes occurring in the galactic disk (e.g. SN feedback) flatten the central DM density cusp into a constant density core (Pontzen and Governato, 2012). However, since the disk mass is 5% of the system total mass, we neglect in this work any variation arising from disk formation on the NFW profile. At $T_d = 300\,\mathrm{K}$, the Toomre stability criterium predicts that the galactic disk would fragment into clumps. In this work, the BH travels in a uniform medium, even

[5] The sound speed in the disk is: $c_{s,d}(T_d = 300\,\mathrm{K}) = 1.5\,\mathrm{km\,s^{-1}}$.

if a more rigorous approach should account for the probability to pass through clumps: nevertheless, we calculated that if the BH spends all the integration time in a clumpy medium ($n \approx 10^2\,\mathrm{cm}^{-3}$, Pallottini et al., 2017) its maximum mass increment would be about 30%, in agreement with the main result of this study. Lupi et al., 2016 state that the large reservoir of dense cold gas in a clumpy medium allows super-Eddington accretion via slim-disk evolution. Fiacconi et al., 2013, Tamburello et al., 2017a, Souza Lima et al., 2017 studied the orbital decay of massive BH pairs in a clumpy circumnuclear disk, important to predict BH dynamics in galaxy mergers remnants. Indeed, our study neglects that the density field of galaxies can be affected by galaxy mergers; for a comprehensive review of the evolution of galaxy structure from first galaxies to the local universe see Conselice, 2014.

The disk properties can be derived in a simple way from those of the halo. The halo rotation can be expressed through the spin parameter,

$$\lambda = \frac{J_{vir}\sqrt{|E|}}{GM_{vir}^{5/2}}, \tag{7.10}$$

which is a measure of the rotational-to-gravitational energy of the system. Numerical simulations show that λ is basically independent of halo mass, redshift and cosmology, and that its distribution for cold dark matter halos is well fitted by a lognormal distribution that peaks at $\lambda = 0.05$ (Barnes and Efstathiou 1987; Macciò et al. 2007). We assume that the disk mass and angular momentum are a fixed fraction of the halo ones, so that:

$$m_d = \frac{M_d}{M_{vir}},\ j_d = \frac{J_d}{J_{vir}}. \tag{7.11}$$

According to Mo et al., 1998, consistency with observational results requires $j_d \approx m_d \approx 0.05$.

For a given rotation curve $v_c(r)$, the angular momentum of the disk is:

$$J_d = \int_0^{r_{vir}} 2\pi\Sigma(r) r^2 v_c(r) dr = 2M_d v_c R_d F_R, \tag{7.12}$$

with

$$F_R = \frac{1}{2}\int_0^{r_{vir}/R_d} u^2 e^{-u}\frac{v_c(uR_d)}{v_c} du, \tag{7.13}$$

$u = r/R_d$, calculated using the fitting formula provided by (Mo et al., 1998),

$$F_R \approx \left(\frac{j_d\lambda}{0.1m_d}\right)^q (1 - 3m_d + 5.2m_d^2)g(c), \tag{7.14}$$

where $q = -0.06 + 2.71m_d + 0.0047(m_d/j_d\lambda)$, and $g(c) = (1-0.019c+0.0002c^2+0.52/c)$. Using the virial theorem, the total energy of the halo is:

$$E = -K = -\frac{M_{vir}v_c^2}{2}F_E, \tag{7.15}$$

where the factor F_E encloses deviations from the energy of an isothermal sphere ($E = -\frac{1}{2}M_{vir}v_c^2$ assuming all particles to be in circular orbits), and depends on the exact shape of the halo density profile; for the NFW profile one finds

$$F_E = \frac{c}{2F^2(c)}\left[1 - \frac{1}{(1+c)^2} - \frac{2\ln(1+c)}{1+c}\right]. \tag{7.16}$$

Combining Eqs. 7.10, 7.11, 7.12 and 7.15, we finally find R_d in terms of m_d and j_d:

$$R_d = \frac{\lambda}{\sqrt{2}}\left(\frac{j_d}{m_d}\right)F_R^{-1}F_E^{-1/2}r_{vir}. \tag{7.17}$$

We assumed the disk to have a constant vertical density $\rho_d(R,z) = \Sigma(R)H^{-1}$, for $|z| \leq H$, and ρ_g (Eq. 7.8), otherwise. The scale height H of the disk can be easily calculated if hydrostatic equilibrium is assumed[6]:

$$\frac{dP}{dz} = -\rho g_z \tag{7.18}$$

Then, the gravitational accerelation at a distance $\sqrt{R^2+z^2}$ from the disk center is:

$$g = \frac{GM(R)}{R^2+z^2}, \tag{7.19}$$

with

$$g_z = \frac{GM(R)}{R^2+z^2}\sin\theta = \frac{GM(R)}{R^2+z^2}\frac{z}{\sqrt{R^2+z^2}} \tag{7.20}$$

where θ is the angle between $\mathbf{g}$ and $\mathbf{r}$. At the disk edge, $R = R_d > z$:

$$g_z \approx \frac{GM(R)z}{R_d^3}, \tag{7.21}$$

[6] This estimate neglects that a rigorous calculation of H should account for the fact that the constant temperature and density vertical profile assumed for the disk do not allow hydrostatic equilibrium to occur.

and Eq. 7.18:

$$dP = -\rho \frac{GM(R_d)z}{R_d^3} dz. \tag{7.22}$$

For $R = R_d$, the z-dependence of ρ can be neglected and the integration between 0 and H gives:

$$P \approx c_s^2 \approx \rho \frac{GM(r_d)z}{r_d^3} \frac{H^2}{2}, \tag{7.23}$$

so that

$$H \approx \sqrt{2 \frac{c_{sd}^2 R_d^3}{GM_d}} \approx \frac{R_d}{6}. \tag{7.24}$$

7.1.2 Black Hole accretion

The accretion theory of a point mass (i.e. a BH) in motion through a uniform medium has been developed by Bondi 1952; Bondi and Hoyle 1944; Hoyle and Lyttleton 1939. The accretion rate $\dot{M}_\bullet$ depends on both the BH-gas relative velocity[7], $v_\bullet$, and the gas density, ρ. In practice, radiation emitted in the accretion process limits the accretion itself by exerting a radiation pressure onto the infalling gas. Hence, the maximum accretion rate achievable, $\dot{M}_E$, is the one that produces the Eddington luminosity $L_E = 1.5 \times 10^{38} (M_\bullet / M_\odot)\,\mathrm{erg\,s^{-1}}$.

To account for feedback-limited accretion we build upon the results by Park and Ricotti, 2013a (hereafter PR; see also Park and Ricotti, 2011, 2012) obtained assuming spherically symmetric accretion and a radiative efficiency $\eta = L/\dot{M}c^2 = 0.1$. In their simulations, PR find that the accretion rate is strongly dependent on $v_\bullet$, depending on which three different regimes have been identified:

$$\dot{M}_\bullet = \begin{cases} 0.01 T_4^{5/2} n_5^{1/2} \dot{M}_B & v_\bullet < c_s \\ 0.7 \frac{G^2 M_\bullet^2}{c_{s,in}^3} \rho (v_\bullet / 2c_{s,in})^2 & c_s < v_\bullet < 2c_{s,in} \\ \frac{G^2 M_\bullet^2}{c_{s,in}^3} \rho (1 + v_\bullet^2 / c_{s,in}^2)^{-3/2} & v_\bullet \gg 2c_{s,in}, \end{cases} \tag{7.25}$$

where $\dot{M}_B = \pi e^{3/2} \rho G^2 M_\bullet^2 c_s^{-3}$ is the Bondi rate, $n = \rho / \mu m_p$, and $c_{s_{in}} = (\gamma k_B T_{in} / \mu_{in} m_p)^{1/2}$ is the sound speed in the cometary-shaped HII region around the BH. We assume $\mu_{in} = 0.6$ (fully ionized primordial gas) and $T_{in} = 4 \times 10^4$K, corresponding to a spectral index $\alpha = 2$ if a single power law $\nu^{-\alpha}$ for the black hole emission spec-

[7] In our approximation the gas in the galaxy is static and $v_\bullet$ coincides with the BH velocity. Nevertheless, even if $v_\bullet$ should account for the rotational velocity of the gas disk, the wide range of simulated BH velocities (Sec. 7.1.3) covers the discrepancy from the BH-gas relative velocity.

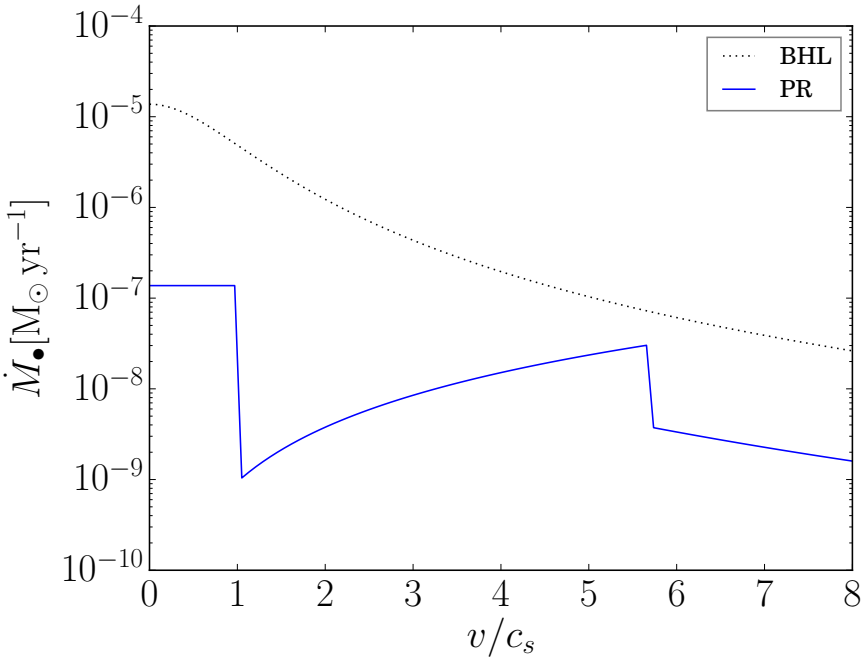

Figure 7.2: BH accretion rate $\dot{M}_\bullet$ from Eq. 7.25 (PR) compared to the Bondi-Hoyle-Lyttleton model (BHL) Eq. 7.30. An ambient gas density $n = 10^5\,\mathrm{cm}^{-3}$, temperature $T = T_{vir} = 10^4$ K and $M_\bullet = 100 M_\odot$ are assumed.

trum is assumed (Park and Ricotti, 2011). As can be appreciated from Fig. 7.2, the accretion rate decreases by several orders of magnitudes as $v_\bullet > c_s$ (i.e. the motion is supersonic with respect to the ambient medium), when PR predicts the formation of a dense gas shell behind the ionization front. The accretion rate has another discontinuity for $v_\bullet = 2c_{s_{in}}$, when the ionized layer becomes rarefied.

The previous formulae implicitly assume that the accretion flow on the black hole is spherically symmetric. However, under some conditions, it is possible that in the vicinity of the black hole the gas is funneled into an accretion disk. The most important condition leading to an accretion disk formation is that the captured material specific angular momentum is larger than the one of the innermost stable orbit $J_{ISCO} = \sqrt{3} c r_g$ for a Schwarzschild black hole ($r_g = 2GM_\bullet/c^2$ is the gravitational radius).

Although disk formation around a moving black hole is still controversial (see for example Chisholm et al., 2003 and Davies and Pringle, 1980 for arguments in favor of disk-like or spherical geometry, respectively) we adopt a spherical accretion model on the basis of the arguments given in Beskin and Karpov, 2005. These authors conclude that, for nearly any $v_\bullet$, neither ISM turbulent motions nor density fluctuations can prevent the onset of a spherical accretion regime. As an example of stellar-BHs disk-like accretion with the PR accretion model, we

nevertheless refer to Wheeler and Johnson, 2011.

7.1.3 Black hole dynamics

As discussed in Sec. 7.1.2, the accreted mass, ΔM, depends on the gas density, ρ, and the BH velocity, v, at each point along its orbit, in turn determined by the galaxy gravitational potential produced by the assumed matter distribution (Sec. 7.1.1). We start by writing the equation of motion which yields the BH acceleration,

$$\ddot{\mathbf{r}} = -\nabla\phi(r) - \frac{\dot{M}_\bullet}{M_\bullet}\mathbf{v}_\bullet, \tag{7.26}$$

where the gravitational potential, ϕ, is given by the Poisson equation: $\nabla^2\phi = 4\pi G\rho$. The gravitational potential contains contributions from two components: (a) the spherically symmetric distribution of the dark matter halo (potential ϕ_h), and (b) the baryonic disk (ϕ_d). We neglect the subdominant contribution from the fraction of uncollapsed baryons residing in the halo.

The halo-related potential is simply

$$\phi_h(r) = -\frac{GM(r)}{r}. \tag{7.27}$$

To compute the potential of the second component we adopt a thin-disk approximation, yielding

$$\phi(r,z)_d = -2\pi G\int_0^\infty J_0(kr)\hat{\Sigma}(k)e^{-k|z|}dk, \tag{7.28}$$

where $J_0(x)$ is the zero-th order Bessel function, and $\hat{\Sigma}(k) = \int_0^\infty J_0(kr)\Sigma(r)rdr$ is the Hankel (or Fourier-Bessel) transform of Σ (Toomre, 1963). Finally, by combining Eqs. 7.28 and 7.9 we get

$$\phi(r,z)_d = -2\pi G\Sigma_0 R_d^2\int_0^\infty \frac{J_0(kr)e^{-k|z|}}{[1+(kR_d)^2]^{3/2}}dk. \tag{7.29}$$

The plot of the potentials for the two components, along with the total one, $\phi = \phi_h + \phi_d$ in the disk plane as a function of galactocentric radius, R, is shown in Fig. 7.3.

The trajectory of a particle in a given potential well is completely determined by three parameters (reduced to two for spherically symmetric problems). Given the initial conditions (IC), we solve Eq. 7.26 using a leapfrog integration over a

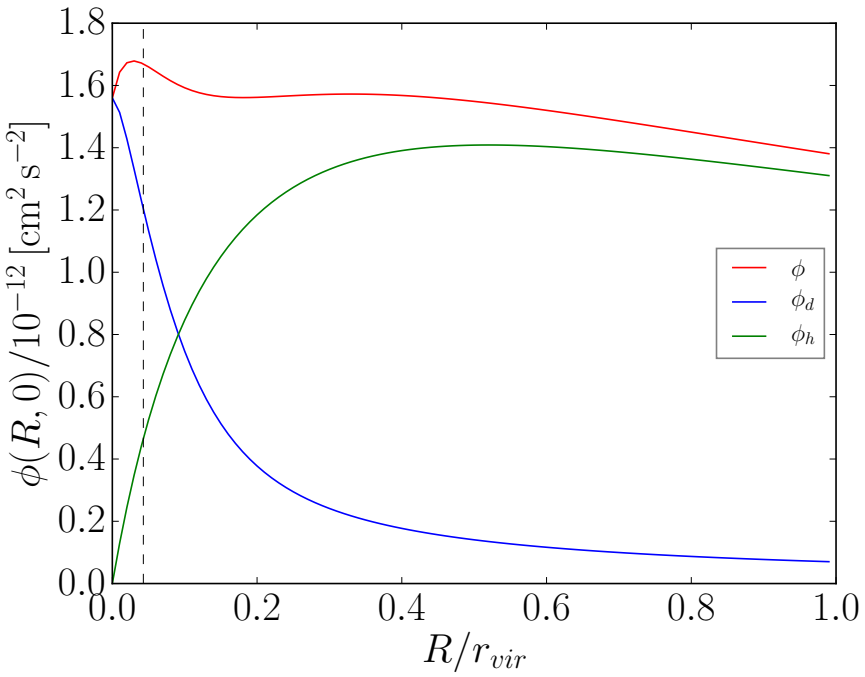

Figure 7.3: Total gravitational potential ϕ (red) as a function of galactocentric radius in the disk plane. Also shown are the disk (blue) and halo (green) contributions. The vertical dashed line marks the disk scale length R_d.

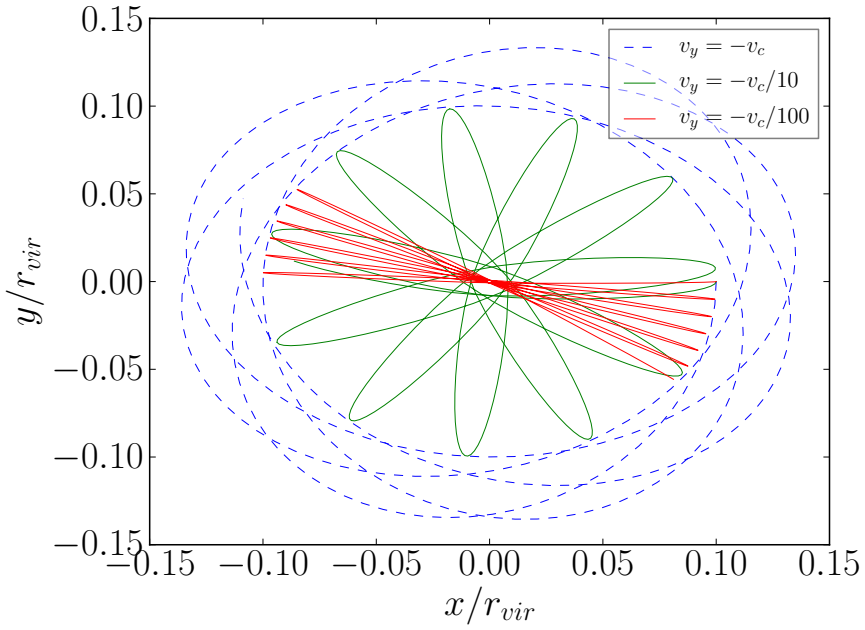

Figure 7.4: Example of orbits in a spherical galaxy hosted by a $T_{vir} = 10^4$K DM halo, starting from different initial conditions.

total integration time[8], $t_{\rm max} = 300\,{\rm Myr}$ with a typical time step of $dt = 10^3{\rm yr}$.

For the spherical case, we consider without loss of generality all orbits to lie on a plane (x, y) perpendicular to the rotation axis z. We initialize the BH position as $x = r_0$, $y = 0$, with initial velocity components $v_x = 0$, $v_y = v_0$. The values of r_0 and v_0 are bound to be $0 < r_0 < r_{vir}$ and $0 < v_0 < v_c$, respectively. The second bound implies that the initial velocity is smaller than the escape velocity in Eq. 7.7, and the orbital period $T_r \lesssim t_{\rm max}$. We verified that, with these IC, the BH never enters in the accretion regime $v_\bullet > 2c_{s_{in}}$ (see Eq. 7.25). Fig. 7.4 shows an example of BH orbits in a spherical galaxy hosted in a $T_{vir} = 10^4{\rm K}$ halo, starting from $r_0 = 0.1\,r_{vir}$ and $v_0 = [1,\ 0.1,\ 0.01]v_c$.

When a disk is present in addition to the halo, spherical symmetry does not hold. Then we need to specify three, rather than two, orbital parameters. These are: $\mathbf{r_0} = (x_0, 0, x_0 \tan\alpha), \mathbf{v_0} = (0, v_0, 0)$. Unless differently stated, we take the angle $\alpha = 0$. For simplicity, and to allow a direct comparison between the spherical and the disk+halo cases, no radial component of the initial velocity is considered in this study.

7.2 Results

We applied the method described in Sec. 7.1 to evaluate the mass accreted by a $100 M_\odot$ black hole as a function of time along its orbit. We are in particular interested in assessing how the rate depends on the IC of the motion and whether significant growth can occur. We have investigated an extended range halos with virial temperatures spanning the range $5000 < T_{vir} < 10^5{\rm K}$ DM halos. However, we found very little dependence of the results on T_{vir}; for sake of brevity, then, we limit the following discussion to the case $T_{vir} = 10^4{\rm K}$ only.

In Sec. 7.2.1 and 7.2.2, we present the results for the spherical and disk-like galaxy model, respectively.

7.2.1 Spherical galaxies

Our investigation allows a statistical description of the mass accreted by the 100 $M_\odot$ BH during the integration time $t_{\rm max} = 300$ Myr as a function of the orbital ICs. We recall that this time span implies that for a BH observed at $z = 7$ the accretion phase has initiated at $z = 10$. For the spherical galaxy case analyzed in this Section, the results are summarized in the left panel of Fig. 7.5.

[8] We recall that the age of the universe is $5 \times 10^8{\rm yr}$ and $8 \times 10^8{\rm yr}$ at $z = 10$ and $z = 7$, respectively.

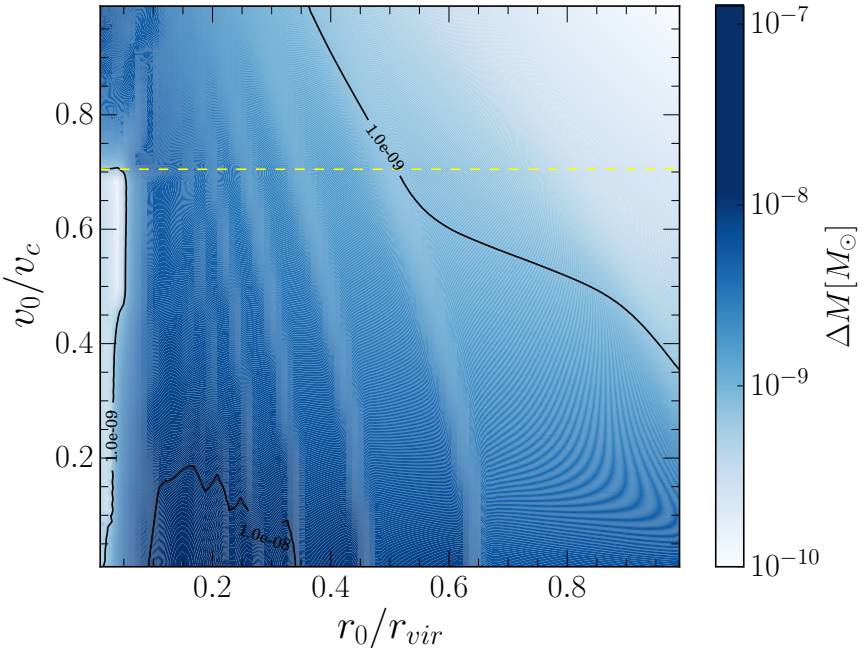

(a)

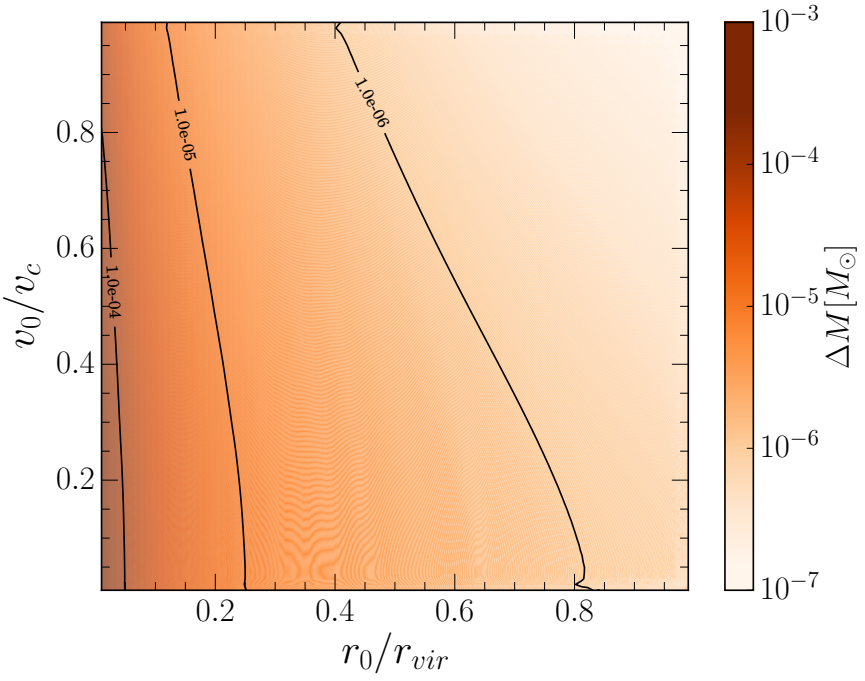

(b)

Figure 7.5: *Left panel:* mass accreted in 300 Myr by a $100M_\odot$ BH (spherical galaxy model) as a function of the orbital ICs (r_0, v_0). The yellow dashed line corresponds to the sonic point at which $v_0 = c_s$; below (above) the line the BH is subsonic (supersonic) corresponding to efficient (inefficient) accretion as shown in Fig. 7.2. Maximal accretion ($\Delta M \lesssim 10^{-7} M_\odot$) is attained when the BH traverses at subsonic speed the central regions of the galaxy; this mainly occurs for close subsonic ICs. Black contour lines join points of equal ΔM (10^{-9} and $10^{-8} M_\odot$ in this case). *Right panel:* same as left panel but with radiative feedback turned off. Accretion occurs at the standard Bondi-Hoyle-Lyttleton rate. $\Delta M \lesssim 10^{-3} M_\odot$ is much higher than in the model included feedback, but still negligible with respect to the initial BH mass.

The accretion rate is maximal when the BH moves at subsonic speed into the densest central regions of the galaxy. However, even under these favorable conditions we find that the mass gained during the evolution is very limited, amounting to only $10^{-7}M_{\odot}$, certainly insufficient to build a SMBH by $z \approx 7$. In these cases, the mean accretion rate is at most $\langle \dot{M}_{\bullet} \rangle = \Delta M/t_{max} < 10^{-8}\dot{M}_E$. The rest of the parameter space, with ICs corresponding to central subsonic orbits or distant supersonic ones, virtually does not allow any growth ($\Delta M \approx 10^{-10}M_{\odot}$).

It is interesting to check whether such BH inability to accrete matter descends from feedback. The answer is encoded in the lower panel of Fig. 7.5, in which we have repeated the same experiment shutting off radiative feedback. A standard Bondi-Hoyle-Lyttleton accretion rate (Bondi, 1952; Bondi and Hoyle, 1944; Hoyle and Lyttleton, 1939),

$$\dot{M}_{BHL} = \pi e^{3/2} \frac{G^2 M_{\bullet}^2}{(c_s^2 + v_{\bullet}^2)^{3/2}} \rho, \tag{7.30}$$

has been assumed in this case. Although indeed feedback causes a quenching of the accretion rate by 3-4 orders of magnitude, even neglecting its effects does not allow a sensible growth of the BH ($\Delta M \approx 10^{-3}M_{\odot}$). Thus, we can conclude that in galaxies not developing a central disk condensation, BH growth is essentially impossible. Hence, we next examine the disk galaxy case.

7.2.2 Disk galaxies

In principle, the high gas densities (up to $n \approx 10^3\,\mathrm{cm}^{-3}$) found in the disk favor high accretion rates. However, the limiting factor to such efficient accretion is the residence time of the BH in the disk. The maximum accretion rate is expected for orbits in which the residence time is 100%; these are the orbits lying in the disk plane ($\alpha = 0$). The results of this particular case are shown in the left panel of Fig. 7.6a. In this case, much larger accretion rates with respect to the spherical galaxy case can take place, leading to a small maximal mass growth $\Delta M \approx 10^{-2}M_{\odot}$, so that the mean accretion rate is at most $\langle \dot{M}_{\bullet} \rangle = \Delta M/t_{max} < 10^{-3}\dot{M}_E$.

If the orbit is instead inclined at an angle α with respect to the disk plane the situation changes only slightly, as shown in Fig. 7.7. We note that the BH trajectory is vertically contained in the baryonic disk if the inclination angle is $\alpha_d = \tan^{-1}(H/R_d) \approx 10^o$; thus, smaller inclination angles give the same result as the $\alpha = 0$ one. Depending on the initial position and velocity, small ($\lesssim 3$) variations are predicted (Fig. 7.7) as a function of α. In particular, orbits starting near the center with low velocity show an increase in ΔM for large inclinations, since the BH spends a larger fraction of the integration time in an

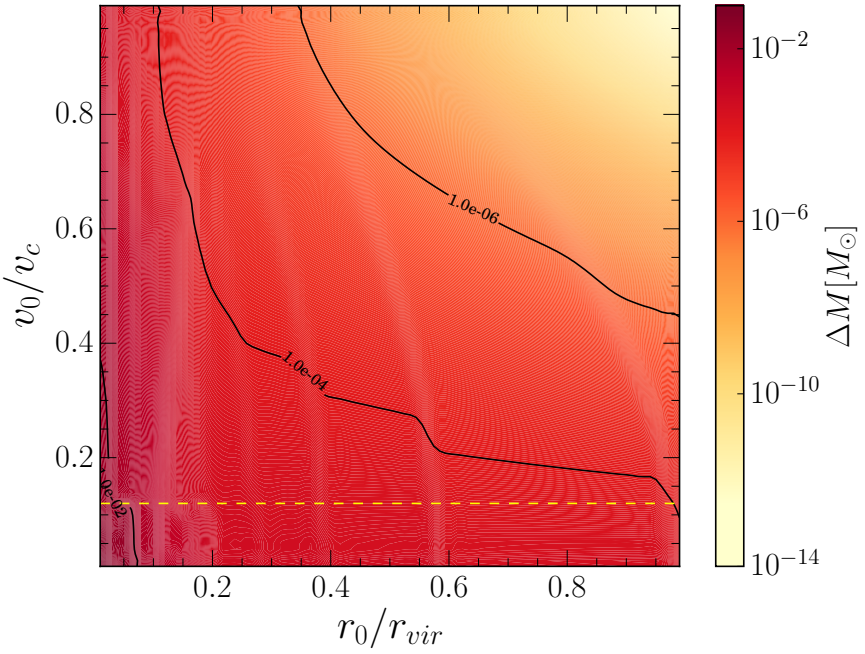

(a)

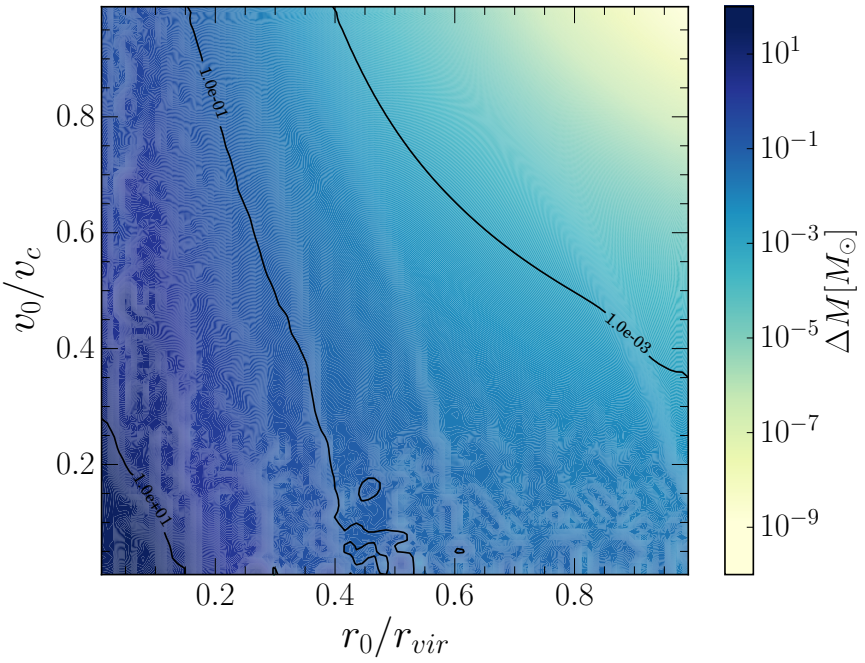

(b)

Figure 7.6: Fig. (a) and (b) show the same as Fig. 7.5 but for the disk galaxy case.

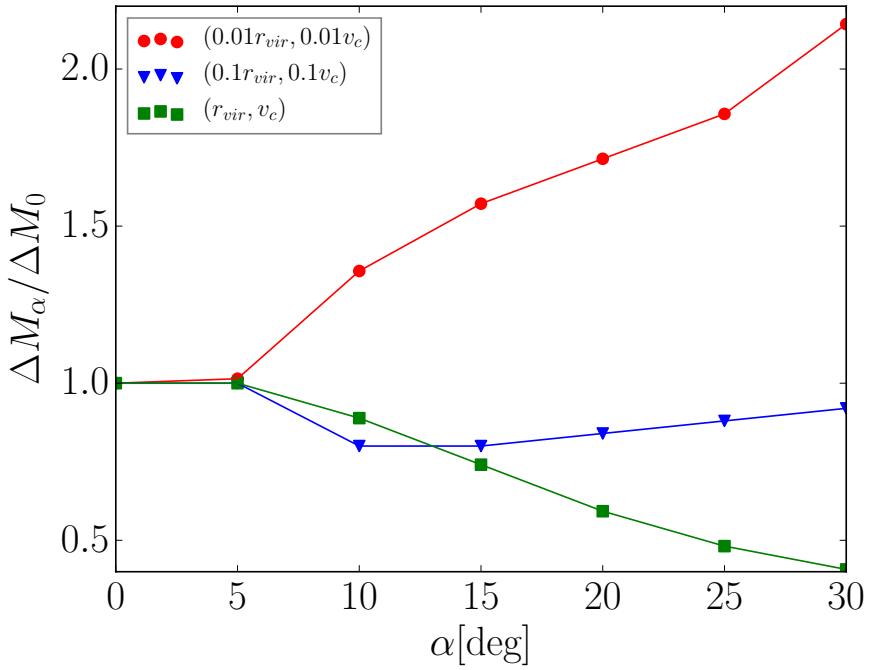

Figure 7.7: Relative mass increment for orbits at different inclination angle α with the disk plane with respect to the orbit at $\alpha = 0$ for different initial conditions, (r_0, v_0) as shown in the inset.

efficient accretion regime (as can be deduced from Eqs. (7.27) and (7.29), the BH experiences a stronger acceleration for large inclinations).

As already noted, velocity seems to play the most important role, with subsonic orbits leading to somewhat larger accretion rates and mass growth, yet still largely insufficient to support the idea that SMBH can grow out of stellar mass BHs orbiting in primordial galaxies.

Finally, we discuss the case in which a standard Bondi-Hoyle-Lyttleton accretion rate (Eq. 7.30) is assumed (Fig. 7.6a, right panel). As in the spherical case, radiative feedback quenches accretion by 3-4 orders of magnitude and, even if an increment $\Delta M \approx 35 M_\odot$ can be achieved under the most favorable ICs, this is largely insufficient to grow a SMBH from a $100 M_\odot$ one.

7.3 Emission

Although we have seen in the previous Section that, under the conditions explored here, BH growth is extremely slow, it is nevertheless important to predict what level of radiative emission is produced during the evolution. X-ray photons produced by early galaxies ionize neutral atoms in the IGM, ejecting high-energy photoelectrons that ionize or collisionally excite other atoms whose energy is

$(m_1, m_2)[M_\odot]$	$(M_1, M_2)[M_\odot]$	$N_\bullet/N_\bullet^{tot}$
$25, 140$	$2, 100$	98%
$260, 500$	$150, 500$	2%

Table 7.2: Mass distribution of the stellar black holes expected in a $T_{vir} = 10^4$K halo at $z = 10$. The 98% sprouts in the $(2, 100)M_\odot$ interval, while only 2% is heavier than $100M_\odot$. Stars are assumed to form with a Salpeter (1955) IMF and to leave a BH remnant according to Heger et al. (2002).

eventually thermalized by scattering with other electrons. Such process deposits 1/3 of the emitted energy as heat (Furlanetto and Stoever, 2010; Shull and van Steenberg, 1985; Valdés et al., 2007). This preheating of the neutral medium can leave well defined signatures on the 21 cm line power spectrum (e.g. Evoli et al. 2014; Mesinger et al. 2013).

In this Section, we want to clarify whether X-ray emission of stellar BHs in primordial galaxies can produce detectable signature on the 21-cm signal from the high-z universe. We focus on the disk galaxy case since accretion rates are larger, and consequently emission is more conspicuous.

The number $N_\bullet$ of stellar mass BHs in the galaxy can be estimated assuming that stars form according to a Salpeter initial mass function (IMF) $\phi(m) \propto m^{-2.35}$ between $(1 - 500)M_\odot$. Stars with $m > 8M_\odot$ explode as supernovae with a frequency $\nu_{SN} \approx 1/100M_\odot$; among them, those more massive than $m > 25M_\odot$ leave a black hole remnant. According to Heger et al., 2002, stars with mass between 25 and $140M_\odot$ leave BHs between 2 and $100M_\odot$, while stars heavier than $260M_\odot$ leave BHs up to $500M_\odot$. Between 140 and $260M_\odot$ theoretical forecasts predict stars to explode as pair-instability supernovae, leaving no remnants.

With these assumptions, in a DM halo of virial mass $M_{vir} = 2.9 \times 10^7 M_\odot$ (corresponding to $T_{vir} = 10^4$K) we expect a number of BHs with mass between M_1 and M_2 (descendants of stars with mass between m_1 and m_2):

$$N_\bullet(M_1, M_2) = M_* \, \nu_{SN} \left(\frac{\int_{m_1}^{m_2} \phi(m) dm}{\int_8^{500} \phi(m) dm} \right), \tag{7.31}$$

where $M_* = M_{vir} \, (\Omega_b/\Omega_m) \, f_* \approx 5 \times 10^5 M_\odot$ for a star formation efficiency $f_* = 10\%$. We find $N_\bullet^{tot} \approx 1000$ BHs with mass between 2 and 500 $M_\odot$. Their mass distribution is shown in Tab. 7.2: the majority of the BH population settles between $(M_1, M_2) = (2, 100)M_\odot$ and only 2% is between 150 and $500M_\odot$.

Sampling the IMF and using the results from Heger et al., 2002, we assign a mass to this population of 1000 BHs and generated the initial conditions of their motions in the galaxy (r_0, v_0, α) stochastically. We followed their accretion rate

$\dot{M}_\bullet(t)$ and integrated Eq. 4.26 between $[0.5, 8]$ keV, obtaining their cumulative X-ray emission as a function of time (Fig. 7.8). The X-ray luminosity flickers around a mean value of $\bar{L}_X = 6 \times 10^{36}\mathrm{ergs}^{-1}$, with the spikes corresponding to passages through the densest parts of the disk. We thus obtain the X-ray luminosity of stellar black holes per stellar unit mass formed:

$$\lambda_X = \bar{L}_X / M_* \approx 10^{31} \mathrm{erg\,s^{-1}\,M_\odot^{-1}}. \tag{7.32}$$

To estimate the stellar mass formed at a given time, we assume that the Star Formation Rate (SFR) ψ of the galaxy rises with time as

$$\psi(z) = \psi_0 \left(1 - e^{-t(z)/\tau}\right), \tag{7.33}$$

where $t(z)$ is the age of the universe at redshift z with an unknown timescale $\tau > 0$ which parametrizes the uncertainty on the exact shape of $\psi(z)$. However, we set ψ_0 so that, for each value of τ, the SFR is (Yue et al., 2015) $10^{-3} M_\odot \mathrm{yr}^{-1}$ at $z = 10$. It turns out that even allowing τ to vary in a very broad range, the total stellar mass in the galaxy is:

$$M_* = \int_\infty^{10} \psi(z) dz \approx (2 - 5) \times 10^5 M_\odot, \tag{7.34}$$

consistent with $f_* = (M_*/M_{vir})\,(\Omega_m/\Omega_b) \approx 0.1$, previously assumed.

In Fig. 7.9 we show (red shaded region) the expected BHs $[0.5, 8]$ keV luminosity obtained as

$$L_X(z) = \lambda_X M_*(z). \tag{7.35}$$

It is interesting to compare such luminosity with the one expected from X-ray binaries (L_{XRB}) in [0.5-8] keV in the same galaxy. The local correlation with the SFR is (Mesinger, 2015; Mineo et al., 2012):

$$L^0_{\mathrm{XRB}} = 3 \times 10^{39}\ \mathrm{erg\,s^{-1}} \left(\frac{\psi}{\mathrm{M_\odot yr^{-1}}}\right), \tag{7.36}$$

In general, high-z galaxies are believed to show a lower metallicity which might lead to higher X-ray production efficiencies. Dijkstra et al., 2012 (Lehmer et al., 2016) found that the local law (Eq. 7.36) evolves up to $z = 3$ ($z = 7$) as follows:

$$L_{\mathrm{XRB}}(z) \approx L^0_{\mathrm{XRB}}(1 + z). \tag{7.37}$$

In Fig. 7.9, the XRB emission is shown with a blue line.

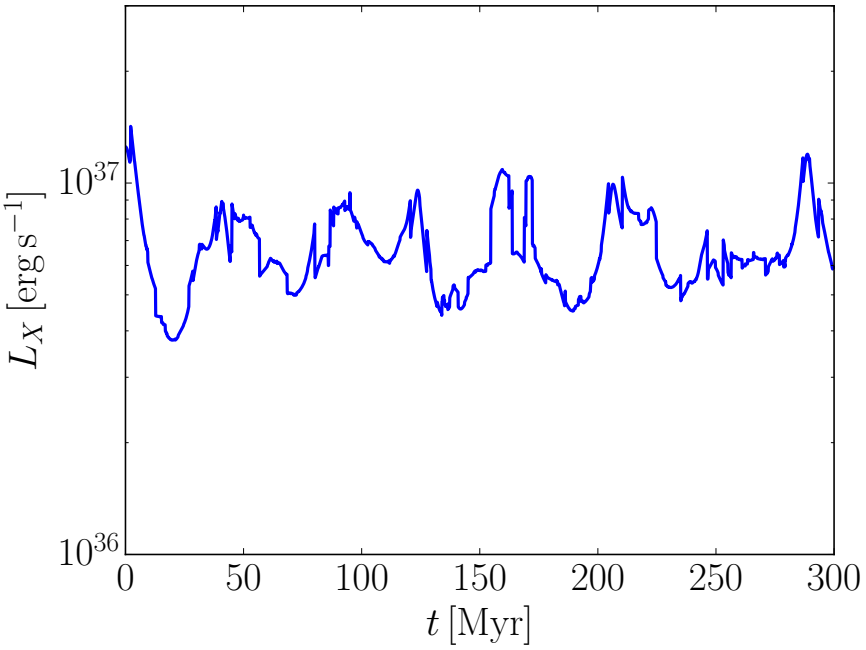

Figure 7.8: Cumulative $[0.5-8]$ keV emission of a 1000 stellar black holes (sBH) sample hosted in the modelled galaxy as a function of time: it flickers around a mean value of $\bar{L}_X = 6 \times 10^{36}$ergs^{-1}, with the spikes corresponding to passages through the densest parts of the galactic disk.

To conclude, we show the BH and XRB contribution to the galaxy SED at redshift $z = 7$ (Fig. 7.10); the red line represents the cumulative synchtrotron spectrum of the BH population predicted by Eq. (4.26); the blue line corresponds to XRB. According to Rephaeli et al., 1995, Swartz et al., 2004, Mineo et al., 2012, the intrinsic XRB spectrum follows a power-law $\nu L_\nu \propto \nu^\alpha$, with $\alpha \approx 0.7-1.0$ and a cut-off above 10 keV (Bachetti et al., 2013; Miyawaki et al., 2009). Following Pacucci et al., 2014 we take $\alpha = 0.8$ as the fiducial value; then we normalized the SED so that it reproduces $L_{\rm XRB}(z = 7)$ predicted by Eq. (7.37) with $\psi = 10^{-3} M_\odot$/yr.

Fig. 7.9 and 7.10 lead to the conclusion that X-ray emission from stellar mass BH is comparable to that of XRB. Thus, the result of this study suggests that the stellar BH energy input should be included in IGM heating computations relevant to the HI 21 cm line signal from cosmic dawn.

7.4 Summary and discussion

We studied the accretion rate of a $M_\bullet = 100 M_\odot$ BH formed in $z = 10$ galaxies under different conditions (e.g. galaxy structure, BH initial position and velocity). We modelled the galaxy baryonic content and followed the BH orbit and accretion

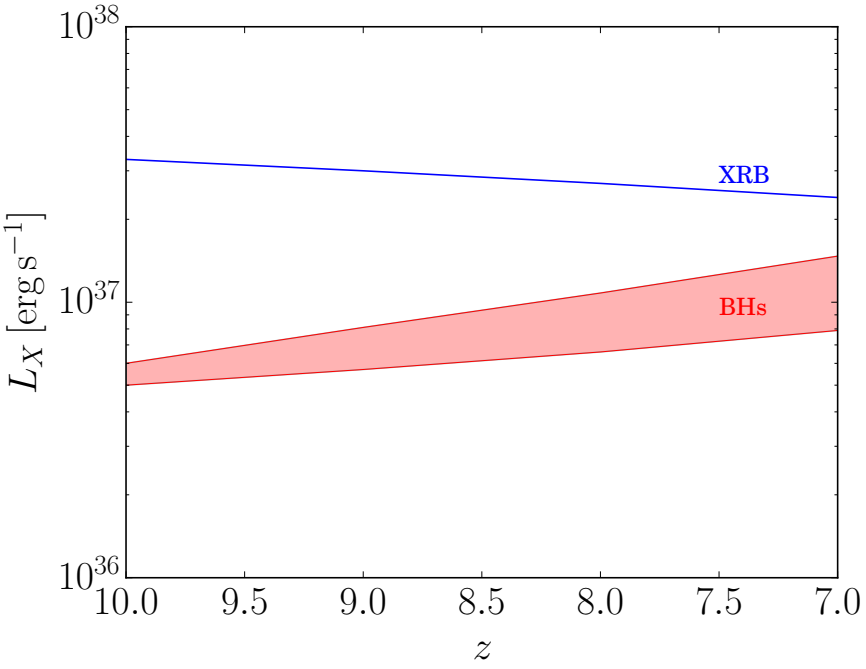

Figure 7.9: [0.5-8] keV emission of the stellar BHs population (red shaded region), compared to the one of the XRB (blue line), as a function of redshift. XRB contribution at high-z relies on the polynomial law eq. 42 extrapolated up to $z = 10$. The error on BHs emission highlights the uncertainty on the exact functional shape of the SFR $\psi(z)$.

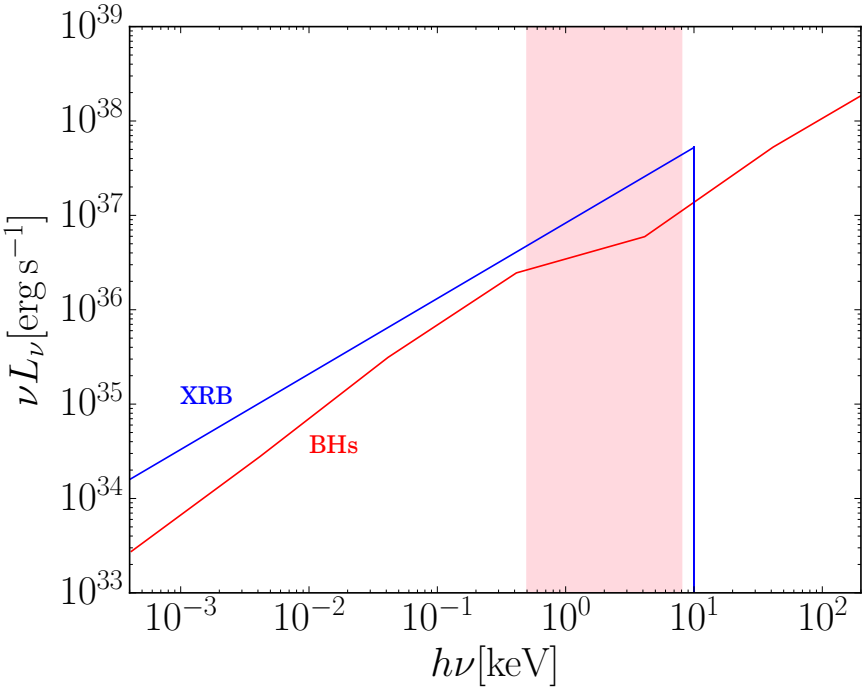

Figure 7.10: Comparison between the BHs cumulative SED (Eq. 4.26) and the XRB SED (Pacucci et al., 2014) at z=7. It is noteworthy that our model predicts BHs to emit above 10 keV, where XRB spctrum is indeed observed to crash. The pink shaded region corresponds to the energy interval [0.5-8] keV.

history for 300 Myr (time interval between $z = 7$ and $z = 10$), assuming the radiation-regulated accretion model by Park and Ricotti, 2013a. We analyzed the mass increment ΔM of the BH in the integration time as a function of the orbital parameters.

We found that, within the limits of our model, the black hole cannot grow by more than 30%; this suggests that simple accretion on light-seed models are inadequate to explain high-z SMBH, and strongly encourages further studies on heavier seeds candidates and/or the occurrence of merging events.

We finally modelled the [0.5-8] keV emission from such stellar BH population, providing an estimate of its cumulative luminosity in this band. We further compute the expected emission from XRB in the same band, concluding that the one from stellar mass BH is lower than, but still comparable, with the one from XRB. Thus, the result of this study suggests that the stellar BH energy input should be included in IGM heating computations relevant to the HI 21 cm line signal from cosmic dawn. A detailed prediction of the effects of such X-ray emission on the 21 cm line power spectrum requires a future dedicated study.

Our model can be improved in many ways by including, e.g. disk formation around the BH, different (realistic) gas density distribution and effects of dynamical friction on BH's orbit, but it seems that none of them are likely to change the conclusion we have drawn in a substantial manner.

Concerning the formation of an accretion disk, we considered the rapid BH growth under anisotropic radiation feedback by Sugimura et al., 2017; it hypothesizes the BH to sprout and settle in the center of the galaxy and grow at $55\%\dot{M}_B$ leading, in our case to a BH of $122M_\odot$. Almost the same mass increment results by accounting for the presence of denser molecular clouds. Pallottini et al., 2017, performed simulations of high-z galaxies to characterize their internal structure, finding H_2 concentrated in a disk-like structure that is 0.01% of the galaxy total volume and has $n \approx 25\,\mathrm{cm}^{-3}$; this density does not lead to significant difference with our former results. In any case, even if this density would rise up to $10^5\mathrm{cm}^{-3}$ (Bolatto et al., 2008; McKee and Ostriker, 2007; Solomon et al., 1987), $\Delta M_{max} \approx 23M_\odot$. Since the nearer to the galaxy center the denser is the gas, the effect of dynamical friction on the orbit produces a slight increase of the accretion rate: we adopted the model by Tagawa et al., 2016 for the acceleration due to the dynamical friction on the BH and found out a double ΔM_{max} with respect to our naiver formulation.

To conclude, even assuming the stellar mass BHs to accrete at the Eddington limit, they could grow up to 1 (2) order of magnitude if the radiative efficiency

is 0.1 (0.01); furthermore, applying our Eddington limited accretion model to $10^4 - 10^6 M_\odot$ BHs we obtain a mass increase of at most 30% of their initial mass.

The solution to the problem of high-z quasars seems then to require high mass seeds and merging/super-Eddington accretion episodes. For what concerns merging, the results of the zoom-in cosmological hydrodynamical simulation presented by Barai et al., 2018a suggest that seeds growth is indeed dominated by direct accretion. For what concerns super-Eddington accretion, several authors have shown that it requires stringent and specific conditions, as for example slim accretion-disks (Madau et al., 2014; Volonteri et al., 2015) or seeds to be anchored in a dense, gas-rich star cluster (Alexander and Natarajan, 2014).

8 SMBHs: a merging scenario

In the previous Chapter, we discussed the feasibility of the scenario in which SMBH form by direct accretion on stellar-mass seed. In this Chapter, we analyse the scenario in which SMBH are the result of the merging of smaller progenitors: we exploit the *merger - tree* method, already described in Sec. 3.4. In particular, we reconstruct the merger history of a $z \sim 6$ quasar to make observational forecasts on its progenitors. The numerical code used to derive the merger-tree is described in Sec. 8.1. Then, in Sec. 8.2 we use the emission model of Chapter 6 to study the visibility of the progenitors in the X-ray band.

The results of this study[1] have been published in Pezzulli et al., 2017.

8.1 Data from GAMETE/QSO$_{\rm DUST}$

We use the merger-tree GAMETE/QSO$_{\rm DUST}$ (developed to study the origin of dust quasars, Valiante et al. 2011), to study a DM halo of $M_h = 10^{13} M_\odot$ at $z = 6.4$. We compare our results with the observational features of SDSS J1148+5251, powered by a SMBH of $M_\bullet \approx 3 \times 10^9 M_\odot$, detected at $z = 6.4$ Willott et al., 2003. GAMETE/QSO$_{\rm DUST}$ is made by two blocks: one reconstructs the halo merger-tree and the other uses an analytical model to derive the evolution of baryons in the halo.

The parameters in the merger-tree are (see Sec. 3.4):

- a redshift dependent resolution mass $M_{res}(z) = 10 M(T_{vir} = 10^4 K, z)$. Here, $M(T_{vir} = 10^4 \mathrm{K}, \mathrm{z})$ is the mass of a halo with virial temperature 10^4 K (Eq. (2.50)) at redshift z;
- $z_1 = 6.4$ and $z_{end} = 37$; the interval $[z_1, z_{end}]$ is divided in 5000 equally log-spaced Δz;
- $M_{seed} = 100 M_\odot$ is assigned to each newly virialized halo with a metallicity $Z < 10^{-4} Z_\odot$.

[1] Cosmological parameters are from Planck collaboration 2014.

We run 30 independent merger trees, extracting four data sets corresponding to the merger-tree snapshots at $z = 7, 8, 9, 10$. Each data set contains the accretion rate in $M_\odot$/yr and the luminosity for each BH progenitor, the hydrogen column density in cm^{-2}, the metallicity and the ratio of the dust mass to the total gas mass. Fig. 8.1 shows the positive correlation between hydrogen column density and the accretion rate for each of the active progenitors ($\dot{M}/\dot{M}_E > 10^{-3}$) at $z = 7, 8, 9, 10$. Azure and magenta points represent super and sub-Eddington accreting progenitors, respectively. It seems then, that when $N_H > 10^{23}$cm^{-2} progenitors accrete at super-Eddington rate.

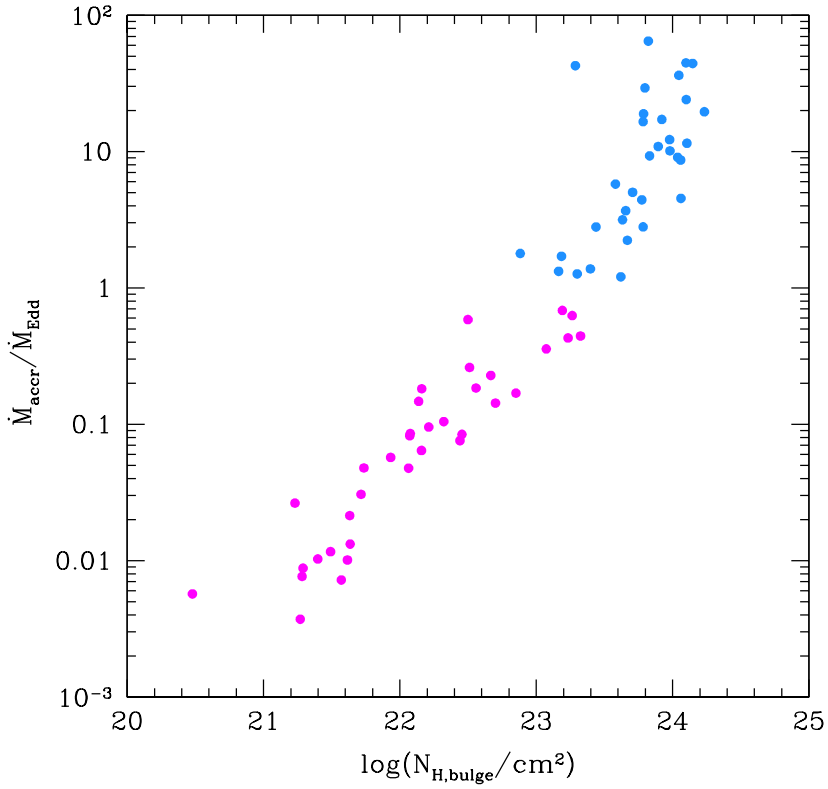

Figure 8.1: Positive correlation between hydrogen column density and the accretion rate for each of the active progenitors ($\dot{M}/\dot{M}_E > 10^{-3}$) at $z = 7, 8, 9, 10$. Azure and magenta points represent super and sub-Eddington accreting progenitors, respectively, so that when $N_H > 10^{23}$cm^{-2} progenitors accrete at super-Eddington rate.

8.2 Observational forecasts

In this Section we plan the best strategy for SMBH progenitors detection; in particular, since no progenitor have been observed so far, we focus on the occur-

rence of two impediments: that progenitors are indeed too faint to be detected by the Chandra Space Telescope or that they are too rare. In Sec. 8.2.1, we describe the Chandra X-ray Observatory and in Sec. 8.2.2 we calculate the expected number of detectable progenitors.

8.2.1 The Chandra Space Telescope

Launched in 1999, the Chandra Space Telescope is still in service. It is formed by a High Resolution Mirror Assembly (HRMA, 1.2 meters wide) with effective collection area of 400 cm^2 at 1 keV: the resulting angular resolution of 0.5 arcsec is unprecedented. Chandra includes multiple focal plane instruments. In particular, the ACIS (Advanced CCD Imaging Spectrometer) operates in an energy range $\Delta E = 0.5 - 8\mathrm{keV}$, distinguished in a soft ($\Delta E_{soft} = 0.5 - 2\mathrm{keV}$) and a hard band ($\Delta E_{hard} = 2 - 8\,\mathrm{keV}$). ACIS counts four CCD chips (1024x1024 pixels) and an image scale of 0.5 arcsec per pixel; the resulting field of view is 16.9x16.9 arcmin^2. In this Thesis, we focus on high-redshift signals and Chandra energy bands ΔE_{soft} and ΔE_{hard} in the rest frame are multiplied by $(1+z)$ (see Chapter 2). As an example, ΔE_{soft} corresponds to $[4, 16]\,\mathrm{keV}$ in the rest frame of the source at $z = 7$ and the soft Chandra energy band is then dominated by the hard component of the source spectrum.

Chandra sensitivity σ (i.e. the minimum detectable flux) can be calculated for an arbitrary exposure time t; in general two kind of noise affect observations as a function of t:

- the detector noise, that adds in each pixel a number of electrons with a time independent variance; its importance scales as the inverse of time

$$\sigma(t) \propto t^{-1}; \tag{8.1}$$

- the background noise, arising from Poisson fluctuations in the number of the background photons. The variance of the number of electrons corresponding to background noise increases with the square root of t:

$$\sigma(t) \propto t^{-1/2}. \tag{8.2}$$

The determination of the dominant noise component is not trivial. In general, it is expected that in the limit of large exposure time the background noise dominates, but the calculation of the threshold between the two regimes lies far beyond the aim of this Thesis. We adopt an empirical approach: Chandra sensitivity is

known for $t = (0.16, 0.25, 2, 4)$ Ms (Alexander et al., 2003; Elvis et al., 2009; Lehmer et al., 2005; Xue et al., 2011), Fig. 8.2; in both the hard and the soft band, these values are well-fitted by a $1/t$ law, therefore we conclude that for $t <$ 4 Ms Chandra is not background limited. In particular,

$$\sigma(t) = 10^{-16.45} \frac{1\text{Ms}}{t} \,\text{erg}\,\text{s}^{-1}\,\text{cm}^{-2} \tag{8.3}$$

for the Chandra soft band and

$$\sigma(t) = 10^{-15.73} \frac{1\text{Ms}}{t} \,\text{erg}\,\text{s}^{-1}\,\text{cm}^{-2} \tag{8.4}$$

for the Chandra hard band.

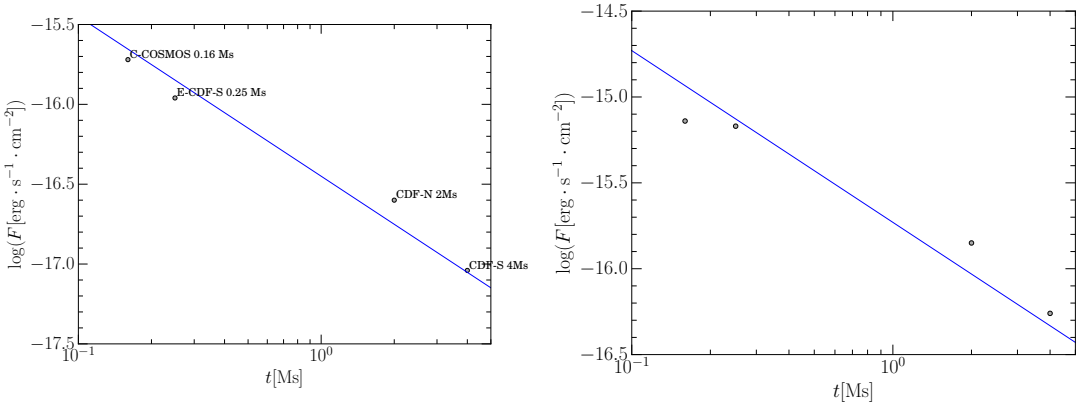

(a) Chandra soft band ([0.5, 2] keV)

(b) Chandra hard band ([2,8] keV)

Figure 8.2: Sensitivity of Chandra Space Telescope. The values of the sensitivity from Xue et al., 2011, Alexander et al., 2003, Elvis et al., 2009 and Lehmer et al., 2005 are fitted with: $\sigma(t) = 10^{-16.45} \frac{1\text{Ms}}{t} \text{erg} \cdot \text{s}^{-1} \cdot \text{cm}^{-2}$ and $\sigma(t) = 10^{-15.73} \frac{1\text{Ms}}{t} \text{erg} \cdot \text{s}^{-1} \cdot \text{cm}^{-2}$ in the Chandra soft and hard band respectively. Since the instrument has a higher sensitivity in the soft band than in the hard one, it is more advantageous to look for faint objects in this band.

Assuming that the progenitors at $z = 7$ and $z = 8$ have X-ray emission given by Eq. 6.7, we integrate the SED F_ν^{obs} in the Chandra soft band [2] $\Delta E_{soft} = [0.5, 2]$ keV. Fig. 8.3 shows the PDF of the expected flux of the supermassive black hole progenitors at redshift $z = 7, 8, 9, 10$ in the Chandra soft and hard band: the vertical lines show the minimum flux detectable by Chandra with exposure time of 4 Ms (long-dashed) and 2 Ms (short-dashed). The distribution for each snapshot (black solid lines) is divided in super- (azure) and sub- (magenta) Eddington accreting BH progenitors. We report both the *unabsorbed* (i.e. intrinsic) model (*top panel*) and the *absorbed* (i.e. accounting for photoelectric absorption) model

[2] This band corresponds to $\Delta E_{soft}^{z=7} = [4, 16]$ keV and $\Delta E_{soft}^{z=8} = [4.5, 18]$ keV for sources at $z = 7$ and $z = 8$, respectively.

(*bottom panel*), for the soft (left panels) and hard (right panels) Chandra bands. In each panel, we show the average number N of active (i.e. $\dot{M}/\dot{M}_E > 10^{-3}$) progenitors with flux larger than the 4 Ms flux limit.

According to Fig. 8.3 the most luminous progenitors are well in reach of the Chandra X-ray Observatory capability. Then the reason for non-detection must be found in their rarity.

8.2.2 Statistical analysis

The comoving volume in which the simulated progenitors are scattered is the ratio of the halo mass to the average comoving density of the Universe, $\rho_c = \frac{3H^2}{8\pi G} \approx 10^{-29}\mathrm{cm}^{-3}$. The volume[3] of one box is $V_{box} = 79\mathrm{cMpc}^3$. We assume the progenitors to lie on the two-dimensional surface $S_{box} = V^{2/3} = 18.38\mathrm{cMpc}^2$, corresponding to a square of side $L_{box} = V^{1/3} = 4.28\mathrm{cMpc}$. At redshift $z = 7$, the surface S_{box} corresponds to $\approx 1.7\,\mathrm{x}\,1.7\mathrm{arcmin}^2$, much smaller than the field of view (FOV) of Chandra $A_{Chandra} = 16.9\,\mathrm{x}\,16.9\mathrm{arcmin}^2$. Nevertheless, the Sheth and Tormen (ST) mass function (Sheth and Tormen, 1999) predicts 0.2 halos of $10^{13} M_\odot$ every Gpc^3 at $z = 6.4$ on average. Then, in volume of 5 Gpc^3 we find one simulated box on average. The volume of 5 Gpc^3 corresponds to a bidimensional surface $\approx 700 \times 700\,\mathrm{arcmin}^2$, totally explored by a survey with about 4×10^5 pointings (the FOV of Chandra is assumed); such a survey is challenging on practice, since the high number of pointings is extremely time consuming.

The number of progenitors N observed by a survey with sensitivity F that probes an area A of the sky is

$$N(F, A) = \bar{N}(F)\frac{A}{A_{ST}}, \tag{8.5}$$

where, $\bar{N}(F)$ is the number of progenitors that have a flux high enough to be detected by a telescope with sensitivity F, A is the probed area by and A_{ST} is the area corresponding to the volume in with the progenitors are scattered according to the Sheth and Tormen mass function, i.e. $(5\mathrm{Gpc}^3)^{2/3}$.

In Fig. 8.4 we show $N(F, A)$ for the *unabsorbed* (top panel) and *absorbed* (bottom panel) models, in the *observed* soft band. The sensitivity curves in the soft band of current surveys are: CDF-S in yellow, *AEGIS* in green (Laird et al., 2009), *COSMOS Legacy* in cyan (Civano et al., 2016), XMM-LSS (Gandhi et al., 2006) + XXL (Pierre et al., 2016) in magenta. In white we show the predicted curve for *ATHENA+* for a total observing time of 25 Ms (Aird et al., 2013). According to

[3] We have chosen to use comoving units, because they are redshift independent

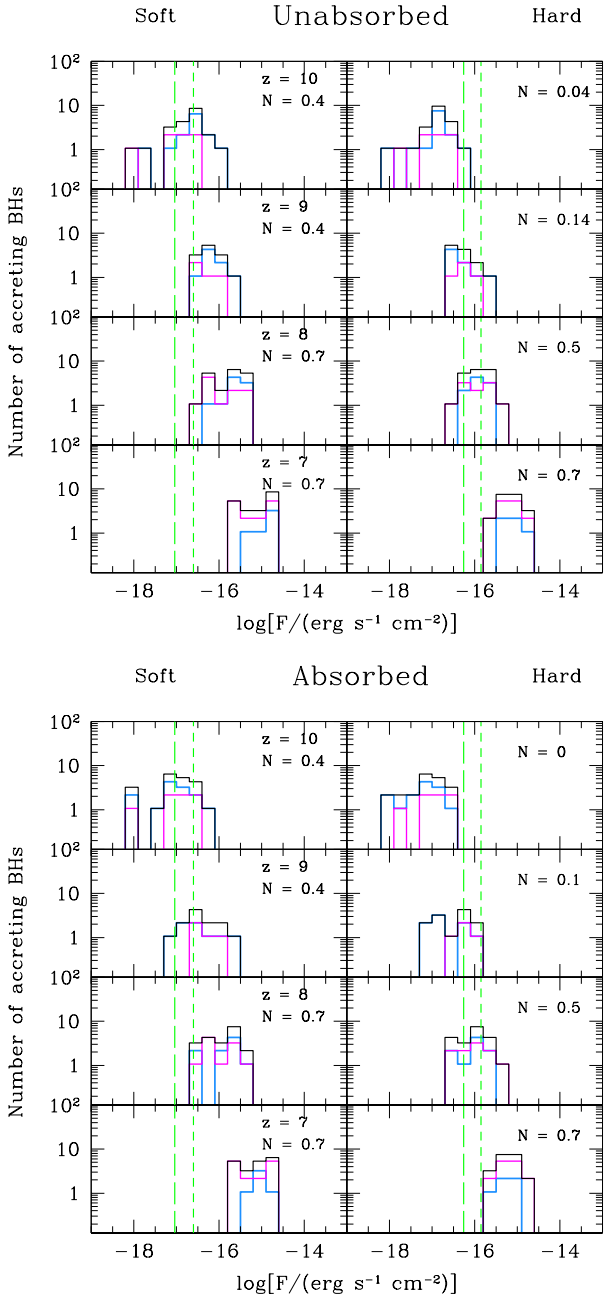

Figure 8.3: Flux distribution for each snapshot (black solid lines), divided in super- (azure) and sub- (magenta) Eddington accreting BH progenitors. We report both the *unabsorbed* model (*top panel*) and the *absorbed* model (*bottom panel*), for the soft (left panels) and hard (right panels) *Chandra* bands. Vertical dashed green lines represent different *Chandra* flux limits: exposure time of 4 Ms (long-dashed, (Xue et al., 2011)) and 2 Ms (short-dashed, (Alexander et al., 2003)) in the soft (hard) band. In each panel, it is shown the average number N of active progenitors with flux stronger than CDF 4 Ms flux limit.

this calculation, the difference between the *unabsorbed* and the *absorbed* models is almost negligible, reaching at most a factor of 2. In fact, the *observed* soft-band corresponds, for high-z progenitors, to rest-frame energies hard enough to be almost unobscured, despite the large N_{H} and Compton-thick fraction (about the 45% of the simulated progenitors). The position occupied by the curve of the most sensitive survey performed nowadays, CDF-S, exploring a solid angle of $465\,\mathrm{arcmin}^2$, is observationally disadvantaged with respect to the *COSMOS Legacy*, less sensitive but covering a wider region of the sky. This survey, in fact, should observe at least one progenitor. Similarly, XMM-LSS+XXL, despite the lower sensitivity, represents the current survey that maximizes the detection probability. Great expectations for the near future comes from *ATHENA+*: according to our estimations, for $t = 25$ Ms about 100 SMBH progenitors are expected.

In conclusion, to increase the probability to detect a SMBH ancestor it is observationally more advantageous to perform several pointings than to increase the sensitivity with a higher exposure time for a single pointing. Therefore, even if SMBHs ancestors have not been detected so far, we expect the detection to be possible in the near future.

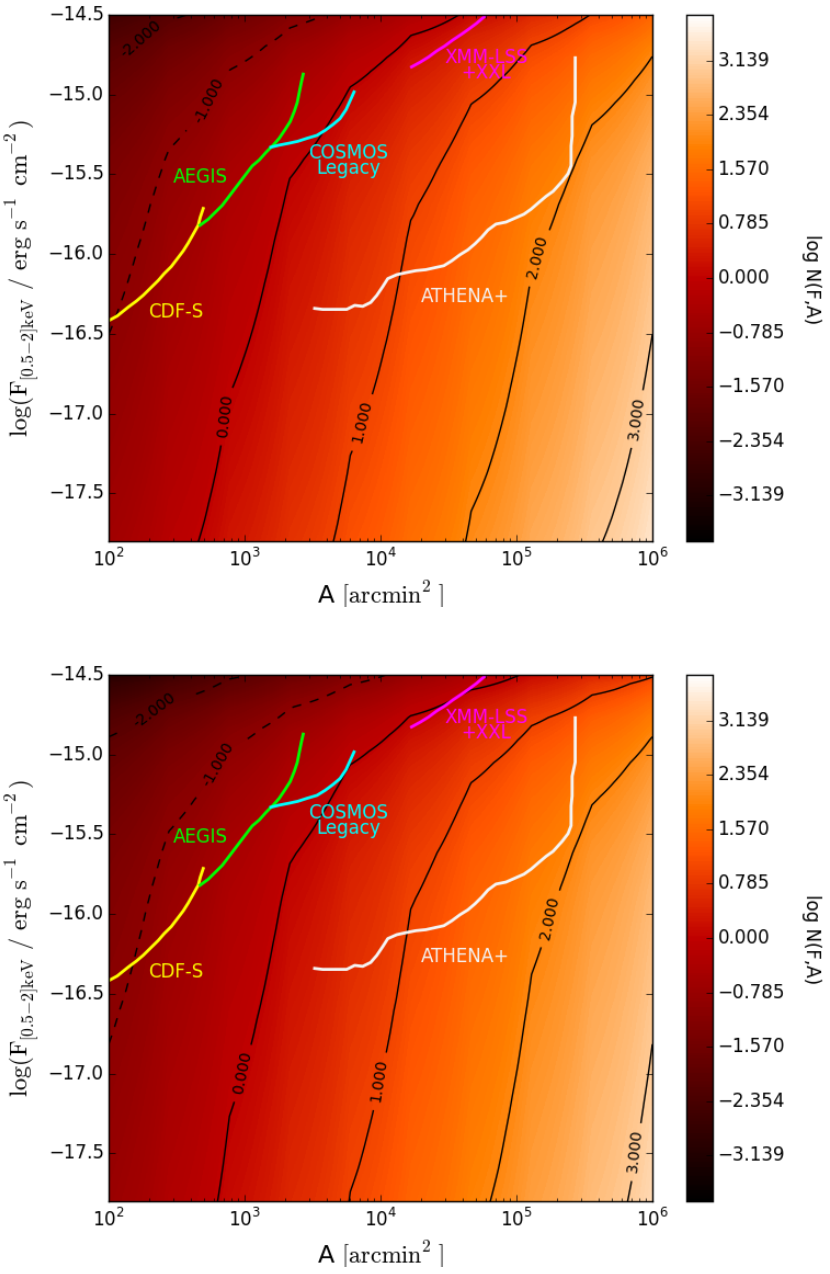

Figure 8.4: Number of progenitors potentially observable in a survey with sensitivity $F_{[0.5-2]\mathrm{keV}}$ and probing an area A for the *unabsorbed* (top panel) and *absorbed* (bottom panel) models, calculated by our collaborators at the INAF. The coloured lines represent the area/flux coverage achieved by current surveys and *ATHENA+* in their soft band and black lines represent the values of $\log N(F, A) = -2, -1$ (dashed lines) and $\log N(F, A) = 0, 1, 2$ and 3 (solid lines).

9 Massive black holes in high-redshift Lyman Break Galaxies

The presence of massive black holes (MBH, $M_\bullet \simeq 10^{7-8} M_\odot$) in typical Lyman Break Galaxies (LBGs) in the Epoch of Reionization (EoR) has become a very pressing question in early galaxy and black hole (co-)evolution. These objects might hold the key to understand at least three fundamental issues: (a) do MBHs in LBGs represent the progenitor population of supermassive black holes (SMBH, $M_\bullet \gtrsim 10^9 M_\odot$) powering the brightest quasars (QSO)? (b) what can we learn about black hole seeds and growth of these compact objects? (c) do they affect, and by what physical mechanisms, the properties and evolution of early galaxies and even large scale structure, e.g., contributing to the reionization and metal enrichment of the intergalactic medium?

At present, we have collected significant statistics and luminosity functions of a large sample of high-z galaxies over a wide span of magnitudes, thanks to space-born surveys, such as (i) the Hubble Ultra Deep Field, and the eXtreme Deep Field, exploiting the power of WFC3 onboard the Hubble Space Telescope (Bouwens et al., 2011, 2015, 2017; McLure et al., 2015; Oesch et al., 2010); (ii) the Hubble CLASH lensing surveys (Atek et al., 2015; Livermore et al., 2017; McLeod et al., 2016); (iii) X-ray surveys (Calhau et al., 2020; Suh et al., 2019). These endevours are complemented by a number of ground-based surveys (Bouwens et al., 2016; Bowler et al., 2015b; Bradley et al., 2012; Fogasy et al., 2020). Although the detected galaxies are seen within $\lesssim 1$ Gyr from the Big Bang, some of them have already built-up large stellar masses and appear as evolved systems, containing an almost solar abundance of heavy elements and dust. For recent reviews on these topics we defer the reader to Dayal and Ferrara (2018) and Maiolino and Mannucci (2019).

In lower-z galaxies there is evidence for a relation between stellar mass and the massive black holes harbored at their centers (Heckman and Best, 2014;

Kormendy and Ho, 2013; Reines and Volonteri, 2016). This connection is not yet fully established at high-z. Some cosmological hydrodynamical simulations such as Horizon-AGN (Volonteri et al., 2016) and BlueTides (Huang et al., 2018) show no significant evolution in the relation up to $z \sim 8$. The same conclusion is found analitically by Schindler et al., 2016, and more recently by Marshall et al., 2020, with a semi-analytical model that highlights minimal evolution in the black holebulge and black holetotal stellar mass relations out to $z = 8$ see also Lupi et al., 2019. Other results from hydrodynamical simulations (Barai et al., 2018b; Khandai et al., 2012) and semi-analytical models (e.g. Lamastra et al., 2010) of $z \sim 6$ SMBHs show deviations from the local relation (Kormendy and Ho, 2013). These results seem to be confirmed by a handful of high$-z$ observations (Pensabene et al., 2020; Targett et al., 2012; Wang et al., 2010; Willott et al., 2015) available to date. They show an over-massive black hole trend with respect to the host stellar mass. In particular, the analysis by Targett et al., 2012 at $z \sim 4$ shows a fast growth of the BH-to-stellar mass ratio with redshift as $\propto (1+z)^{1.4-2.0}$. However, these works are still debated and not conclusive. Specifically, Salviander et al., 2007 concluded that apparent evolution of the local law can be due to observational biases.

Observations are jeopardized by several difficulties. The standard direct X-ray detection of AGN technique, widely applied at lower redshifts, becomes very challenging for these remote and intrinsically faint (or obscured, Ni et al. 2020; Trebitsch et al. 2019a) objects. Fortunately, new results pushing instrumental capabilities to their very limits have been nevertheless obtained: using the 7 Ms Chandra survey (Cowie et al., 2020; Vito et al., 2018) have derived very stringent and useful constraints on the early MBH population. In this paper we will extensively made use of these constraints to calibrate and anchor our models. As the UV emission from MBH is likely swamped by stellar light emitted by the galaxy, observations in this band can be hardly conclusive about the presence of a central black hole in LBGs. Faint Active Galactic Nuclei (AGN) might also be present within Lyman Alpha Emitters (LAE) as recently shown by Calhau et al. (2020) (see also Haro et al. (2020)). These authors studied the X-ray and radio properties of about 4000 LAEs at $2.2 < z < 6$ from the SC4K survey in the COSMOS field. They detect 6.8% (3.2%) of these sources in the X-rays (radio). The interpretation of these results relies on the existence of a population of extremely faint/obscure AGN that escape even the deepest X-ray searches, but are potentially detectable in radio emission.

In spite of these difficulties, MBH might be caught by searching for the unique

features they imprint on the observed properties of the host galaxy. These indirect probes might then allow us to reliably answer the questions outlined at the beginning. Among other possibilities, there are at least three indirect but clear smoking guns of the presence of a hidden MBH in a LBG.

The first is the infrared emission from an accreting MBH. MBH in LBG are either quiescent or heavily obscured by dust. In this second scenario strong IR emission is expected. Both the IR peak wavelength and intensity strongly depend on the spatial distribution of dust around the BH, and therefore on the galaxy/AGN morphology[1]. The second probe are UV emission lines. UV emission lines such as HeII 1640 Å and NV 1240 Å are good tracers of a hard radiation field (Feltre et al., 2016; Laporte et al., 2017; Pallottini et al., 2015b; Stark et al., 2015; Volonteri et al., 2017a) and have been systematically used to study AGNs (Dietrich et al., 2002). Finally, MBH are in principle capable to launch powerful outflows (Barai et al., 2018b; Costa et al., 2015; Costa et al., 2014a; Ni et al., 2020). In a dust-obscured AGN, in fact, dust opacity boosts radiation pressure efficiency well above the level expected from pure electron scattering (Fabian et al., 2008). Outflows, in turn, might profoundly affect galaxy morphology, star formation, escape of ionizing photons and metal enrichment of the circumgalactic and intergalactic medium. Although at least some of these effects are degenerate with the star formation activity (Dayal et al., 2010; Pizzati et al., 2020) or PopIII emission (Pallottini et al., 2015b), their combination can uniquely pinpoint the presence of a MBH. Furthermore, signatures of outflowing gas have been recently found in several $z > 5$ galaxies (Fujimoto et al., 2019; Gallerani et al., 2018; Ginolfi et al., 2020; Sugahara et al., 2019). These outflows may be possibly powered by a yet undetected accreting MBH.

Here we use available data in combination with simple but robust semi-analytical models, similar to previous works by Petri et al., 2012b; Tanaka and Haiman, 2009; Tanaka, 2014, to study the mass and luminosity of MBH as a function of the host halo mass. With this approach we aim to assess whether LBGs at $z = 6$ host MBH, determining the MBH mass and Eddington ratio and preliminarily appraise their impact on the galaxy properties.

The Chapter is organized as follows. Sec. 9.1 describes the merger tree, seeding and growth prescriptions, along with the observational constraints we impose. In Sec. 9.2 we derive the BH-halo mass relation, and in Sec. 9.3 we use it to compute the combined galaxy-AGN luminosity function for two different scenarios. Sec.

[1] However, IR-observation of AGN in dwarf galaxies is particularly difficult as star formation in these systems is capable of heating dust in such a way that mimics the infrared colors of more luminous AGNs (Hainline et al., 2016).

9.4 contains the implications for LBGs, including FIR luminosity, emission lines, and presence of outflows. Finally, a summary is given in Sec. 9.5.

The results of this work are published in the paper Orofino et al. 2020 (submitted to MNRAS).

9.1 Method

We run merger trees by using the public code described in Parkinson et al., 2008b. Our initial goal is the derivation of the relation between the mass of the BH and the host dark matter halo. We generate merger trees with root halos of mass in the range $M_h = 10^{10.6-13} M_\odot$ at $z = 6$. Then we seed the leafs with BHs, and follow their accretion and merging down to the root. Our method is similar to the one used by Tanaka and Haiman, 2009, and is best suited to derive the most probable BH mass hosted by a halo of known mass, along with its expected variance.

We specialize our analysis to redshift $z = 6$, where existing observational data on UV and X-ray luminosity of AGN allow to put constraints on the black hole-galaxy relation. Our aim is to study the BH final mass and accretion rate at that epoch, even for those BH masses that are smaller than observed. We then require that the combined BH-galaxy luminosity functions satisfy the available constraints from deep UV/X-ray surveys, and use the results to make predictions for future early galaxies observations.

9.1.1 Merger Tree setup and parameters

Parkinson et al., 2008b algorithm follows the formation history of dark matter halos using the extended Press-Schechter theory. It has been shown to be in accurate agreement with the conditional mass functions found from ΛCDM Millennium N-body simulations. For further details on the code we refer the reader to Parkinson et al., 2008b.

We sample 40 different final halo masses equally spaced in log space from $M_{\rm min} = 10^{10.6} M_\odot$ to $M_{\rm max} = 10^{13} M_\odot$ and run $\gtrsim 100$ merger trees for each mass to achieve a significant statistics. The mass resolution of the merger trees is $M_{\rm res} = 5 \times 10^7 M_\odot$; they follow the cosmic evolution from $z = 30$ to $z = 6$. For each of the trees we computed the BH mass inside the halos, following accretion and merging history from the high-z leafs to the $z = 6$ root. The seeding and accretion prescriptions are described in the following.

Seeding

Seeding prescriptions employing stellar mass BH ($M_\bullet \lesssim 10^2 M_\odot$) seeds are known to face difficulties in explaining the observed $10^9 M_\odot$ SMBHs at $z = 6$ (Alvarez et al., 2009; Orofino et al., 2018b). Such models have to resort to prolonged super-Eddington accretion phases (Aversa et al., 2015; Lupi et al., 2016; Madau et al., 2014; Regan et al., 2019; Takeo et al., 2020; Volonteri et al., 2015) that are in contrast with models in which radiation pressure regulates gas infall, such as e.g. Park and Ricotti (2013b), Park (2012), Sugimura and Ricotti (2020), and Toyouchi et al. (2020).

We use instead a seeding prescription based on intermediate mass $M_\bullet \approx 10^5 M_\odot$ black holes (IMBH). These seeds represent the possible outcome of two direct formation scenarios: (i) monolithic collapse of the gas in H_2-free primordial halos (direct collapse BH, see, e.g. Ferrara et al. 2014b; Mayer et al. 2010; Mayer et al. 2015; Rees 1984), and (ii) heavy seeds formation in low-metallicity, dense stellar clusters where, due to energy equipartition, the most massive members tend to sink towards the center (Begelman and Rees, 1978; Boco et al., 2020; Devecchi and Volonteri, 2009; Devecchi et al., 2010, 2012; Lee, 1987; Mehrgan et al., 2019; Omukai et al., 2008; Quinlan and Shapiro, 1990; Spitzer, 1969; Vishniac, 1978). We refer to Latif and Ferrara (2016b), and Mezcua (2017) for recent reviews on this topic.

Ferrara et al., 2014b studied the IMBH initial mass function and host halo properties. They concluded that the optimal prescription is to seed halos of mass $7.5 < \log(M_h/M_\odot) < 8$ in the redshift range $8 < z < 17$ with IMBH of mass $4.75 < \log(M_\bullet/M_\odot) < 6.25$. We the adopt this prescription, but for simplicity assume a single mass [2] value $M_\bullet = 10^5 M_\odot$.

We also note that the above results represent only a necessary condition for the formation of IMBH. The prescription implicitly assumes that the halo is illuminated by a sufficiently strong UV Lyman-Werner (LW; $11.2 - 13.6$ eV) intensity $J_{LW} > J^*_{LW}$ so to prevent molecular hydrogen formation during the collapse. The precise value of the intensity threshold, $J^*_{LW} \approx (30 - 1000) \times 10^{-21} \mathrm{erg\,s^{-1}cm^{-2}Hz^{-1}sr^{-1}}$, depends on radiative transfer, chemistry and spectral shape of the sources, and it is only approximately known (Agarwal and Khochfar, 2015; Agarwal et al., 2016b; Ferrara et al., 2014b; Sugimura et al., 2014). We condense this uncertainty in the $f_{\rm seed}$ parameter expressing the fraction of potential host candidate halos that actually meet the above illumination condition,

[2] As a test, we checked that a random scatter in the seed mass range $(0.2 - 1.8) \times 10^5 M_\odot$ introduces variations $< 5\%$ in the results.

and therefore are seeded with an IMBH.

To summarize our seeding procedure: we planted a seed of $10^5 M_\odot$ in a fraction f_{seed} of the merger-tree leaves that have mass $7.5 < \log(M_h/M_\odot) < 8$ in the redshift range $8 < z < 17$; f_{seed} is constant over such mass/redshift ranges.

Growth

Implanted BH seeds can grow via two distinct channels: BH-BH merger and direct gas accretion. We assume that every halo merger results in an instantaneous BH merging. This is justified by previous calculations (Armitage and Natarajan, 2005; Colpi, 2014; Volonteri and Rees, 2006) which showed that coalescence is very rapid due to the fact that both viscous dissipation in the surrounding accretion disk, and energy loss due to gravitational wave emission have timescales much shorter than the Hubble time (≈ 1 Gyr) at $z = 6$.

For simplicity, we do not consider gravitationalradiation induced recoil (Devecchi et al., 2009; Merritt et al., 2009) neither. This assumption is partly justified by the findings of Schnittman and Buonanno (2007) indicating that the typical velocities for gravitational recoil (or kick) are of the order of $100\,\mathrm{km\,s^{-1}}$. These values are lower than the escape velocity from the typical halos we are interested in ($M_h \approx 10^{12} M_\odot$ corresponding to $v_e = 422\,\mathrm{km\,s^{-1}}$).

However, other works (e.g. Pfister et al. 2019; Tamburello et al. 2017b; Bortolas et al. 2020) deem these assumptions as too optimistic, as some BHs might be kicked off from the galaxies during the initial growth stages or because the merging time might not be negligibly short. This might lead to an overestimate of the merger efficiency, and hence of the final MBH mass. As we will see below, in the most plausible scenario growth is largely ($> 90\%$) dominated by accretion rather than by merging, so this issue only marginally affects our conclusions.

In between two merger episodes, we allow BHs to grow by direct accretion at a fraction λ_E of their Eddington rate, $\dot{M}_\bullet = \lambda_E \dot{M}_E$, where

$$\dot{M}_E \equiv \frac{L_E}{\eta c^2} = 2.5 \times 10^{-8} \left(\frac{M_\bullet}{M_\odot}\right) \left(\frac{0.1}{\eta}\right) M_\odot \mathrm{yr}^{-1}, \tag{9.1}$$

where $L_E = 1.5 \times 10^{38} (M_\bullet/M_\odot)\,\mathrm{erg\,s^{-1}}$ is the Eddington luminosity. The allowed values for the matter-radiation conversion efficiency, η, range from 0.054 for non-rotating Schwarzschild BHs to 0.42 for maximally rotating Kerr BHs (Shapiro et al., 1983). Following the arguments given in Marconi et al. (2004b) we will take $\eta = 0.1$ in the following. The Eddington-ratio λ_E is a free parameter of the model, and it is further discussed in the next Sections.

9.1.2 BH Luminosity

From the assumptions made in the previous Section it follows that the bolometric luminosity of the BH is simply given by

$$L = \lambda_E(M_\bullet) L_E. \tag{9.2}$$

In the previous equation we have highlighted the likely possibility that the Eddington ratio is a function of BH mass. This function is not yet specified in our model. In the next Section we discuss the constraints on λ_E descending from available observational data. We then explore the effects of different λ_E prescriptions.

For later use we need to calculate the X-ray ($0.5 - 2$ keV band) and UV (at 1450Å) luminosity of the black holes. These can be directly obtained from the bolometric luminosity by applying the appropriate bolometric corrections, i.e.

$$L_i = f_i(L) L, \tag{9.3}$$

with L given by Eq. 9.2, and $i = \mathrm{X}, \mathrm{UV}$. For both f_X and f_UV we use the luminosity-dependent fit by Shen et al. (2020) (see their Fig.2). For example, for $L = 10^{46} \mathrm{erg\,s^{-1}}$ they find $f_X = 0.02$ (soft band) and $f_\mathrm{UV} = 0.2$, respectively.

9.1.3 Observational constraints

In order to constrain direct accretion efficiency and obscuration (see Sec. 9.2.1 and Sec. 9.2.2) we use two types of experimental constraints available at $z \simeq 6$. The first one comes from the abundance and luminosity of SMBH. According to ΛCDM (Mo and White, 2002; Mo et al., 2010; Sheth et al., 2001) and for the adopted cosmology, the comoving density[3] of the most massive halos in our merger tree, $M_{max} = 10^{13} M_\odot$, at $z = 6$ is $n_{max} \simeq 10^{-9}\,\mathrm{Mpc^{-3}}$. According to the results of the Sloan Digital Sky Survey (Jiang et al., 2009) this abundance corresponds to a UV magnitude (at 1450Å) in the range $-27 < M_\mathrm{UV} < -25$. In this work we use $M_\mathrm{UV} \simeq -26$ or $L_\mathrm{UV} \simeq 2 \times 10^{46} \mathrm{erg\,s^{-1}}$ or $L \simeq 10^{47} \mathrm{erg\,s^{-1}}$. This sets a constrain on the product $\lambda_E M_\bullet = 6 \times 10^8 M_\odot$. As measurements of the virial SMBH mass using MgII line width of individual SDSS sources and other

[3] The precise value of n_{max} is somewhat sensitive to the cosmological parameters, particularly σ_8, and the transfer function used. As the primary goal of this work is to study MBH in LBGs, this uncertainty has virtually no impact on our results. To compute the halo mass function we have used the public code HMFcalc, available at hmf.icrar.org/hmf_finder/form/create/.

high-z quasars (Kurk et al., 2007; Mortlock et al., 2011; Willott et al., 2007b) indicate $M_\bullet \simeq (1-3)\times 10^9 M_\odot$, one can conclude that $\lambda_E \approx 0.2-0.6$ in the supermassive regime.

The second constraint comes from X-ray observations. Cowie et al., 2020 searched for high-redshift ($z > 4.5$) X-ray AGN in the deep central region of the 7 Ms Chandra Deep Field-South (CDFs) X-ray image. They put a tight[4] upper limit, $n_X = 10^{-5}\mathrm{Mpc}^{-3}$, on the comoving density of $z \simeq 6$ X-ray sources with $L_X > L_X^* = 10^{42.5}\mathrm{erg\,s}^{-1}$ in the 0.5-2 keV band. Paralleling the previous procedure, this abundance corresponds to a halo mass $M_h \simeq 10^{12} M_\odot$. Note that this halo mass scale is typical of $z = 6$ LBGs with $M_{UV} \simeq -22$ (Behroozi et al., 2019 and Fig. 9.4). CDFs observations then set a constrain $\lambda_E M_\bullet \simeq 10^6 M_\odot$ for BH hosted by LBGs at the end of the Epoch of Reionization. We should also allow for the possibility that a fraction of the emitted light by the AGN is absorbed by dust and gas in the vicinity of the black hole. When appropriate, we denote this fraction as $f_{\rm abs}$ in the appropriate X-ray or UV band.

As λ_E governs also the growth of the black hole ($d\log M_\bullet \propto \lambda_E$) we impose the above SMBH abundance/mass and X-ray luminosity limits into our merger tree by linearly interpolating λ_E in the halo mass range $10^{12-13} M_\odot$. For smaller halos we keep $\lambda_E \equiv$ const. (see Fig. 9.1); since this value is very low, $\simeq 10^{-3}$, implying a very inefficient accretion, our conclusions are weakly affected by a different assumption on the shape of λ_E for halos $M_h \lesssim 10^{12} M_\odot$. We then solve the problem by iteration. The key challenge is to produce the SMBHs powering quasars, at the same time preventing MBHs to become too luminous.

9.2 Constrained Halo-BH relation

As already mentioned, the seeding prescription we are using (see Sec. 9.1.1) represents only a necessary condition for the formation of a IMBH by direct collapse. In fact, not all the candidate host halos might be illuminated by a sufficiently strong LW flux such to prevent H_2 formation, leading to detrimental cooling fragmentation during the collapse. Given this uncertainty, we explore in the following two different scenarios, S1 and S2.

- *Maximal seeding* [Scenario S1]. This scenario assumes that all the candidates IMBH host halos are exposed to a sufficiently high LW radiation field

[4] We recall that this luminosity is so low that it could be produced purely by High Mass X-ray Binaries and hot ISM in a galaxy forming stars at a rate of $\simeq 500 M_\odot \mathrm{yr}^{-1}$ (Das et al., 2017; Mineo et al., 2014).

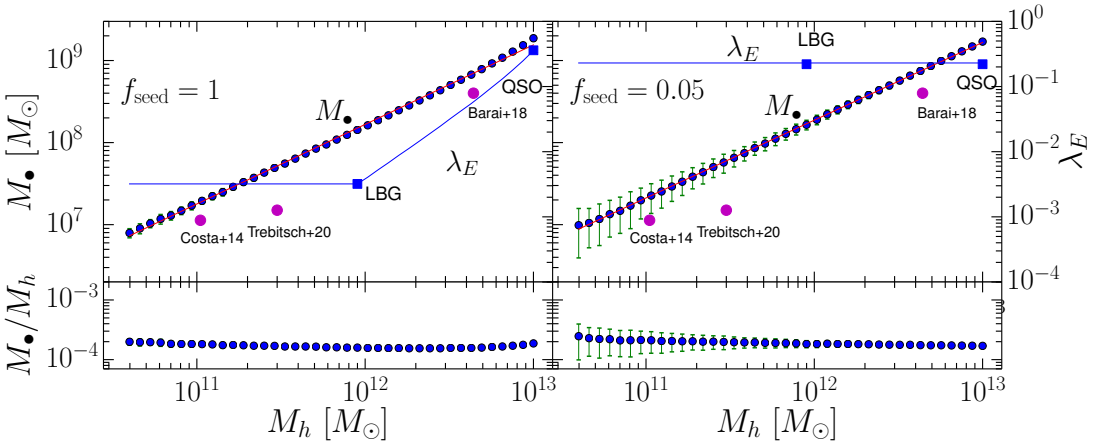

Figure 9.1: Halo vs massive black hole mass relation. *Left panel*: Results of the merger tree simulations (blue points) for scenario S1 ($f_{\rm seed} = 1$). Variance of individual points is evaluated from ≈ 100 merger tree realizations performed per halo mass bin. The red line represents the best fit (see text for an analytical expression) to the data. The Eddington ratio, λ_E, required to match CDFs and QSO abundance data is shown by the blue line. Also shown is the result of numerical simulations by Barai et al. (2018b), Costa et al. (2014b), and Trebitsch et al. (2020): the predicted trend is consistent with these works, although our BH masses are slightly larger. The bottom panel shows the $M_\bullet/M_h$ ratio across the halo mass range. *Right*: Same for S2 ($f_{\rm seed} = 0.05$).

coming either from a nearby galaxy or the cosmological background. This implies a fraction $f_{\rm seed} = 1$ of seeded halos in the leafs.

- *Inefficient seeding* [Scenario S2] This scenario envisages a inhomogeneous LW background, as predicted by some studies (Yue et al., 2014), in which only a small fraction of the putative host halos can form a IMBH. Guided by these findings, we seed a fraction $f_{\rm seed} = 0.05$ of the leafs.

As we see in the following, the main difference between the two scenarios is the relative importance of merging and accretion for the BH growth. In S1 the bulk of the final MBH mass is already made up by the seeds, and therefore limited accretion is required. In S2, instead, the initial seed mass is decreased by 20 times, and therefore growth must occur largely by accretion. We discuss the implications of these two scenarios in the following.

In this work we assume that BHs are active at all times, i.e. we do not introduce a duty cycle; however, we introduce obscuration in model S2 to satisfy the observational constraints. As obscuration and duty cycle are known to be degenerate (Chen and Gnedin, 2018; Shankar et al., 2010; Trebitsch et al., 2019b), the two possibilities can be disentangled only with the help from ancillary data such as IR observations or clustering experiments.

9.2.1 Maximal seeding scenario

In the S1 scenario $f_{\rm seed} = 1$. Our model in this case predicts a tight, almost linear relation between the MBH and halo mass (Fig. 9.1) whose best fit is $\log M_\bullet = -3.4 + 0.97 \log M_h$. Note that the variance in the relation, evaluated from the ≈ 100 merger tree realizations performed per halo mass bin, is very small.

Halos corresponding to typical LBGs at $z = 6$ ($M_h \simeq 10^{12} M_\odot$) are predicted to host BHs with mass $M_\bullet = 2 \times 10^8 M_\odot$. Such ratio, $M_\bullet / M_h \approx 2 \times 10^{-4}$, is approximately constant in the entire BH mass range, as depicted in the lower panel of Fig. 9.1; this value is significantly smaller than the seeding one, $0.001 - 0.03$.

If we convert the halo mass into stellar mass using the models by Behroozi et al. (2019) we obtain $M_\star = 1.3 \times 10^{10} M_\odot$, corresponding to a BH/stellar mass ratio $\mathcal{R} = 0.015$. While higher than the local value, $\mathcal{R} = 0.0037$ – see eq. 10 of Kormendy and Ho (2013) – yet this value is consistent with high-z determinations (Targett et al., 2012; Wang et al., 2010; Willott et al., 2015). Although at $z = 6$ the observational relation is affected by a large scatter (Pensabene et al., 2020) and observational bias, our result confirms that BHs grew faster than their host stellar counterpart.

As λ_E governs also the growth of the black hole ($d \log M_\bullet \propto \lambda_E$) we impose the SMBH abundance/mass and X-ray luminosity limits according to the deep central region of the 7 Ms CDFs X-ray image (Cowie et al. 2020, Sec. 9.1.3) into our merger tree by linearly interpolating λ_E in the halo mass range $10^{12-13} M_\odot$. For smaller halos we keep $\lambda_E \equiv$ const. (see Fig. 9.1); since this value is very low, $\simeq 10^{-3}$, implying a very inefficient accretion, our conclusions are weakly affected by a different assumption on the shape of λ_E for halos $M_h \lesssim 10^{12} M_\odot$. We then solve the problem by iteration. The key challenge is to produce the SMBHs powering quasars, at the same time preventing MBHs to become too luminous.

The CDFs luminosity limits implies that MBH in LBGs must accrete at a low Eddington ratio[5], $\lambda_E = 3 \times 10^{-3}$; such value must increase to 0.36 to reproduce the quasar constraints. These values imply a somewhat different growth mechanism for MBH and SMBH. Accreted matter represents on average only 5% of the final MBH mass at $z = 6$, the rest being acquired by merging; however, its contribution raises up to 20% for SMBH with mass $M_\bullet = 10^9 M_\odot$. In spite of such (mild) dependence on BH mass, a general conclusion is that accretion is

[5] As a test, we checked that a random scatter in the Eddington ration in the range $0 - 0.44$ introduces variations $< 5\%$ in the results.

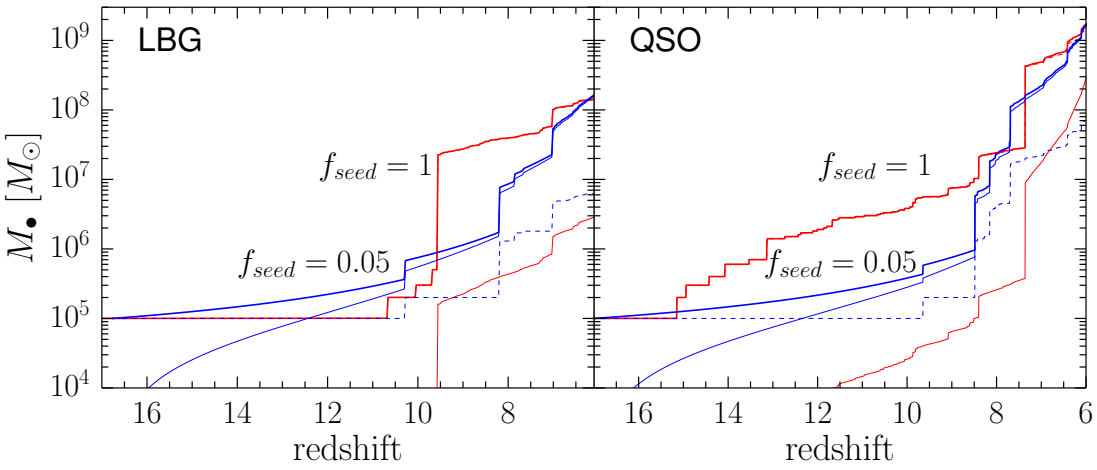

Figure 9.2: Growth history of BH hosted by Lyman Break Galaxies (left) and quasars (right) as a function of redshift. In each panel we show the total BH mass (thick lines), and the mass contributed by accretion (thin) for the two scenarios S1 ($f_{\rm seed} = 1$, red curves) and S2 ($f_{\rm seed} = 0.05$, blue). For S2 we also show the contribution by mergers (dashed blue).

a sub-dominant BH growth channel in S1 as a result of the large number of IMBH seeds available for mergers in this scenario. To gain further insight on this important aspect, we show in Fig. 9.2 with red lines the growth history of a MBH hosted by a LBG-type halo (left panel), and that for a SMBH (right). For this calculation, we followed the growth history of the seed located in the highest leaf from $z \approx 17$ down to the root. For $f_{\rm seed} = 1$ (S1) the growth is characterized by several vertical discontinuities associated with merging events, with accretion in between them playing a minor role, particularly at high redshift. Only $2.5 \times 10^6 M_\odot$, out of the final MBH mass of $1.5 \times 10^8 M_\odot$, have been accreted. For the SMBH the situation is only quantitatively different, with accretion along this branch contributing more (20%) to the growth; however, mergings are still dominating the rise of the curve.

9.2.2 Inefficient seeding scenario

In the S2 scenario $f_{\rm seed} = 0.05$. This corresponds to a likely more physical situation in which only a minor fraction of candidate halos manage to form a IMBH seed. The best fit to the MBH – halo mass relation (Fig. 9.1, right panel) is $\log M_\bullet = -3.1 + 0.95 \log M_h$, i.e., not too different from S1. The ratio $M_\bullet/M_h$ is also very similar to S1, apart from a slightly higher variance at low BH masses. To be more quantitative, the LBG BH mass is only 30% larger in S2 with respect to S1. These results are not particularly surprising as the two scenarios are bound to satisfy the same constraints.

However, the key difference is that because of the scarcer availability of seeds, the required production of SMBHs requires a higher Eddington ratio, $\lambda_E = 0.22$ in order to accrete sufficient mass. However, if we force the LBG MBH (and lower mass BH) to accrete at the Eddington ratio required by the X-ray limits, $\lambda_E = 2 \times 10^{-3}$, the early phase of the growth is strongly suppressed – also lacking a major merger contribution, and would be too slow to climb up to the SMBH range. Hence, λ_E has to be larger even in the MBH regime. For simplicity we have then assumed a constant $\lambda_E = 0.22$ in the entire BH mass range. Clearly, with this accretion rate LBG MBHs ($M_\bullet \simeq 10^{8.3} M_\odot$) would be very luminous in X-rays. From Eq. 9.3 we obtain $L_X = 1.0 \times 10^{44} \mathrm{erg\,s^{-1}}$ (for $f_X = 0.0153$, averaged over the soft and hard X-ray bands, and for the appropriate bolometric luminosity), and hence largely exceeding the CDFs upper limit $L_X^* = 3 \times 10^{42} \mathrm{erg\,s^{-1}}$.

We are forced to assume that the X-ray flux from BHs in LBGs (and to a much smaller, but not negligible extent also in quasars) must be locally absorbed by intervening gas and dust. The transmitted fraction of the X-ray luminosity, T_X, can be determined[6] by imposing that $T_X L_X = L_X^*$, or $T_X = 0.03$. The required optical depth to ≈ 1 keV photons to achieve such reduction is $\tau_X = -\ln T_X \simeq 3.53$, which for a solar metallicity gas implies an absorbing column $N_H = 1.44 \times 10^{22} \mathrm{cm^{-2}}$. We note that this conclusion perfectly agrees with LBG simulations at $z = 6$, see e.g. Fig. 2 of Behrens et al. (2019).

The differences between S2 and S1 are also evident in the growth history of BHs hosted by LBGs and QSOs. Looking again at Fig. 9.2 we see that the $f_{\rm seed} = 0.05$ curves are smoother, as a result of the more continuous growth associated with accretion[7]. Indeed, both for LBG and QSO black holes, the growth is completely (97%) dominated by accretion, with mergers playing a negligible role. This different balance between the two mechanisms entails an initial slower BH growth in S2. For example, the LBG (left panel) BH at $z \simeq 8$ is about 20× less massive than predicted in S1, for which $M_\bullet = 4 \times 10^7 M_\odot$. The same effect is visible also in the QSO BH track (right panel), albeit shifted to a higher redshift range $z = 10 - 12$. Eventually, the growth in S2 catches up with that of S1 by $z = 6$.

As the growth history encodes a memory of the initial seeding physics, it opens very interesting experimental perspectives to test when and where the first IMBH

[6] Strictly speaking, this is just a lower bound on the amount of absorption. In some cases, the central MBH might be obscured by even higher gas column densities, as found e.g. by D'Amato et al. (2020) and Vito et al. (2018) for 6 sources in the CDFs.

[7] In reality a few jumps are seen also in the the accretions curves. These correspond to the nodes of two merger tree branches, where we sum the past accreted matter in each of the two.

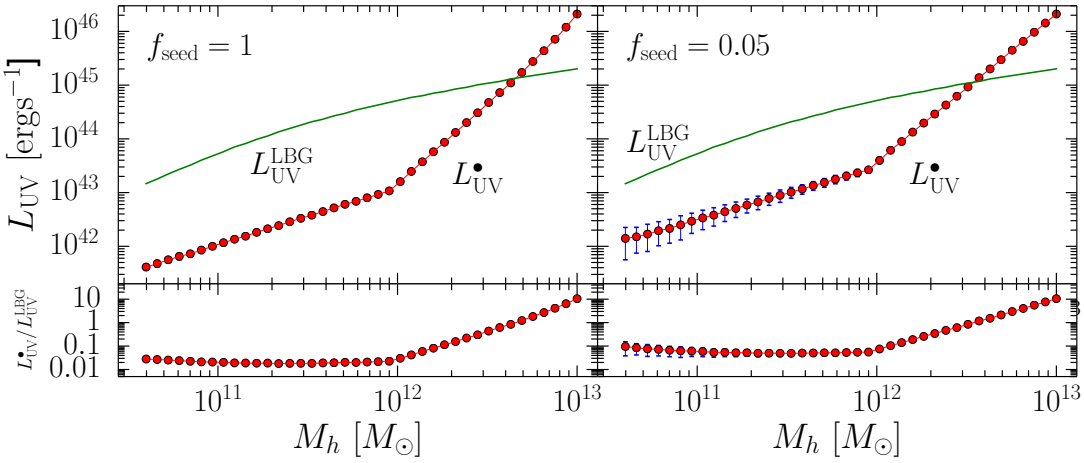

Figure 9.3: *Left panel*: LBG (green line) and BH (red points) UV luminosity vs. halo mass for S1. The bottom panel shows the luminosity ratio $L_{\rm UV}^{\bullet}/L_{\rm UV}^{\rm LBG}$ between the two components across the halo mass range. Variance of individual points is evaluated from ≈ 100 merger tree realizations performed per halo mass bin. *Right*: Same for S2 ($f_{\rm seed} = 0.05$).

appeared on the cosmic stage. Proving the existence of $M_\bullet > 10^7 M_\odot$ BH in LBGs at $z \simeq 8$, for instance, would significantly favor an efficient seeding scenario, with relevant consequences on the production of UV photons in the early universe.

9.3 Massive black holes in LBGs

Having clarified the relation between MBHs and their host halo, to enable a meaningful observational comparison it is necessary to connect the properties of MBHs to those of the Lyman Break Galaxy population. To this aim we use available galaxy UV luminosity functions (LF) to associate a UV AB magnitude at 1375Å, $M_{\rm UV}$, to each halo. We then compute the MBH UV luminosity from our model, and finally combine the two in the total UV LF.

9.3.1 Galaxy UV luminosity

Bouwens et al., 2015 have studied ≈ 10400 star forming galaxies at redshift $4 < z < 10$, and derived their UV LF. We then adopt their data at $z = 6$, and perform an abundance matching analysis to associate a $M_{\rm UV}$ to each halo mass. This entails solving the following equation:

$$\int_{M_h}^{+\infty} \frac{dn}{dM_h'} dM_h' = \int_{-\infty}^{M_{\rm UV}} \frac{dn}{dM_{\rm UV}'} dM_{\rm UV}'. \tag{9.4}$$

In the previous expression dn/dM_h is the halo mass function (Sheth et al., 2001) implemented in the numerical code developed by Murray et al., 2013; $dn/dM_{\rm UV}$ is the experimentally determined LF at $z = 6$ (Bouwens et al., 2015).

The resulting relation between halo mass and the UV luminosity of the galaxy is reported in Fig. 9.3. For reference, the typical $M_h = 10^{12} M_\odot$ LBG halo hosts a galaxy with UV luminosity of $5 \times 10^{44} {\rm erg\,s^{-1}}$. Using the standard Kennicutt (1998) conversion factor of $4.46 \times 10^9 L_\odot/M_\odot {\rm yr}^{-1}$, such luminosity corresponds to a star formation rate SFR $= 28.7\, M_\odot {\rm yr}^{-1}$.

9.3.2 BH UV luminosity

From the results obtained in Sec. 9.2 it is straightforward to compute the UV BH luminosity, using the derived $M_\bullet$ and λ_E values for the two scenarios, along with Eq. 9.3; this is displayed in Fig. 9.3. However, due to obscuration effects, the calculation for S2 requires an extra step.

We have seen that in a typical LBG, X-ray emission must be absorbed by a gas column $N_H = 1.44 \times 10^{22} {\rm cm}^{-2}$. The corresponding optical depth at 1450Å, adopting a Milky Way $R_V = 3.1$ extinction curve (Weingartner and Draine, 2001) and solar metallicity, is $\tau_{\rm UV} = \sigma_{\rm UV} N_H = 4.8 \times 10^{-22} \mathcal{A} N_H = 19.4$, where $\mathcal{A} = 2.75$ is the 1450Å-to-V band attenuation ratio (Ferrara et al., 2019). Differently from X-rays, whose opacity is dominated by gas photoelectric effects, (non-ionizing) UV photons mostly interact with dust by which they are absorbed and scattered. In spite of the large UV optical depth, scattering enables a varying fraction, $T_{\rm UV}$, of photons to escape from the system. $T_{\rm UV}$ depends on $\tau_{\rm UV}$, and on the optical properties of dust grains, namely the albedo, ω, and the Henyey-Greenstein scattering phase function, g. The classical solution (Code, 1973) for a central source surrounded by a spherical gas/dust distribution obtained with the two-stream approximation, and confirmed by Monte Carlo radiative transfer simulations[8] (Ferrara et al., 1999), is appropriate here. This yields the transmitted UV fraction

$$T_{\rm UV} = \frac{2}{(1+\zeta)e^{\xi\tau_{\rm UV}} + (1-\zeta)e^{-\xi\tau_{\rm UV}}}, \tag{9.5}$$

where

$$\zeta = \sqrt{(1-\omega)/(1-\omega g)} = 0.916, \tag{9.6}$$

and

$$\xi = \sqrt{(1-\omega)(1-\omega g)} = 0.691, \tag{9.7}$$

[8] Online digital data for the adopted configuration can be found at `www.arcetri.astro.it/~sbianchi/attenuation/E_MC.att`

having assumed the appropriate MW dust parameters $\omega = 0.3668$ and $g = 0.6719$ (Weingartner and Draine, 2001). We then find $T_{\rm UV} = 2 \times 10^{-6}$ for a MBH hosted by a LBG halo. Such value is much larger than that for a pure absorption case 5.4×10^{-9}, obtained by setting the albedo $\omega = 0$ in Eq. 9.5. However, the gas is well known to be clumpy in the circumnuclear regions of AGN. Bianchi et al. (2000) showed that this situation leads of a lower effective $\tau_{\rm UV}$. They find that for a realistic case in which 75% of the gas mass is in clumps (clumping factor $f_c = 0.75$) the effective optical depth is $\tau^*_{\rm UV} \simeq \tau_{\rm UV}/3.5 = 5.55$. Then, the corresponding (effective) transmissivity is $T^*_{\rm UV} = 0.023$; note that, by chance, $T^*_{\rm UV} \approx T_X$. As a guide we then assume this value when discussing S2 implications for LBGs in Sec. 9.4.

Similarly, $T^*_{\rm UV}$ for QSO is derived by imposing that the bolometric luminosity in our most massive halo is $10^{47}{\rm erg\,s^{-1}}$; we linearly interpolate values of $T^*_{\rm UV}$ from the QSO to the LBG halo ranges, and keep it constant below the LBG halo mass. Finally, the emerging UV luminosity, as a function of the BH mass, is

$$L^\bullet_{\rm UV} = T^*_{\rm UV} f_{\rm UV} \lambda_E L_E. \tag{9.8}$$

For the LBG, the predicted BH UV luminosity in S1 (S2) ranges from $L^\bullet_{\rm UV} = 1.5\,(3) \times 10^{43}{\rm erg\,s^{-1}}$. The BH contribution to the total (galaxy + BH) luminosity increases with halo mass (the relative ratio of the two components is displayed in the bottom panel of the Fig. 9.3).

In the LBG halo mass range $10^{11-12}\,M_\odot$, the BH luminosity is $\simeq 1/50$ of the stellar one. However, this ratio raises in more massive halos until the BH outshines the host galaxy by a factor $\simeq 3-4$ in quasars. These results are qualitatively the same for both scenarios. BHs in S2 are ~ 5 times more luminous compared to S1 in the LBG range. This is mostly due to the different value of the product $T^*_{\rm UV}\lambda_E$.

For QSOs, S1 and S2 yield the same results, because they are both anchored to the QSO abundance constraints. We recall that as in S2 λ_E is about 100× higher, the the CDFs X-ray and QSO constraints can only be satisfied if the BH emission is heavily absorbed (see Sec. 9.2.2). The previous results suggest that UV luminosity of LBG is largely dominated by stars. Although we are not dealing with ionizing photons, this finding resonates with those by Trebitsch et al. (2020) who conclude that faint AGN do not contribute significantly to cosmic reionization.

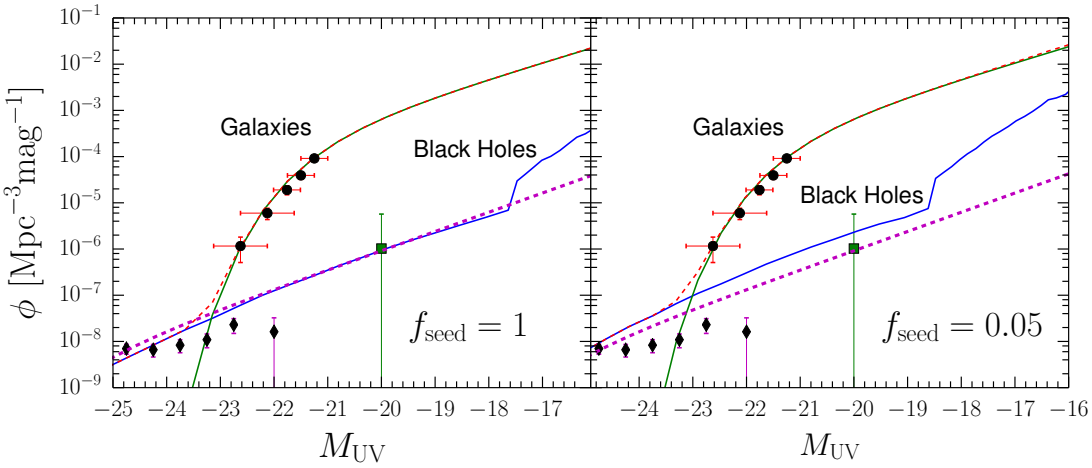

Figure 9.4: *Right*: Combined LBG and BH UV luminosity functions for scenario S1 ($f_{\rm seed} = 1$) at $z = 6$. The total (red dashed line) LF is the sum of the LBG (green) and BH (blue) contributions. Data points are from Bowler et al. (2015a) (circles), Matsuoka et al. (2018) (diamonds) and Parsa et al. (2018a) (square). The long-dashed magenta line is the QSO LF best fit from Onoue et al. (2017). *Right*: Same for S2 ($f_{\rm seed} = 0.05$).

9.3.3 UV luminosity function

We are now ready to predict the BH contribution to the observed galaxy UV LF. This can be formally written as

$$\phi \equiv \frac{dn}{dL^{\bullet}_{\rm UV}} = \frac{dn}{dM_h}\frac{dM_h}{dM_{\bullet}}\frac{dM_{\bullet}}{dL^{\bullet}_{\rm UV}}, \tag{9.9}$$

where $dM_h/dM_{\bullet}$ and $dM_{\bullet}/dL^{\bullet}_{\rm UV}$ are the BH-halo mass relation, and the BH mass dependence of the UV luminosity, respectively. Fig. 9.4 shows the results of this calculation for S1 and S2, after a final conversion of the UV luminosity into an absolute AB magnitude, $M_{\rm UV}$, at 1375Å.

In both scenarios the LF is largely dominated by stellar emission up to very bright magnitudes $M_{\rm UV} \gtrsim -23$. At luminosities fainter than this, the BH LF has a power law shape extending to $M_{\rm UV} \simeq -17.5$; at even fainter fluxes the BH LF becomes uncertain as the Eddington ratio is not constrained. The fraction of galaxies powered by a BH at $M_{\rm UV} \simeq -17.5$ is 10^{-3}; this ratio increases to 6×10^{-3} (1.0) at $M_{\rm UV} \simeq -22$ (-23.5). The very bright end of the LF is dominated by rare ($\phi < 10^{-8}$Mpc^{-3}) sources in which BH emission outshines star formation (i.e. quasars). There, the LF deviates from the Schechter function and becomes a power-law.

These results agree well with available data from large survey such as the SHELLQ (Matsuoka et al., 2018), GOLDRUSH (Ono et al., 2018), and SHELA

Stevans et al. (2018). SHELLQ, in particular, measured the quasar UV LF at $z \simeq 6$ over the wide mag range $-30 < M_{\rm UV} < -22$. The observed ratio of galaxies powered by a BH at $M_{\rm UV} \simeq -22(-23.5)$ is $1.6 \times 10^{-3}(1)$, in almost perfect agreement with our results (note that the measurement at the faintest $M_{\rm UV} < -22$ luminosity is affected by a considerable error). While the normalization of the LF at $M_{\rm UV} = -23.5$ also agrees with SHELLQ, predicting a BH density of $10^{-8}{\rm Mpc}^{-3}$, the faint-end slope[9], α, of our LF function is steeper. We find $\alpha = -2.5$, which must be compared with the SHELLQ best fit value $\alpha = -1.23^{+0.44}_{-0.34}$. We note that our faint-end slope is marginally consistent with that derived by Onoue et al. (2017), $\alpha = -2.04^{+0.33}_{-0.18}$, who included also X-ray detected AGN from Parsa et al. (2018b), and the multi-redshift determination by Manti et al. (2017), $\alpha = -1.33^{+0.88}_{-0.93}$. This discrepancy likely indicates that a considerable fraction of AGN at $z = 6$ is indeed obscured as we confirm here.

Interestingly the two seeding scenarios cannot be disentangled purely from the LF. This is because they are both bound to satisfy the observational constrains at the LBG and QSO mass scales. However, we recall that – in order to satisfy those constraints – in S2 a large fraction of the accretion luminosity must be absorbed by gas and dust. This has important implications that we discuss in the next Section.

9.4 Implications and tests

The previous analysis shows that it is very likely that LBGs host a MBH. In order to circumvent the tight limits imposed by X-ray observations, one has to assume that either such MBHs accrete at a very low rate (scenario S1), or their emission is obscured (S2). Although neither possibility can be discarded, we recall that S1 requires a, perhaps implausible, maximal efficiency of seed formation via the direct collapse mechanism. For this reason, we concentrate next on the implications of S2, and the possible ways to test them.

9.4.1 Infrared emission

We have seen that in a typical LBG, $\tau^*_{\rm UV} = 5.55$, implying that $> 99.6\%$ of the UV luminosity *produced* by the MBH, $L^\bullet_{\rm UV}[(1 - T^*_{\rm UV})/T^*_{\rm UV}] \simeq f_{\rm UV}\lambda_E L_E$, is absorbed by dust, and converted into thermal infrared emission. We recall from Sec. 9.2.2 that $\lambda_E = 0.22$, $M_\bullet = 10^{8.3} M_\odot$, and $L_E = 3 \times 10^{46}{\rm erg\,s}^{-1}$;

[9] We follow Matsuoka et al. (2018), and define the slope from the power-law fit $\log(\phi/\phi^*) = -0.4(\alpha + 1)(M_{\rm UV} - M^*_{\rm UV})$.

hence, the unobscured, intrinsic UV luminosity is $1.31 \times 10^{45} \mathrm{erg\,s^{-1}} \simeq L_{\mathrm{FIR}}$, where L_{FIR} is the total far infrared luminosity in the $8 - 1000\,\mu$m range. To proceed further, we need to estimate the dust mass from the absorbing column[10] $N_H = 1.44 \times 10^{22} \mathrm{cm^{-2}}$.

We envisage two possibilities: (a) absorption is produced by a central obscurer local to the MBH, which we can tentatively identify with the dust torus, whose size we assume to be $R_H \simeq 1$ pc (Netzer, 2015); (b) the absorbing dust is part of the interstellar medium of the host LBG. Numerical simulations (Barai et al., 2018b) indicate that $N_H \simeq 10^{22} \mathrm{cm^{-2}}$ is found at a typical distance $R_H \approx 500$ pc from the center in AGN-host galaxies[11] with a halo mass of $\approx 10^{12} M_\odot$. The dust mass (assuming a dust-to-gas ratio $\mathcal{D} = 1/162$ (Galliano et al., 2008)) is then $M_d = (2.8, 7 \times 10^5) M_\odot$ for (a) and (b), respectively.

The dust temperature, T_d is the determined by the following expression (Hirashita et al., 2014), which assumes a gray-body emission:

$$T_d = \left(\frac{f_{\mathrm{UV}} \lambda_E L_E}{\Theta M_d} \right)^{1/(4+\beta)} ; \tag{9.10}$$

where

$$\Theta = \frac{8\pi}{c^2} \frac{\kappa_{158}}{\nu_{158}^{\beta}} \frac{k_B^{4+\beta}}{h_P^{4+\beta}} \zeta(4+\beta)\Gamma(4+\beta) = 4.07 \times 10^{-6}, \tag{9.11}$$

the mass absorption coefficient, $\kappa_\nu = \kappa_{158}(\nu/\nu_{158})^\beta$ is pivoted at a the reference wavelength of 158μm since high-z ALMA observations are often tuned to the rest wavelength of [CII] emission. We take $\kappa_{158} = 20.9\,\mathrm{cm^2 g^{-1}}$, $\beta = 2$ appropriate for graphite grains following (Dayal et al., 2010) and references therein; ζ and Γ are the Zeta and Gamma functions, respectively; the other symbols have the usual meaning. We then obtain $T_d = (621, 78)$ K for (a) and (b), respectively. As expected, dust located close to the MBH gets hotter. The peak wavelength for the gray-body adopted here is $\lambda_m = 0.29/T_d$, hence yielding $\lambda_m = (4.7, 37.3)\,\mu$m. For a LBG located at $z \simeq 6$, the redshifted emission peak nicely falls in the SW/SMI bands of SPICA for case (a); for case (b) the Rayleigh-Jeans portion of the spectrum is at reach of ALMA. It is then useful to compute the expected flux in these two cases. By applying the standard formula

$$f_\nu = \frac{(1+z)}{d_L^2} \kappa_{(1+z)\nu} M_d B_{(1+z)\nu}(T_d), \tag{9.12}$$

[10] We have verified that the above predicted LBG luminosities are in perfect agreement with the observed $L_X - L_{\mathrm{FIR}}$ relation presented in Fig. 12 of Pouliasis et al. (2020).

[11] Tentatively identified with the Narrow Line Region. Such N_H corresponds to a mean gas density of $10\,\mathrm{cm^{-3}}$.

we predict a flux of $(80, 30)\mu$Jy in the SPICA SW/SMI band and for ALMA Band 6; these fluxes are well at reach of these instruments. While SPICA is still in the planning phase, available ALMA continuum observations of $z \simeq 5-6$ LBGs at 158 μm indeed report fluxes that are comparable to the above one. For example, HZ6 a LBG at $z = 5.3$ part of the Capak et al. (2015) sample with $M_{\rm UV} = -22.5$, hence comparable to the reference LBG considered here, has a measured continuum flux of $129 \pm 36\,\mu$Jy. Hence, according to our results, $> 18\%$ of the observed flux could be contributed by MBH accretion luminosity if the obscuring dust is located in the Narrow Line Region.

In summary, hot dust is expected only if a MBH is present and the dust obscurer is local ($\simeq 1$ pc) to it; if absorption occurs on larger scales (comparable to the NLR, several hundreds pc) stars and MBH accretion contribute similarly to observed continuum flux. Hence, a MBH cannot be excluded by a SPICA non-detection; an ALMA detection cannot uniquely disentangle the MBH contribution from the stellar one.

9.4.2 UV emission lines

To make progress, it is necessary to combine FIR probes with an unique feature of MBH accretion, such as UV emission lines. In particular, we should search for ionized species with an ionization potential > 4 Ryd, which cannot be produced by even the hardest (e.g. binaries) stellar radiation sources, with the possible exception of elusive Pop III stars for HeII (Pallottini et al., 2015b). The most suitable candidates are then the NV 1240Å (IP=77.47 eV) and HeII 1640Å (IP=54.4 eV) lines. Laporte et al. (2017) recently reported a $\approx 5\sigma$ detection of these two lines in the redshift[12] $z = 7.15$ galaxy COSY ($M_{\rm UV} = -21.8$, SFR=20.2 $M_\odot {\rm yr}^{-1}$), opening the interesting possibility that this system might host a central MBH powering them. The measured rest-frame equivalent widths (EWs) is $3.2^{+0.8}_{-0.7}$Å and $2.8^{+1.3}_{-0.9}$Å, for NV and HeII, respectively. COSY is undetected in the 158μm continuum (upper limit $< 14\,\mu$Jy), which, according to Eq. 9.12, should imply a AGN-heated dust with temperature $T_d \gtrsim 90$ K, and distributed within 300 pc of the MBH.

Dietrich et al. (2002) studied 744 Type 1 AGN in $0 < z < 5$, spanning nearly 6 orders of magnitude in continuum. They find that, almost independently of redshift, the EWs of most emission lines (including HeII) significantly anti-correlate with the continuum strength (akin to the Baldwin effect); the NV EW is in-

[12] We warn that our model is tuned to $z = 6$, so uncertainties of about a factor of 2 (see Fig. 9.2) in the BH mass and related quantities must be accommodated.

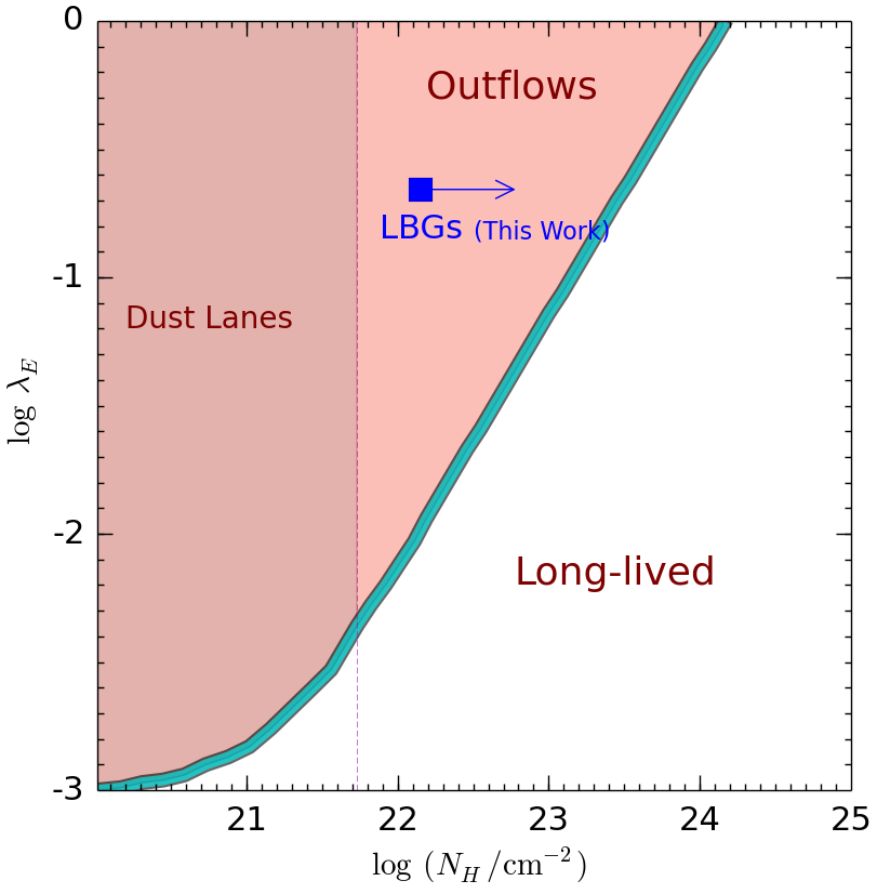

Figure 9.5: Regions in the $\lambda_E - N_H$ parameter space for a high-λ_E AGN spectrum delimiting various regimes according to Fabian et al. (2008) model. Systems lying to the left of the (maroon dashed) line develop powerful outflows if $N_H > 21.7\,\mathrm{cm}^{-2}$; below that threshold filamentary structures (dust lanes) form. The pred icted location of the typical, $M_{\mathrm{UV}} = -22$, LBG galaxy (blue point) at $z = 6$ is also shown.

stead almost independent of $L_{\rm UV}$. For our predicted *observed* luminosity of $1.31 \times 10^{45} T^*_{UV} = 3 \times 10^{43} {\rm erg\,s^{-1}}$, their relations (Fig. 7 of their paper) indicate a EW of 30Å and 20Å for Nv and Heii, respectively. Given that our MBH is significantly obscured, we need to correct these EWs for line absorption. A simple correction can be obtained by using the line escape probability, β, as a function of the medium optical depth (as both lines are in the UV, we assume the same optical depth, $\tau^*_{\rm UV} = 5.44$, derived in Sec. 9.3). Such formalism yields (see e.g. Netzer (1990) which states that the probability for a line to escape from the system is

$$\beta \simeq \frac{1}{1 + 2\tau^*_{\rm UV}} = 0.083. \tag{9.13}$$

After correcting for this effect the two EW become equal to $\simeq 2.49$Å, for Nv and $\simeq 1.66$Å, for Heii in qualitative agreement (barred the many uncertainties) with the observed values, including their relative ratio. Although this simplistic treatment cannot represent a conclusive argument, it clearly points towards the possibility that indeed COSY hosts a MBH with properties similar to those predicted here.

9.4.3 Outflows

Accreting black holes might launch powerful outflows by converting their radiative energy into kinetic one. In a dusty medium, radiation pressure does not rely purely on Thomson scattering on electrons but it can additionally transfer momentum via an efficient coupling with dust grains. The amplification (or boost) factor of the radiation force in the UV bands is $A = \sigma_{UV}/\sigma_T \approx 1900$, where σ_T is the Thomson cross-section, thus favoring the onset of radiation-pressure driven outflow from the galaxy. A proper treatment must include the frequency-weighting over the AGN spectrum. The calculation has been performed by Fabian et al. (2008) as a function of the absorbing gas column density. In their model, they show that the boost factor is the inverse of the Eddington factor, $A = \lambda_E^{-1}$.

Fig. 9.5 shows λ_E vs. N_H for a high-λ_E AGN spectrum. Systems lying in the low N_H – high λ_E region to the left of the curve develop powerful outflows, particularly if $N_H > 21.7\,{\rm cm^{-2}}$. Lower columns provide only a weak coupling to the radiation, leading only to the possible formation of filamentary structures (dust lanes). The predicted location of the typical, $M_{\rm UV} = -22$, LBG galaxy at $z = 6$ (blue point in Fig. 9.5) falls in the region in which outflows should develop. We recall that the N_H derived from the CDFs X-ray data represents a lower limit, as indicated by the arrow.

Evidences for outflows in high-z LBGs are rapidly accumulating, particularly

thanks to the availability of ALMA observations. The original claim by Gallerani et al. (2018) from a stacking analysis of the Capak et al. (2015) sample, has been now confirmed by the ALPINE Large Program (Fudamoto et al., 2020; Ginolfi et al., 2020) Fast outflows have been tentatively identified in $z = 5 - 6$ galaxies also by using deep Keck metal absorption line spectra (Sugahara et al., 2019).

Obviously, it might well be that these outflows are driven by supernova energy, rather than by an hidden AGN. Pizzati et al. (2020) showed that stellar outflows might explain the extended (size ≈ 10 kpc) C ıı halos observed around LBGs at $z = 4 - 6$ (Fujimoto et al., 2020; Fujimoto et al., 2019). Interestingly, though, these authors noted that the required relatively large outflow loading factor, $\eta = 3.2$, is only marginally consistent with starburst-driven outflows, and might instead indicate an additional energy input from a hidden AGN. Investigating the nature of outflows energy sources might lead to considerable progress in understanding the internal functioning of early galaxies, and their co-evolution with MBHs.

9.5 Summary

To address the possible presence of faint AGN powered by MBH in Lyman Break Galaxies in the Epoch of Reionization, we have run merger tree simulations implanted with direct collapse black hole seeds of mass $10^5 M_\odot$ according to the prescriptions given in Ferrara et al. (2014b). The BH growth, which can occur via BH-BH merging and matter accretion, is followed down to $z = 6$ with an accretion rate determined by the Eddington ratio, λ_E, whose values is constrained by X-ray LBG and SMBH abundance/luminosity data. Depending on the seeded halo fraction, $f_{\rm seed}$, corresponding to different feedback-regulated formation efficiencies of direct collapse BHs, we consider (a) *maximal seeding* ($f_{\rm seed} = 1$, S1), and (b) *inefficient seeding* ($f_{\rm seed} = 0.05$, S2) scenarios.

The two scenarios predict a very similar $M_\bullet/M_h \simeq 2 \times 10^{-4}$ relation at $z = 6$. This is not surprising as they are bound to satisfy the same observational constraints. However, they widely differ in many other properties. For example, in a typical LBG galaxy ($M_h = 10^{12} M_\odot, M_{\rm UV} = -22, n = 10^{-5}{\rm Mpc}^{-3}$) accreted matter represents only 5% of the final MBH mass, the rest being acquired by merging. Instead, in S2 accretion dominates in the (super-)massive BH range. It follows that, to satisfy X-ray constraints, the MBH luminosity in S2 must be obscured by an absorbing gas column density $N_H = 1.44 \times 10^{22}{\rm cm}^{-2}$, corresponding to a soft X-ray optical depth $\tau_X > 3.51$ (transmissivity $T_X = 0.03$). In addition,

S2 predicts an initial slower BH growth: proving the existence of $M_\bullet > 10^7 M_\odot$ MBH in $z \simeq 8$ LBGs, for instance, would significantly favor the maximal seeding scenario, with relevant consequences on the production of UV photons in the EoR.

We predict that the observed UV LF in both scenarios is largely dominated by stellar emission up to very bright mag, $M_{\rm UV} \gtrsim -23$, with BH emission playing a subdominant role. This finding is in agreement with the results by Volonteri et al. (2017b). The fraction of galaxies powered by a BH at $M_{\rm UV} \simeq -17.5$ is 10^{-3}; this ratio increases to 6×10^{-3} (1.0) at $M_{\rm UV} \simeq -22$ (-23.5). These results are generally consistent with available QSO LF determinations, but the predicted faint-end slope $\alpha = -2.2$ is steeper than that derived by SHELLQ (Matsuoka et al., 2018).

Although the two scenarios are both viable, S1 postulates a 100% efficiency of seed formation. As such, for the more realistic S2 scenario in which MBHs grow by obscured accretion, we have explored the following implications:

- *Infrared emission* If the obscurer is local ($\simeq 1$ pc) to the MBH, the amount of dust implied is very small, $2.8 M_\odot$; because of its high temperature, $T_d = 621$ K, dust emission peaks at restframe 4.7 μm, and a typical $z = 6$ LBG should produce a flux of 80 μJy in the SPICA SW/SMI band. If instead obscuration occurs on a scale typical of the NLR (500 pc), the larger mass ($7 \times 10^5 M_\odot$) of cooler ($T_d = 78$ K) dust produces a 30 μJy flux in ALMA Band 6. This represents $> 18\%$ of the flux observed in similar LBGs, such as HZ6.

- *Emission lines* Although ALMA FIR continuum observations alone cannot conclusively pinpoint the presence of a faint AGN in LBGs, they can be combined with UV emission lines such as NV and HeII uniquely tracing AGN hard radiation. We show that the detected EWs of these two lines in COSY, a LBG galaxy at $z = 7.15$ are successfully reproduced by our model, thus supporting the suggestion that COSY hosts an obscured MBH with properties similar to those predicted here.

- *Outflows* A MBH in a typical LBG galaxy, with the λ_E and N_H predicted here, should launch a powerful outflow according to the model by Fabian et al. (2008). This prediction is preliminarly supported by a number of recent findings, including the ALMA ALPINE survey, highlighting the presence of outflows that are only marginally consistent with starburst energetics, and might therefore require an additional energy contribution from a hidden,

faint AGN.

10 Summary and conclusions

Observations assess the presence of supermassive black holes (SMBH, $M_\bullet > 10^9 M_\odot$) even in early ($z = 6$) Universe, less than 1 Gyr after the Big Bang. Their formation in such a short time is difficult to be explained theoretically. We addressed this scientific problem analysing different formation scenarios and their observational implications.

After a brief introduction to the cosmological background and the structure formation in the early universe (Chapters 2 and 3), we started with a general description (Chapter 4) of high-z quasars and their puzzling formation (Chapter 5), developing a model for their X-ray spectrum which would take in account the attenuation of the intrinsic emission by intervening material in the interstellar medium of the host galaxy (Chapter 6). In fact, black holes are characterized by a strong X-ray emission; this could be used to discriminate them from "ordinary" stellar sources. This emission/absorption model has remarkable applications. At first, we apply this model to an already observed high-z quasar, SDSS J1148+5251, obtaining constraints on the SMBH mass and the column density of the obscuring material resulting in perfect agreement with previous independent constraints based on observations: this allowed us to test the reliability of the model (Sec.6.3).

In Chapter 7 we explored the possibility to build up a SMBH by direct accretion on a stellar mass seed wandering in a primordial galaxy: in particular, we studied the accretion rate of a $M_\bullet = 100 M_\odot$ BH in a $z = 10$ galaxy under different conditions (e.g. galaxy structure, BH initial position and velocity). We modelled the galaxy baryonic content and followed the BH trajectory and accretion history for 300 Myr, assuming the radiation-regulated accretion model of Park and Ricotti, 2013a. We analyzed the mass increment ΔM of the BH in the integration time as a function of the orbital parameters and found that, within the limits of our model, the black hole cannot increase its mass more than the 30%; this suggests that simple accretion on light-seed models are inadequate to explain high-z SMBHs and strongly encourages further studies on heavier seeds candidates and/or the occurrence of merging events. We finally provided an es-

timate of a population of these BHs' cumulative luminosity, finding it is widely negligible if compared to the predicted X-ray binaries emission in the galaxy.

Several refinements in the model can in principle affect our results, e.g. disk formation around the BH, different (realistic) density distribution and effects of dynamical friction on BH's orbit, but it seems that none of them can lead to a mass increment larger than the 30% of the initial mass. In conclusion, the solution to the problem of high-z quasars seems then to require merging or (and) high mass seeds or (and) super-Eddington accretion episodes (Madau et al., 2014, Alexander and Natarajan, 2014, Volonteri et al., 2015). Whether these conditions are achievable or not has still to be understood.

In Chapter 8 we consider the assembly of a SMBH to occur by merging of smaller progenitors (to whom we extended the model of emission/absorption developed for the quasar in Chapter 6), studying their visibility in the [0.5-2] keV band in current and future surveys. Indeed, we expect that SMBHs' ancestors are present at higher redshift but they have never been observed so far. Their detection would be an important breakthrough that would allow us to reach a deeper knowledge of these mysterious and problematic objects. Several attempts have been done in order to reveal them but, so far, without any positive responses. The difficulties in a survey planning are due to several uncertainties on the progenitors' emission as well as their abundance; nevertheless, we can rely on the results of numerical simulations to predict the expected emission and to perform some observational forecasts. The main difficulties in this kind of surveys are the need to reach a sufficient sensitivity and to explore an area of the sky large enough for the detection of these objects to be statistically probable. For this reason, we investigated the ancestors visibility the [0.5-2] keV band; we adopted the results of a semi-numerical simulation, that provides details on the progenitors accretion and on the amount of obscuring material in their environs, and evaluate the X-ray emission of the progenitors. Interestingly, we found that the most luminous SMBHs ancestors are very bright and well in reach of the most powerful current observatories. Hence, we investigated the reasons for the non-detection. By performing a statistical analysis in order to compute the volume density of these objects, we found that this negative response is due to the rarity of these sources and to the limited area probed by the latest deep surveys: therefore the non-detection is statistically expected. To examine in depth this issue, we developed a formalism to obtain, given the characteristics of the survey, how many sources are supposed to be detected. As expected for the rarity of these objects, none of the surveys performed so far probes a region of the sky large

enough for the detection to be statistically probable. We planned the best observational strategy, finding out that is more advantageous for a survey to explore an area as large as possible to the detriment of the sensitivity. The results are encouraging because none of the past surveys implemented the optimal strategy and therefore there is ample room for improvement. The conclusion of this work are very exciting: indeed, the detection of SMBHs' ancestors is already at reach of our observational capabilities. Therefore, even if they have not been detected so far, we expect the detection to be possible in the near future with the Chandra space telescope or the Athena X-ray observatory; this will be a milestone in the SMBHs observational history, leading to binding constraints in our theoretical models.

To conclude, in Chapter 9 we focussed on Lyman Break Galaxies at $z = 6$, since there are several evidence that they might host massive black holes. We addressed this question by using a merger tree combined with tight constraints from the 7 Ms Chandra survey and the known high-z SMBH population. We found that typical LBGs settled in $10^{12} M_{\odot}$, $z = 6$ halos host massive black holes of $\approx 10^{8} M_{\odot}$. Depending on the fraction, $f_{\rm seed}$, of early halos planted with a direct collapse black hole seed ($M_{\rm seed} = 10^{5} M_{\odot}$), the model suggests two possible scenarios: (a) if $f_{\rm seed} = 1$, MBH in LBGs mostly grow by merging, and must accrete at a low Eddington ratio not to exceed the experimental X-ray luminosity upper bound; (b) if $f_{\rm seed} = 0.05$ accretion dominates and MBH emission in LBGs must be heavily obscured. In both scenarios the UV luminosity function is largely dominated by stellar emission, with BH emission playing a subdominant role. Scenario (a) poses extremely challenging, and possibly unphysical, requirements on DCBH formation. Scenario (b) entails testable implications on the physical properties of LBGs involving the FIR luminosity, emission lines, and presence of outflows.

Bibliography

Agarwal, B. et al. (2016a). "Detecting direct collapse black holes: making the case for CR7". In: *MNRAS* 460, pp. 4003–4010. DOI: 10.1093/mnras/stw1173. arXiv: 1510.01733.

Agarwal, Bhaskar and Sadegh Khochfar (2015). "Revised rate coefficients for H_2 and H^- destruction by realistic stellar spectra". In: *MNRAS* 446.1, pp. 160–168. DOI: 10.1093/mnras/stu1973. arXiv: 1407.4115 [astro-ph.GA].

Agarwal, Bhaskar et al. (2016b). "New constraints on direct collapse black hole formation in the early Universe". In: *MNRAS* 459.4, pp. 4209–4217. DOI: 10.1093/mnras/stw929. arXiv: 1504.04042 [astro-ph.GA].

Aird, J. et al. (2013). "The Hot and Energetic Universe: The formation and growth of the earliest supermassive black holes". In: *ArXiv e-prints*. arXiv: 1306.2325 [astro-ph.HE].

Alexander, D. M. et al. (2003). "The Chandra Deep Field North Survey. XIII. 2 Ms Point-Source Catalogs". In: *AJ* 126, pp. 539–574. DOI: 10.1086/376473. eprint: astro-ph/0304392.

Alexander, T. and P. Natarajan (2014). "Rapid growth of seed black holes in the early universe by supra-exponential accretion". In: *Science* 345, pp. 1330–1333. DOI: 10.1126/science.1251053. arXiv: 1408.1718.

Alvarez, M. A., J. H. Wise, and T. Abel (2009). "Accretion onto the First Stellar-Mass Black Holes". In: *ApJ* 701, pp. L133–L137. DOI: 10.1088/0004-637X/701/2/L133. arXiv: 0811.0820.

Armitage, Philip J. and Priyamvada Natarajan (2005). "Eccentricity of Supermassive Black Hole Binaries Coalescing from Gas-rich Mergers". In: *ApJ* 634.2, pp. 921–927. DOI: 10.1086/497108. arXiv: astro-ph/0508493 [astro-ph].

Asplund, M. et al. (2009). "The Chemical Composition of the Sun". In: *ARA&A* 47, pp. 481–522. DOI: 10.1146/annurev.astro.46.060407.145222. arXiv: 0909.0948 [astro-ph.SR].

Atek, Hakim et al. (2015). "New Constraints on the Faint End of the UV Luminosity Function at z ~7-8 Using the Gravitational Lensing of the Hubble Frontier

Fields Cluster A2744". In: *ApJ* 800.1, 18, p. 18. DOI: 10.1088/0004-637X/800/1/18. arXiv: 1409.0512 [astro-ph.GA].

Aversa, R. et al. (2015). "Black Hole and Galaxy Coevolution from Continuity Equation and Abundance Matching". In: *ApJ* 810.1, 74, p. 74. DOI: 10.1088/0004-637X/810/1/74. arXiv: 1507.07318 [astro-ph.GA].

Bachetti, M. et al. (2013). "The Ultraluminous X-Ray Sources NGC 1313 X-1 and X-2: A Broadband Study with NuSTAR and XMM-Newton". In: *ApJ* 778, 163, p. 163. DOI: 10.1088/0004-637X/778/2/163. arXiv: 1310.0745 [astro-ph.HE].

Banerjee, R. et al. (2012). "Generation of strong magnetic fields via the small-scale dynamo during the formation of the first stars". In: *ArXiv e-prints*. arXiv: 1202.4536 [astro-ph.CO].

Baraffe, I., A. Heger, and S. E. Woosley (2001). "On the Stability of Very Massive Primordial Stars". In: *ApJ* 550, pp. 890–896. DOI: 10.1086/319808. eprint: astro-ph/0009410.

Barai, P. et al. (2018a). "Quasar outflows at z ¿ 6: the impact on the host galaxies". In: *MNRAS* 473, pp. 4003–4020. DOI: 10.1093/mnras/stx2563. arXiv: 1707.03014.

Barai, Paramita et al. (2018b). "Quasar outflows at z $\geq$ 6: the impact on the host galaxies". In: *MNRAS* 473.3, pp. 4003–4020. DOI: 10.1093/mnras/stx2563. arXiv: 1707.03014 [astro-ph.GA].

Barnes, J. and G. Efstathiou (1987). "Angular momentum from tidal torques". In: *ApJ* 319, pp. 575–600. DOI: 10.1086/165480.

Barth, A. J. et al. (2003). "Iron Emission in the z = 6.4 Quasar SDSS J114816". In: *ApJ* 594, pp. L95–L98. DOI: 10.1086/378735. eprint: astro-ph/0308005.

Begelman, M. C. and M. J. Rees (1978). "The fate of dense stellar systems". In: *MNRAS* 185, pp. 847–860. DOI: 10.1093/mnras/185.4.847.

Behrens, C. et al. (2019). "Ly α emission from galaxies in the Epoch of Reionization". In: *MNRAS* 486.2, pp. 2197–2209. DOI: 10.1093/mnras/stz980. arXiv: 1903.06185 [astro-ph.GA].

Behroozi, Peter et al. (2019). "UNIVERSEMACHINE: The correlation between galaxy growth and dark matter halo assembly from z = 0-10". In: *MNRAS* 488.3, pp. 3143–3194. DOI: 10.1093/mnras/stz1182. arXiv: 1806.07893 [astro-ph.GA].

Bernet, M. L. et al. (2008). "Strong magnetic fields in normal galaxies at high redshift". In: *Nature* 454, pp. 302–304. DOI: 10.1038/nature07105. arXiv: 0807.3347.

Berti, E., V. Cardoso, and C. M. Will (2006). "Gravitational-wave spectroscopy of massive black holes with the space interferometer LISA". In: *Phys. Rev. D* 73.6, 064030, p. 064030. DOI: 10.1103/PhysRevD.73.064030. eprint: gr-qc/0512160.

Beskin, G. M. and S. V. Karpov (2005). "Low-rate accretion onto isolated stellar-mass black holes". In: *A&A* 440, pp. 223–238. DOI: 10.1051/0004-6361:20040572. eprint: astro-ph/0403649.

Bianchi, S. et al. (2000). "Effects of clumping on the observed properties of dusty galaxies". In: *MNRAS* 311.3, pp. 601–610. DOI: 10.1046/j.1365-8711.2000.03113.x. arXiv: astro-ph/9909395 [astro-ph].

Boco, L., A. Lapi, and L. Danese (2020). "Growth of Supermassive Black Hole Seeds in ETG Star-forming Progenitors: Multiple Merging of Stellar Compact Remnants via Gaseous Dynamical Friction and Gravitational-wave Emission". In: *ApJ* 891.1, 94, p. 94. DOI: 10.3847/1538-4357/ab7446. arXiv: 2002.03645 [astro-ph.GA].

Bolatto, A. D. et al. (2008). "The Resolved Properties of Extragalactic Giant Molecular Clouds". In: *ApJ* 686, 948-965, pp. 948–965. DOI: 10.1086/591513. arXiv: 0807.0009.

Bond, J. R. et al. (1991). "Excursion set mass functions for hierarchical Gaussian fluctuations". In: *ApJ* 379, pp. 440–460. DOI: 10.1086/170520.

Bondi, H. (1952). "On spherically symmetrical accretion". In: *MNRAS* 112, p. 195. DOI: 10.1093/mnras/112.2.195.

Bondi, H. and F. Hoyle (1944). "On the mechanism of accretion by stars". In: *MNRAS* 104, p. 273. DOI: 10.1093/mnras/104.5.273.

Bortolas, Elisa et al. (2020). "Global torques and stochasticity as the drivers of massive black hole pairing in the young Universe". In: *arXiv e-prints*, arXiv:2005.02409, arXiv:2005.02409. arXiv: 2005.02409 [astro-ph.GA].

Bouwens, R. J. et al. (2011). "Ultraviolet Luminosity Functions from 132 z ~7 and z ~8 Lyman-break Galaxies in the Ultra-deep HUDF09 and Wide-area Early Release Science WFC3/IR Observations". In: *ApJ* 737.2, 90, p. 90. DOI: 10.1088/0004-637X/737/2/90. arXiv: 1006.4360 [astro-ph.CO].

Bouwens, R. J. et al. (2015). "UV Luminosity Functions at Redshifts z 4 to z 10: 10,000 Galaxies from HST Legacy Fields". In: *ApJ* 803.1, 34, p. 34. DOI: 10.1088/0004-637X/803/1/34. arXiv: 1403.4295 [astro-ph.CO].

Bouwens, R. J. et al. (2016). "The Bright End of the z 9 and z 10 UV Luminosity Functions Using All Five CANDELS Fields*". In: *ApJ* 830.2, 67, p. 67. DOI: 10.3847/0004-637X/830/2/67. arXiv: 1506.01035 [astro-ph.GA].

Bouwens, R. J. et al. (2017). "The z 6 Luminosity Function Fainter than -15 mag from the Hubble Frontier Fields: The Impact of Magnification Uncertainties". In: *ApJ* 843.2, 129, p. 129. DOI: 10.3847/1538-4357/aa70a4. arXiv: 1610.00283 [astro-ph.GA].

Bowler, R. A. A. et al. (2015a). "The galaxy luminosity function at z 6 and evidence for rapid evolution in the bright end from z 7 to 5". In: *MNRAS* 452.2, pp. 1817–1840. DOI: 10.1093/mnras/stv1403. arXiv: 1411.2976 [astro-ph.GA].

Bowler, R. A. A. et al. (2015b). "VizieR Online Data Catalog: Galaxy luminosity function at z =~7 (Bowler+, 2014)". In: *VizieR Online Data Catalog*, J/MNRAS/440/2810, J/MNRAS/440/2810.

Bowler, R. A. A. et al. (2017). "No evidence for Population III stars or a direct collapse black hole in the z=6.6 Lyman emitter CR7". In: *Monthly Notices of the Royal Astronomical Society* 469.1, pp. 448–458. DOI: 10.1093/mnras/stx839. eprint: /oup/backfile/content_public/journal/mnras/469/1/10.1093_mnras_stx839/1/stx839.pdf. URL: +http://dx.doi.org/10.1093/mnras/stx839.

Bradley, L. D. et al. (2012). "The Brightest of Reionizing Galaxies Survey: Constraints on the Bright End of the z ~8 Luminosity Function". In: *ApJ* 760.2, 108, p. 108. DOI: 10.1088/0004-637X/760/2/108. arXiv: 1204.3641 [astro-ph.CO].

Bromm, V. and A. Loeb (2003a). "Formation of the First Supermassive Black Holes". In: *ApJ* 596, pp. 34–46. DOI: 10.1086/377529. eprint: astro-ph/0212400.

— (2003b). "Formation of the First Supermassive Black Holes". In: *ApJ* 596, pp. 34–46. DOI: 10.1086/377529. eprint: astro-ph/0212400.

Bromm, V. and N. Yoshida (2011). "The First Galaxies". In: *ARA&A* 49, pp. 373–407. DOI: 10.1146/annurev-astro-081710-102608. arXiv: 1102.4638.

Calhau, João et al. (2020). "The X-ray and radio activity of typical and luminous Lyα emitters from z $\sim$ 2 to z $\sim$ 6: evidence for a diverse, evolving population". In: *MNRAS*. DOI: 10.1093/mnras/staa476. arXiv: 1909.11672 [astro-ph.GA].

Capak, P. L. et al. (2015). "Galaxies at redshifts 5 to 6 with systematically low dust content and high [C II] emission". In: *Nature* 522.7557, pp. 455–458. DOI: 10.1038/nature14500. arXiv: 1503.07596 [astro-ph.GA].

Cappelluti, N. et al. (2016). "Chandra Counterparts of CANDELS GOODS-S Sources". In: *ApJ* 823, 95, p. 95. DOI: 10.3847/0004-637X/823/2/95. arXiv: 1512.00510 [astro-ph.HE].

Carr, B. J., J. R. Bond, and W. D. Arnett (1984). "Cosmological consequences of Population III stars". In: *ApJ* 277, pp. 445–469. DOI: 10.1086/161713.

Carroll, S. M., W. H. Press, and E. L. Turner (1992). "The cosmological constant". In: *ARA&A* 30, pp. 499–542. DOI: 10.1146/annurev.aa.30.090192.002435.

Chen, Huanqing and Nickolay Y. Gnedin (2018). "Constraints on the Duty Cycles of Quasars at z $\sim$ 6". In: *The Astrophysical Journal* 868.2, p. 126. DOI: 10.3847/1538-4357/aae8e8. URL: https://doi.org/10.3847%2F1538-4357%2Faae8e8.

Chiappini, C. et al. (2011). "Imprints of fast-rotating massive stars in the Galactic Bulge". In: *Nature* 472, pp. 454–457. DOI: 10.1038/nature10000.

Chisholm, J. R., S. Dodelson, and E. W. Kolb (2003). "Stellar-Mass Black Holes in the Solar Neighborhood". In: *ApJ* 596, pp. 437–450. DOI: 10.1086/377628. eprint: astro-ph/0205138.

Ciardi, B. and A. Ferrara (2005). "The First Cosmic Structures and Their Effects". In: *Space Sci. Rev.* 116, pp. 625–705. DOI: 10.1007/s11214-005-3592-0. eprint: astro-ph/0409018.

Cicone, C. et al. (2015). "Very extended cold gas, star formation and outflows in the halo of a bright quasar at z ¿ 6". In: *A&A* 574, A14, A14. DOI: 10.1051/0004-6361/201424980. arXiv: 1409.4418.

Civano, F. et al. (2016). "The Chandra Cosmos Legacy Survey: Overview and Point Source Catalog". In: *ApJ* 819, 62, p. 62. DOI: 10.3847/0004-637X/819/1/62. arXiv: 1601.00941.

Code, A. D. (1973). "Radiative Transfer in Circumstellar Dust Clouds". In: *Interstellar Dust and Related Topics*. Ed. by Jerome Mayo Greenberg and Hendrik Christoffel van de Hulst. Vol. 52. IAU Symposium, p. 505.

Colpi, Monica (2014). "Massive Binary Black Holes in Galactic Nuclei and Their Path to Coalescence". In: *Space Sci. Rev.* 183.1-4, pp. 189–221. DOI: 10.1007/s11214-014-0067-1. arXiv: 1407.3102 [astro-ph.GA].

Conselice, C. J. (2014). "The Evolution of Galaxy Structure Over Cosmic Time". In: *ARA&A* 52, pp. 291–337. DOI: 10.1146/annurev-astro-081913-040037. arXiv: 1403.2783.

Costa, T., D. Sijacki, and M. G. Haehnelt (2015). "Fast cold gas in hot AGN outflows." In: *MNRAS* 448, pp. L30–L34. DOI: 10.1093/mnrasl/slu193. arXiv: 1411.0678 [astro-ph.GA].

Costa, Tiago, Debora Sijacki, and Martin G. Haehnelt (2014a). "Feedback from active galactic nuclei: energy- versus momentum-driving". In: *MNRAS* 444.3, pp. 2355–2376. DOI: 10.1093/mnras/stu1632. arXiv: 1406.2691 [astro-ph.GA].

Costa, Tiago et al. (2014b). "The environment of bright QSOs at z ∼ 6: star-forming galaxies and X-ray emission". In: *MNRAS* 439.2, pp. 2146–2174. DOI: 10.1093/mnras/stu101. arXiv: 1307.5854 [astro-ph.CO].

Cowie, L. L. et al. (2020). "On the Absence of High-Redshift AGNs: Little Growth in the Supermassive Black Hole Population at High Redshifts". In: *arXiv e-prints*, arXiv:2001.06015, arXiv:2001.06015. arXiv: 2001.06015 [astro-ph.GA].

D'Amato, Q. et al. (2020). *Dust and gas content of high-redshift galaxies hosting obscured AGN in the CDF-S*. arXiv: 2003.08631 [astro-ph.GA].

Das, Arpan et al. (2017). "High-mass X-ray binaries and the cosmic 21-cm signal: impact of host galaxy absorption". In: *MNRAS* 469.1, pp. 1166–1174. DOI: 10.1093/mnras/stx943. arXiv: 1702.00409 [astro-ph.CO].

Davies, M. B., M. C. Miller, and J. M. Bellovary (2011). "Supermassive Black Hole Formation Via Gas Accretion in Nuclear Stellar Clusters". In: *ApJ* 740, L42, p. L42. DOI: 10.1088/2041-8205/740/2/L42. arXiv: 1106.5943.

Davies, R. E. and J. E. Pringle (1980). "On accretion from an inhomogeneous medium". In: *MNRAS* 191, pp. 599–604. DOI: 10.1093/mnras/191.3.599.

Dayal, Pratika and Andrea Ferrara (2018). "Early galaxy formation and its large-scale effects". In: *Phys. Rep.* 780, pp. 1–64. DOI: 10.1016/j.physrep.2018.10.002. arXiv: 1809.09136 [astro-ph.GA].

Dayal, Pratika, Hiroyuki Hirashita, and Andrea Ferrara (2010). "Detecting Lyman alpha emitters in the submillimetre". In: *MNRAS* 403.2, pp. 620–624. DOI: 10.1111/j.1365-2966.2009.16164.x. arXiv: 0908.1571 [astro-ph.CO].

Devecchi, B. and M. Volonteri (2009). "Formation of the First Nuclear Clusters and Massive Black Holes at High Redshift". In: *ApJ* 694, pp. 302–313. DOI: 10.1088/0004-637X/694/1/302. arXiv: 0810.1057.

Devecchi, B. et al. (2009). "Imprints of recoiling massive black holes on the hot gas of early-type galaxies". In: *MNRAS* 394.2, pp. 633–640. DOI: 10.1111/j.1365-2966.2008.14329.x. arXiv: 0805.2609 [astro-ph].

Devecchi, B. et al. (2010). "High-redshift formation and evolution of central massive objects - I. Model description". In: *MNRAS* 409.3, pp. 1057–1067. DOI: 10.1111/j.1365-2966.2010.17363.x. arXiv: 1001.3874 [astro-ph.CO].

Devecchi, B. et al. (2012). "High-redshift formation and evolution of central massive objects - II. The census of BH seeds". In: *MNRAS* 421.2, pp. 1465–1475. DOI: 10.1111/j.1365-2966.2012.20406.x. arXiv: 1201.3761 [astro-ph.CO].

Di Matteo, T. et al. (2017). "The origin of the most massive black holes at high-z: BlueTides and the next quasar frontier". In: *MNRAS* 467, pp. 4243–4251. DOI: 10.1093/mnras/stx319. arXiv: 1606.08871.

Dietrich, M. et al. (2002). "Continuum and Emission-Line Strength Relations for a Large Active Galactic Nuclei Sample". In: *ApJ* 581.2, pp. 912–924. DOI: 10.1086/344410. arXiv: astro-ph/0208348 [astro-ph].

Dijkstra, M. et al. (2012). "Constraints on the redshift evolution of the L_X-SFR relation from the cosmic X-ray backgrounds". In: *MNRAS* 421, pp. 213–223. DOI: 10.1111/j.1365-2966.2011.20292.x. arXiv: 1108.4420.

Dijkstra, M., M. Gronke, and D. Sobral (2016). "Lyα Signatures from Direct Collapse Black Holes". In: *ApJ* 823, 74, p. 74. DOI: 10.3847/0004-637X/823/2/74. arXiv: 1602.07695.

Dopcke, G. et al. (2011). "The Effect of Dust Cooling on Low-metallicity Star-forming Clouds". In: *ApJ* 729, L3, p. L3. DOI: 10.1088/2041-8205/729/1/L3. arXiv: 1101.4891.

— (2013). "On the Initial Mass Function of Low-metallicity Stars: The Importance of Dust Cooling". In: *ApJ* 766, 103, p. 103. DOI: 10.1088/0004-637X/766/2/103. arXiv: 1203.6842 [astro-ph.SR].

Dutta, J. (2016). "On the effects of rotation in primordial star-forming clouds". In: *A&A* 585, A59, A59. DOI: 10.1051/0004-6361/201526747. arXiv: 1511.00285.

Eisenstein, D. J. and W. Hu (1998). "Baryonic Features in the Matter Transfer Function". In: *ApJ* 496, pp. 605–614. DOI: 10.1086/305424. eprint: astro-ph/9709112.

Elvis, M. et al. (2009). "The Chandra COSMOS Survey. I. Overview and Point Source Catalog". In: *ApJS* 184, pp. 158–171. DOI: 10.1088/0067-0049/184/1/158. arXiv: 0903.2062 [astro-ph.CO].

Evoli, C., A. Mesinger, and A. Ferrara (2014). "Unveiling the nature of dark matter with high redshift 21 cm line experiments". In: *J. Cosmology Astropart. Phys.* 11, 024, p. 024. DOI: 10.1088/1475-7516/2014/11/024. arXiv: 1408.1109 [astro-ph.HE].

Fabian, A. C., R. V. Vasudevan, and P. Gandhi (2008). "The effect of radiation pressure on dusty absorbing gas around active galactic nuclei". In: *MNRAS* 385.1, pp. L43–L47. DOI: 10.1111/j.1745-3933.2008.00430.x. arXiv: 0712.0277 [astro-ph].

Fan, X. et al. (2003). "A Survey of z¿5.7 Quasars in the Sloan Digital Sky Survey. II. Discovery of Three Additional Quasars at z¿6". In: *AJ* 125, pp. 1649–1659. DOI: 10.1086/368246. eprint: astro-ph/0301135.

Fan, X. et al. (2006). "A Survey of z ¡5.7 Quasars in the Sloan Digital Sky Survey. IV. Discovery of Seven Additional Quasars". In: *AJ* 131, pp. 1203–1209. DOI: 10.1086/500296. eprint: astro-ph/0512080.

Federrath, C. et al. (2011). "A New Jeans Resolution Criterion for (M)HD Simulations of Self-gravitating Gas: Application to Magnetic Field Amplification by Gravity-driven Turbulence". In: *ApJ* 731, 62, p. 62. DOI: 10.1088/0004-637X/731/1/62. arXiv: 1102.0266 [astro-ph.SR].

Feltre, A., S. Charlot, and J. Gutkin (2016). "Nuclear activity versus star formation: emission-line diagnostics at ultraviolet and optical wavelengths". In: *MNRAS* 456.3, pp. 3354–3374. DOI: 10.1093/mnras/stv2794. arXiv: 1511.08217 [astro-ph.GA].

Ferrara, A., M. Pettini, and Y. Shchekinov (2000). "Mixing metals in the early Universe". In: *MNRAS* 319, pp. 539–548. DOI: 10.1046/j.1365-8711.2000.03857.x. eprint: astro-ph/0004349.

Ferrara, A. et al. (2014a). "Initial mass function of intermediate-mass black hole seeds". In: *MNRAS* 443, pp. 2410–2425. DOI: 10.1093/mnras/stu1280. arXiv: 1406.6685.

— (2014b). "Initial mass function of intermediate-mass black hole seeds". In: *MNRAS* 443.3, pp. 2410–2425. DOI: 10.1093/mnras/stu1280. arXiv: 1406.6685 [astro-ph.GA].

Ferrara, A. et al. (2019). "A physical model for [C II] line emission from galaxies". In: *MNRAS* 489.1, pp. 1–12. DOI: 10.1093/mnras/stz2031. arXiv: 1908.07536 [astro-ph.GA].

Ferrara, Andrea et al. (1999). "An Atlas of Monte Carlo Models of Dust Extinction in Galaxies for Cosmological Applications". In: *ApJS* 123.2, pp. 437–445. DOI: 10.1086/313244. arXiv: astro-ph/9903078 [astro-ph].

Fiacconi, D. et al. (2013). "Massive Black Hole Pairs in Clumpy, Self-gravitating Circumnuclear Disks: Stochastic Orbital Decay". In: *ApJ* 777, L14, p. L14. DOI: 10.1088/2041-8205/777/1/L14. arXiv: 1307.0822.

Fiore, F. et al. (2012). "Faint high-redshift AGN in the Chandra deep field south: the evolution of the AGN luminosity function and black hole demography". In: *A&A* 537, A16, A16. DOI: 10.1051/0004-6361/201117581. arXiv: 1109.2888.

Fireman, E. L. (1974). "Interstellar Absorption of X-Rays". In: *ApJ* 187, pp. 57–60. DOI: 10.1086/152588.

Fogasy, Judit et al. (2020). "SMM J04135+10277: A distant QSO-starburst system caught by ALMA". In: *MNRAS*. DOI: 10.1093/mnras/staa472. arXiv: 2002.06925 [astro-ph.GA].

Frank, J., A. King, and D. Raine (2002). *Accretion Power in Astrophysics*. Cambridge University Press. ISBN: 9780521629577. URL: https://books.google.it/books?id=GGM_t-xn8ocC.

Fudamoto, Yoshinobu et al. (2020). "The ALPINE-ALMA [CII] Survey: Dust Attenuation Properties and Obscured Star-Formation at z~4.4-5.8". In: *arXiv e-prints*, arXiv:2004.10760, arXiv:2004.10760. arXiv: 2004.10760 [astro-ph.GA].

Fujimoto, S. et al. (2020). "The ALPINE-ALMA [CII] Survey: Size of Individual Star-Forming Galaxies at z=4-6 and their Extended Halo Structure". In: *arXiv e-prints*, arXiv:2003.00013, arXiv:2003.00013. arXiv: 2003.00013 [astro-ph.GA].

Fujimoto, Seiji et al. (2019). "First Identification of 10 kpc [C II]158 μm Halos around Star-forming Galaxies at z=57". In: *ApJ* 887.2, 107, p. 107. DOI: 10.3847/1538-4357/ab480f. arXiv: 1902.06760 [astro-ph.GA].

Furlanetto, S. R. and S. J. Stoever (2010). "Secondary ionization and heating by fast electrons". In: *MNRAS* 404, pp. 1869–1878. DOI: 10.1111/j.1365-2966.2010.16401.x. arXiv: 0910.4410.

Gallerani, S. et al. (2008). "Glimpsing through the high-redshift neutral hydrogen fog". In: *MNRAS* 386, pp. 359–369. DOI: 10.1111/j.1365-2966.2008.13029.x. arXiv: 0706.1053.

Gallerani, S. et al. (2010). "The extinction law at high redshift and its implications". In: *A&A* 523, A85, A85. DOI: 10.1051/0004-6361/201014721. arXiv: 1006.4463.

Gallerani, S. et al. (2014). "First CO(17-16) emission line detected in a z ¿ 6 quasar". In: *MNRAS* 445, pp. 2848–2853. DOI: 10.1093/mnras/stu2031. arXiv: 1409.4413.

Gallerani, S. et al. (2017). "X-ray spectroscopy of the z = 6.4 quasar SDSS J1148+5251". In: *MNRAS* 467, pp. 3590–3597. DOI: 10.1093/mnras/stx363. arXiv: 1702.07349.

Gallerani, S. et al. (2018). "ALMA suggests outflows in z ∼ 5.5 galaxies". In: *MNRAS* 473.2, pp. 1909–1917. DOI: 10.1093/mnras/stx2458. arXiv: 1604.05714 [astro-ph.GA].

Galliano, Frédéric, Eli Dwek, and Pierre Chanial (2008). "Stellar Evolutionary Effects on the Abundances of Polycyclic Aromatic Hydrocarbons and Supernova-Condensed Dust in Galaxies". In: *ApJ* 672.1, pp. 214–243. DOI: 10.1086/523621. arXiv: 0708.0790 [astro-ph].

Gandhi, P. et al. (2006). "The XMM large scale structure survey: properties and two-point angular correlations of point-like sources". In: *A&A* 457, pp. 393–404. DOI: 10.1051/0004-6361:20065284. eprint: astro-ph/0607135.

Georgakakis, A. et al. (2015). "The X-ray luminosity function of active galactic nuclei in the redshift interval z=3-5". In: *MNRAS* 453, pp. 1946–1964. DOI: 10.1093/mnras/stv1703. arXiv: 1507.07558 [astro-ph.HE].

Giallongo, E. et al. (2015). "Faint AGNs at z ¿ 4 in the CANDELS GOODS-S field: looking for contributors to the reionization of the Universe". In: *A&A* 578, A83, A83. DOI: 10.1051/0004-6361/201425334. arXiv: 1502.02562.

Ginolfi, M. et al. (2020). "The ALPINE-ALMA [C II] survey: Star-formation-driven outflows and circumgalactic enrichment in the early Universe". In: *A&A* 633, A90, A90. DOI: 10.1051/0004-6361/201936872. arXiv: 1910.04770 [astro-ph.GA].

Greif, T. H. et al. (2011). "Simulations on a Moving Mesh: The Clustered Formation of Population III Protostars". In: *ApJ* 737, 75, p. 75. DOI: 10.1088/0004-637X/737/2/75. arXiv: 1101.5491.

Haiman, Z. (2013). "The Formation of the First Massive Black Holes". In: *The First Galaxies*. Ed. by T. Wiklind, B. Mobasher, and V. Bromm. Vol. 396.

Astrophysics and Space Science Library, p. 293. DOI: 10.1007/978-3-642-32362-1_6. arXiv: 1203.6075.

Hainline, Kevin N. et al. (2016). "Mid-infrared Colors of Dwarf Galaxies: Young Starbursts Mimicking Active Galactic Nuclei". In: *ApJ* 832.2, 119, p. 119. DOI: 10.3847/0004-637X/832/2/119. arXiv: 1609.06721 [astro-ph.GA].

Häring, N. and H.-W. Rix (2004). "On the Black Hole Mass-Bulge Mass Relation". In: *ApJ* 604, pp. L89–L92. DOI: 10.1086/383567. eprint: astro-ph/0402376.

Haro, P. Arrabal et al. (2020). *Differences and similarities of stellar populations in LAEs and LBGs at $z \sim 3.4$ - 6.8*. arXiv: 2004.11175 [astro-ph.GA].

Hartwig, T. et al. (2016). "Exploring the nature of the Lyman-α emitter CR7". In: *MNRAS* 462, pp. 2184–2202. DOI: 10.1093/mnras/stw1775. arXiv: 1512.01111.

Heckman, Timothy M. and Philip N. Best (2014). "The Coevolution of Galaxies and Supermassive Black Holes: Insights from Surveys of the Contemporary Universe". In: *ARA&A* 52, pp. 589–660. DOI: 10.1146/annurev-astro-081913-035722. arXiv: 1403.4620 [astro-ph.GA].

Heger, A., N. Langer, and S. E. Woosley (2000). "Presupernova Evolution of Rotating Massive Stars. I. Numerical Method and Evolution of the Internal Stellar Structure". In: *ApJ* 528, pp. 368–396. DOI: 10.1086/308158. eprint: astro-ph/9904132.

Heger, A. et al. (2002). "Evolution and Explosion of Very Massive Primordial Stars". In: *Lighthouses of the Universe: The Most Luminous Celestial Objects and Their Use for Cosmology*. Ed. by M. Gilfanov, R. Sunyeav, and E. Churazov, p. 369. DOI: 10.1007/10856495_57. eprint: astro-ph/0112059.

Heger, A. et al. (2003). "How Massive Single Stars End Their Life". In: *ApJ* 591, pp. 288–300. DOI: 10.1086/375341. eprint: astro-ph/0212469.

Hirano, S. et al. (2014). "One Hundred First Stars: Protostellar Evolution and the Final Masses". In: *ApJ* 781, 60, p. 60. DOI: 10.1088/0004-637X/781/2/60. arXiv: 1308.4456 [astro-ph.CO].

Hirashita, Hiroyuki et al. (2014). "Constraining dust formation in high-redshift young galaxies". In: *MNRAS* 443.2, pp. 1704–1712. DOI: 10.1093/mnras/stu1290. arXiv: 1406.6762 [astro-ph.GA].

Hopkins, P. F., G. T. Richards, and L. Hernquist (2007). "An Observational Determination of the Bolometric Quasar Luminosity Function". In: *ApJ* 654, pp. 731–753. DOI: 10.1086/509629. eprint: astro-ph/0605678.

Hoyle, F. and R. A. Lyttleton (1939). "The effect of interstellar matter on climatic variation". In: *Proceedings of the Cambridge Philosophical Society* 35, p. 405. DOI: 10.1017/S0305004100021150.

Huang, Kuan-Wei et al. (2018). "BlueTides simulation: establishing black hole-galaxy relations at high redshift". In: *Monthly Notices of the Royal Astronomical Society* 478.4, pp. 5063–5073. ISSN: 0035-8711. DOI: 10.1093/mnras/sty1329. eprint: https://academic.oup.com/mnras/article-pdf/478/4/5063/25105638/sty1329.pdf. URL: https://doi.org/10.1093/mnras/sty1329.

Jiang, L. et al. (2015). "Discovery of Eight z = 6 Quasars in the Sloan Digital Sky Survey Overlap Regions". In: *AJ* 149, 188, p. 188. DOI: 10.1088/0004-6256/149/6/188. arXiv: 1504.01741.

Jiang, Linhua et al. (2009). "A Survey of z ~6 Quasars in the Sloan Digital Sky Survey Deep Stripe. II. Discovery of Six Quasars at z $_{AB}$>21". In: *AJ* 138.1, pp. 305–311. DOI: 10.1088/0004-6256/138/1/305. arXiv: 0905.4126 [astro-ph.CO].

Johnson, J. L. and V. Bromm (2007). "The aftermath of the first stars: massive black holes". In: *MNRAS* 374, pp. 1557–1568. DOI: 10.1111/j.1365-2966.2006.11275.x. eprint: astro-ph/0605691.

Juarez, Y. et al. (2009). "The metallicity of the most distant quasars". In: *A&A* 494.2, pp. L25–L28. DOI: 10.1051/0004-6361:200811415. arXiv: 0901.0974 [astro-ph.CO].

Kennicutt Robert C., Jr. (1998). "Star Formation in Galaxies Along the Hubble Sequence". In: *ARA&A* 36, pp. 189–232. DOI: 10.1146/annurev.astro.36.1.189. arXiv: astro-ph/9807187 [astro-ph].

Khandai, Nishikanta et al. (2012). "The formation of galaxies hosting z ∼ 6 quasars". In: *MNRAS* 423.3, pp. 2397–2406. DOI: 10.1111/j.1365-2966.2012.21047.x. arXiv: 1111.0692 [astro-ph.CO].

Kormendy, John and Luis C. Ho (2013). "Coevolution (Or Not) of Supermassive Black Holes and Host Galaxies". In: *ARA&A* 51.1, pp. 511–653. DOI: 10.1146/annurev-astro-082708-101811. arXiv: 1304.7762 [astro-ph.CO].

Kudritzki, R.-P. and J. Puls (2000). "Winds from Hot Stars". In: *ARA&A* 38, pp. 613–666. DOI: 10.1146/annurev.astro.38.1.613.

Kurk, Jaron D. et al. (2007). "Black Hole Masses and Enrichment of z ~6 SDSS Quasars". In: *ApJ* 669.1, pp. 32–44. DOI: 10.1086/521596. arXiv: 0707.1662 [astro-ph].

Lacey, C. and S. Cole (1993). "Merger rates in hierarchical models of galaxy formation". In: *MNRAS* 262, pp. 627–649.

Laird, E. S. et al. (2009). "AEGIS-X: the Chandra Deep Survey of the Extended Groth Strip". In: *ApJS* 180, pp. 102–116. DOI: 10.1088/0067-0049/180/1/102. arXiv: 0809.1349.

Lamastra, A. et al. (2010). "The building up of the black hole-stellar mass relation". In: *MNRAS* 405.1, pp. 29–40. DOI: 10.1111/j.1365-2966.2010.16439.x. arXiv: 1001.5407 [astro-ph.CO].

Laporte, Nicolas et al. (2017). "A Spectroscopic Search for AGN Activity in the Reionization Era". In: *ApJ* 851.1, 40, p. 40. DOI: 10.3847/1538-4357/aa96a8. arXiv: 1708.05173 [astro-ph.GA].

Latif, M. A. and A. Ferrara (2016a). "Formation of Supermassive Black Hole Seeds". In: *PASA* 33, e051, e051. DOI: 10.1017/pasa.2016.41. arXiv: 1605.07391.

— (2016b). "Formation of Supermassive Black Hole Seeds". In: *PASA* 33, e051, e051. DOI: 10.1017/pasa.2016.41. arXiv: 1605.07391.

Lee, H. M. (1987). "Dynamical effects of successive mergers on the evolution of spherical stellar systems". In: *ApJ* 319, pp. 801–818. DOI: 10.1086/165498.

Lehmer, B. D. et al. (2005). "The Extended Chandra Deep Field-South Survey: Chandra Point-Source Catalogs". In: *ApJS* 161, pp. 21–40. DOI: 10.1086/444590. eprint: astro-ph/0506607.

Lehmer, B. D. et al. (2016). "The Evolution of Normal Galaxy X-Ray Emission through Cosmic History: Constraints from the 6 MS Chandra Deep Field-South". In: *ApJ* 825, 7, p. 7. DOI: 10.3847/0004-637X/825/1/7. arXiv: 1604.06461.

Livermore, R. C., S. L. Finkelstein, and J. M. Lotz (2017). "VizieR Online Data Catalog: Galaxies >~6 from the Hubble Frontier Fields (Livermore+, 2017)". In: *VizieR Online Data Catalog*, J/ApJ/835/113, J/ApJ/835/113.

Lupi, A. et al. (2014). "Constraining the high-redshift formation of black hole seeds in nuclear star clusters with gas inflows". In: *MNRAS* 442, pp. 3616–3626. DOI: 10.1093/mnras/stu1120. arXiv: 1406.2325.

Lupi, A. et al. (2016). "Growing massive black holes through supercritical accretion of stellar-mass seeds". In: *MNRAS* 456, pp. 2993–3003. DOI: 10.1093/mnras/stv2877. arXiv: 1512.02651.

Lupi, Alessandro et al. (2019). "High-redshift quasars and their host galaxies - I. Kinematical and dynamical properties and their tracers". In: *MNRAS* 488.3,

pp. 4004–4022. DOI: 10.1093/mnras/stz1959. arXiv: 1901.02464 [astro-ph.GA].

Lusso, E. et al. (2012). "Bolometric luminosities and Eddington ratios of X-ray selected active galactic nuclei in the XMM-COSMOS survey". In: *MNRAS* 425, pp. 623–640. DOI: 10.1111/j.1365-2966.2012.21513.x. arXiv: 1206.2642.

Macciò, A. V. et al. (2007). "Concentration, spin and shape of dark matter haloes: scatter and the dependence on mass and environment". In: *MNRAS* 378, pp. 55–71. DOI: 10.1111/j.1365-2966.2007.11720.x. eprint: astro-ph/0608157.

Madau, P., F. Haardt, and M. Dotti (2014). "Super-critical Growth of Massive Black Holes from Stellar-mass Seeds". In: *ApJ* 784, L38, p. L38. DOI: 10.1088/2041-8205/784/2/L38. arXiv: 1402.6995.

Magorrian, J. et al. (1998). "The Demography of Massive Dark Objects in Galaxy Centers". In: *AJ* 115, pp. 2285–2305. DOI: 10.1086/300353. eprint: astro-ph/9708072.

Maiolino, R. and F. Mannucci (2019). "De re metallica: the cosmic chemical evolution of galaxies". In: *A&A Rev.* 27.1, 3, p. 3. DOI: 10.1007/s00159-018-0112-2. arXiv: 1811.09642 [astro-ph.GA].

Maiolino, R. et al. (2012). "Evidence of strong quasar feedback in the early Universe". In: *MNRAS* 425, pp. L66–L70. DOI: 10.1111/j.1745-3933.2012.01303.x. arXiv: 1204.2904.

Makino, N., S. Sasaki, and Y. Suto (1998). "X-Ray Gas Density Profile of Clusters of Galaxies from the Universal Dark Matter Halo". In: *ApJ* 497, pp. 555–558. DOI: 10.1086/305507. eprint: astro-ph/9710344.

Manti, S. et al. (2017). "Quasar UV luminosity function evolution up to z = 8". In: *MNRAS* 466.1, pp. 1160–1169. DOI: 10.1093/mnras/stw3168. arXiv: 1612.01544 [astro-ph.GA].

Mao, S., H. J. Mo, and S. D. M. White (1998). "The evolution of galactic discs". In: *MNRAS* 297, pp. L71–L75. DOI: 10.1046/j.1365-8711.1998.01766.x.

Marconi, A. et al. (2004a). "Local supermassive black holes, relics of active galactic nuclei and the X-ray background". In: *MNRAS* 351, pp. 169–185. DOI: 10.1111/j.1365-2966.2004.07765.x eprint: astro-ph/0311619.

— (2004b). "Local supermassive black holes, relics of active galactic nuclei and the X-ray background". In: *MNRAS* 351.1, pp. 169–185. DOI: 10.1111/j.1365-2966.2004.07765.x. arXiv: astro-ph/0311619 [astro-ph].

Marshall, Madeline A. et al. (2020). "Dark-ages reionization and galaxy formation simulation - XVIII. The high-redshift evolution of black holes and their host galaxies". In: *MNRAS* 494.2, pp. 2747–2759. DOI: 10.1093/mnras/staa936. arXiv: 1910.08124 [astro-ph.GA].

Matsuoka, Yoshiki et al. (2018). "Subaru High-z Exploration of Low-luminosity Quasars (SHELLQs). V. Quasar Luminosity Function and Contribution to Cosmic Reionization at z = 6". In: *ApJ* 869.2, 150, p. 150. DOI: 10.3847/1538-4357/aaee7a. arXiv: 1811.01963 [astro-ph.GA].

Mayer, L. et al. (2010). "Direct formation of supermassive black holes via multi-scale gas inflows in galaxy mergers". In: *Nature* 466.7310, pp. 1082–1084. DOI: 10.1038/nature09294. arXiv: 0912.4262 [astro-ph.CO].

Mayer, Lucio et al. (2015). "Direct Formation of Supermassive Black Holes in Metal-enriched Gas at the Heart of High-redshift Galaxy Mergers". In: *ApJ* 810.1, 51, p. 51. DOI: 10.1088/0004-637X/810/1/51. arXiv: 1411.5683 [astro-ph.GA].

McKee, C. F. and E. C. Ostriker (2007). "Theory of Star Formation". In: *ARA&A* 45, pp. 565–687. DOI: 10.1146/annurev.astro.45.051806.110602. arXiv: 0707.3514.

McLeod, D. J., R. J. McLure, and J. S. Dunlop (2016). "The z = 9-10 galaxy population in the Hubble Frontier Fields and CLASH surveys: the z = 9 luminosity function and further evidence for a smooth decline in ultraviolet luminosity density at z≥ 8". In: *MNRAS* 459.4, pp. 3812–3824. DOI: 10.1093/mnras/stw904. arXiv: 1602.05199 [astro-ph.GA].

McLure, R. J. et al. (2015). "VizieR Online Data Catalog: Galaxy luminosity function at z = 7-9 (McLure+, 2013)". In: *VizieR Online Data Catalog*, J/MNRAS/432/2696, J/MNRAS/432/2696.

Mehrgan, Kianusch et al. (2019). "A 40 Billion Solar-mass Black Hole in the Extreme Core of Holm 15A, the Central Galaxy of Abell 85". In: *ApJ* 887.2, 195, p. 195. DOI: 10.3847/1538-4357/ab5856. arXiv: 1907.10608 [astro-ph.GA].

Merritt, David, Jeremy D. Schnittman, and S. Komossa (2009). "Hypercompact Stellar Systems Around Recoiling Supermassive Black Holes". In: *ApJ* 699.2, pp. 1690–1710. DOI: 10.1088/0004-637X/699/2/1690. arXiv: 0809.5046 [astro-ph].

Mesinger, A. (2015). *Understanding the Epoch of Cosmic Reionization: Challenges and Progress*. Astrophysics and Space Science Library. Springer Inter-

national Publishing. ISBN: 9783319219578. URL: https://books.google.it/books?id=YtULCwAAQBAJ.

Mesinger, A., A. Ferrara, and D. S. Spiegel (2013). "Signatures of X-rays in the early Universe". In: *MNRAS* 431, pp. 621–637. DOI: 10.1093/mnras/stt198. arXiv: 1210.7319.

Meynet, G. and A. Maeder (2000). "Stellar evolution with rotation. V. Changes in all the outputs of massive star models". In: *A&A* 361, pp. 101–120. eprint: astro-ph/0006404.

— (2005). "Stellar evolution with rotation. XI. Wolf-Rayet star populations at different metallicities". In: *A&A* 429, pp. 581–598. DOI: 10.1051/0004-6361:20047106. eprint: astro-ph/0408319.

Meynet, G. et al. (2006a). "Evolution of rotating stars at very low metallicity". In: *Stellar Evolution at Low Metallicity: Mass Loss, Explosions, Cosmology*. Ed. by H. J. G. L. M. Lamers et al. Vol. 353. Astronomical Society of the Pacific Conference Series, p. 49. eprint: astro-ph/0511446.

Meynet, G., S. Ekström, and A. Maeder (2006b). "The early star generations: the dominant effect of rotation on the CNO yields". In: *A&A* 447, pp. 623–639. DOI: 10.1051/0004-6361:20053070. eprint: astro-ph/0510560.

Mezcua, Mar (2017). "Observational evidence for intermediate-mass black holes". In: *International Journal of Modern Physics D* 26.11, 1730021, p. 1730021. DOI: 10.1142/S021827181730021X. arXiv: 1705.09667 [astro-ph.GA].

Mineo, S., M. Gilfanov, and R. Sunyaev (2012). "X-ray emission from star-forming galaxies - I. High-mass X-ray binaries". In: *MNRAS* 419, pp. 2095–2115. DOI: 10.1111/j.1365-2966.2011.19862.x. arXiv: 1105.4610 [astro-ph.HE].

Mineo, S. et al. (2014). "X-ray emission from star-forming galaxies - III. Calibration of the L_X-SFR relation up to redshift z $\approx$ 1.3". In: *MNRAS* 437.2, pp. 1698–1707. DOI: 10.1093/mnras/stt1999. arXiv: 1207.2157 [astro-ph.HE].

Miyawaki, R. et al. (2009). "Suzaku Observations of M 82 X-1 : Detection of a Curved Hard X-Ray Spectrum". In: *PASJ* 61, S263–S278. DOI: 10.1093/pasj/61.sp1.S263. arXiv: 0809.3339.

Mo, H. J. and S. D. M. White (2002). "The abundance and clustering of dark haloes in the standard ΛCDM cosmogony". In: *MNRAS* 336.1, pp. 112–118. DOI: 10.1046/j.1365-8711.2002.05723.x. arXiv: astro-ph/0202393 [astro-ph].

Mo, H. J., S. Mao, and S. D. M. White (1998). "The formation of galactic discs". In: *MNRAS* 295, pp. 319–336. DOI: 10.1046/j.1365-8711.1998.01227.x. eprint: astro-ph/9707093.

Mo, Houjun, Frank C. van den Bosch, and Simon White (2010). *Galaxy Formation and Evolution*.

Morrison, R. and D. McCammon (1983). "Interstellar photoelectric absorption cross sections, 0.03-10 keV". In: *ApJ* 270, pp. 119–122. DOI: 10.1086/161102.

Mortlock, D. J. et al. (2011). "A luminous quasar at a redshift of z = 7.085". In: *Nature* 474, pp. 616–619. DOI: 10.1038/nature10159. arXiv: 1106.6088 [astro-ph.CO].

Murphy, E. J. (2009). "The Far-Infrared-Radio Correlation at High Redshifts: Physical Considerations and Prospects for the Square Kilometer Array". In: *ApJ* 706, pp. 482–496. DOI: 10.1088/0004-637X/706/1/482. arXiv: 0910.0011.

Murray, S. G., C. Power, and A. S. G. Robotham (2013). "HMFcalc: An online tool for calculating dark matter halo mass functions". In: *Astronomy and Computing* 3, pp. 23–34. DOI: 10.1016/j.ascom.2013.11.001. arXiv: 1306.6721 [astro-ph.CO].

Nagao, Kazutaka, Yoshio Miura, and Masafumi Shirai (2006). "Half-metallicity at the (110) interface between a full Heusler alloy and GaAs". In: *Phys. Rev. B* 73.10, 104447, p. 104447. DOI: 10.1103/PhysRevB.73.104447.

Natarajan, P. (2011). "The formation and evolution of massive black hole seeds in the early Universe". In: *Bulletin of the Astronomical Society of India* 39, pp. 145–161. arXiv: 1104.4797 [astro-ph.CO].

Navarro, J. F., C. S. Frenk, and S. D. M. White (1995). "The assembly of galaxies in a hierarchically clustering universe". In: *MNRAS* 275, pp. 56–66. DOI: 10.1093/mnras/275.1.56. eprint: astro-ph/9408067.

Netzer, H. (1990). "AGN emission lines." In: *Active Galactic Nuclei*. Ed. by R. D. Blandford et al., pp. 57–160.

Netzer, Hagai (2013). "The physics and evolution of active galactic nuclei". In:

Netzer, Hagai (2015). "Revisiting the Unified Model of Active Galactic Nuclei". In: *ARA&A* 53, pp. 365–408. DOI: 10.1146/annurev-astro-082214-122302. arXiv: 1505.00811 [astro-ph.GA].

Ni, Yueying et al. (2020). "QSO obscuration at high redshift (z 7): predictions from the BLUETIDES simulation". In: *MNRAS* 495.2, pp. 2135–2151. DOI: 10.1093/mnras/staa1313. arXiv: 1912.03780 [astro-ph.GA].

Nugis, T. and H. J. G. L. M. Lamers (2000). "Mass-loss rates of Wolf-Rayet stars as a function of stellar parameters". In: *A&A* 360, pp. 227–244.

Oesch, P. A. et al. (2010). "The Evolution of the Ultraviolet Luminosity Function from z ~0.75 to z ~2.5 Using HST ERS WFC3/UVIS Observations". In: *ApJ* 725.2, pp. L150–L155. DOI: 10.1088/2041-8205/725/2/L150. arXiv: 1005.1661 [astro-ph.CO].

Omukai, K. et al. (2005). "Thermal and Fragmentation Properties of Star-forming Clouds in Low-Metallicity Environments". In: *ApJ* 626, pp. 627–643. DOI: 10.1086/429955. eprint: astro-ph/0503010.

Omukai, K., R. Schneider, and Z. Haiman (2008). "Can Supermassive Black Holes Form in Metal-enriched High-Redshift Protogalaxies?" In: *ApJ* 686, 801-814, pp. 801–814. DOI: 10.1086/591636. arXiv: 0804.3141.

Omukai, K., T. Hosokawa, and N. Yoshida (2010). "Low-metallicity Star Formation: Prestellar Collapse and Protostellar Accretion in the Spherical Symmetry". In: *ApJ* 722, pp. 1793–1815. DOI: 10.1088/0004-637X/722/2/1793. arXiv: 1008.4262.

Ono, Yoshiaki et al. (2018). "Great Optically Luminous Dropout Research Using Subaru HSC (GOLDRUSH). I. UV luminosity functions at z $\sim$ 4-7 derived with the half-million dropouts on the 100 deg^2 sky". In: *PASJ* 70, S10, S10. DOI: 10.1093/pasj/psx103. arXiv: 1704.06004 [astro-ph.GA].

Onoue, Masafusa et al. (2017). "Minor Contribution of Quasars to Ionizing Photon Budget at z 6: Update on Quasar Luminosity Function at the Faint End with Subaru/Suprime-Cam". In: *ApJ* 847.2, L15, p. L15. DOI: 10.3847/2041-8213/aa8cc6. arXiv: 1709.04413 [astro-ph.GA].

Orofino, M. C., A. Ferrara, and S. Gallerani (2018a). "Growth problems of stellar black holes in early galaxies". In: *MNRAS* 480, pp. 681–691. DOI: 10.1093/mnras/sty1482.

— (2018b). "Growth problems of stellar black holes in early galaxies". In: *MNRAS* 480.1, pp. 681–691. DOI: 10.1093/mnras/sty1482. arXiv: 1807.05760 [astro-ph.GA].

Pacucci, F. et al. (2014). "The X-ray spectra of the first galaxies: 21 cm signatures". In: *MNRAS* 443, pp. 678–686. DOI: 10.1093/mnras/stu1240. arXiv: 1403.6125.

Pacucci, F. et al. (2016a). "First identification of direct collapse black hole candidates in the early Universe in CANDELS/GOODS-S". In: *MNRAS* 459, pp. 1432–1439. DOI: 10.1093/mnras/stw725. arXiv: 1603.08522.

— (2016b). "First identification of direct collapse black hole candidates in the early Universe in CANDELS/GOODS-S". In: *MNRAS* 459, pp. 1432–1439. DOI: 10.1093/mnras/stw725. arXiv: 1603.08522.

Pacucci, F. et al. (2017). "The nature of the Lyman α emitter CR7: a persisting puzzle". In: *MNRAS* 468, pp. L77–L81. DOI: 10.1093/mnrasl/slx029. arXiv: 1702.04351.

Padmanabhan, T. (1993). *Structure Formation in the Universe*. Cambridge University Press.

Pallottini, A. et al. (2015a). "The brightest Ly α emitter: Pop III or black hole?" In: *MNRAS* 453, pp. 2465–2470. DOI: 10.1093/mnras/stv1795. arXiv: 1506.07173.

— (2015b). "The brightest Ly α emitter: Pop III or black hole?" In: *MNRAS* 453.3, pp. 2465–2470. DOI: 10.1093/mnras/stv1795. arXiv: 1506.07173 [astro-ph.GA].

Pallottini, A. et al. (2017). "Zooming on the internal structure of z =6 galaxies". In: *MNRAS* 465, pp. 2540–2558. DOI: 10.1093/mnras/stw2847. arXiv: 1609.01719.

Park, K. and M. Ricotti (2011). "Accretion onto Intermediate-mass Black Holes Regulated by Radiative Feedback. I. Parametric Study for Spherically Symmetric Accretion". In: *ApJ* 739, 2, p. 2. DOI: 10.1088/0004-637X/739/1/2. arXiv: 1006.1302.

— (2012). "Accretion onto Black Holes from Large Scales Regulated by Radiative Feedback. II. Growth Rate and Duty Cycle". In: *ApJ* 747, 9, p. 9. DOI: 10.1088/0004-637X/747/1/9. arXiv: 1110.4634 [astro-ph.CO].

— (2013a). "Accretion onto Black Holes from Large Scales Regulated by Radiative Feedback. III. Enhanced Luminosity of Intermediate-mass Black Holes Moving at Supersonic Speeds". In: *ApJ* 767, 163, p. 163. DOI: 10.1088/0004-637X/767/2/163. arXiv: 1211.0542.

— (2013b). "Accretion onto Black Holes from Large Scales Regulated by Radiative Feedback. III. Enhanced Luminosity of Intermediate-mass Black Holes Moving at Supersonic Speeds". In: *ApJ* 767, 163, p. 163. DOI: 10.1088/0004-637X/767/2/163. arXiv: 1211.0542.

Park, KwangHo (2012). "Accretion onto Black Holes from Large Scales Regulated by Radiative Feedback". PhD thesis. University of Maryland, College Park.

Parkinson, H., S. Cole, and J. Helly (2008a). "Generating dark matter halo merger trees". In: *MNRAS* 383, pp. 557–564. DOI: 10.1111/j.1365-2966.2007.12517.x. arXiv: 0708.1382.

Parkinson, Hannah, Shaun Cole, and John Helly (2008b). "Generating dark matter halo merger trees". In: *MNRAS* 383.2, pp. 557–564. DOI: 10.1111/j.1365-2966.2007.12517.x. arXiv: 0708.1382 [astro-ph].

Parsa, Shaghayegh, James S. Dunlop, and Ross J. McLure (2018a). "No evidence for a significant AGN contribution to cosmic hydrogen reionization". In: *MNRAS* 474.3, pp. 2904–2923. DOI: 10.1093/mnras/stx2887. arXiv: 1704.07750 [astro-ph.GA].

— (2018b). "No evidence for a significant AGN contribution to cosmic hydrogen reionization". In: *MNRAS* 474.3, pp. 2904–2923. DOI: 10.1093/mnras/stx2887. arXiv: 1704.07750 [astro-ph.GA].

Pensabene, A. et al. (2020). "The ALMA view of the high redshift relation between supermassive black holes and their host galaxies". In: *arXiv e-prints*, arXiv:2002.00958, arXiv:2002.00958. arXiv: 2002.00958 [astro-ph.GA].

Petri, A., A. Ferrara, and R. Salvaterra (2012a). "Supermassive black hole ancestors". In: *MNRAS* 422, pp. 1690–1699. DOI: 10.1111/j.1365-2966.2012.20743.x. arXiv: 1202.3141 [astro-ph.CO].

— (2012b). "Supermassive black hole ancestors". In: *MNRAS* 422.2, pp. 1690–1699. DOI: 10.1111/j.1365-2966.2012.20743.x. arXiv: 1202.3141 [astro-ph.CO].

Pezzulli, E. et al. (2017). "Faint progenitors of luminous z = 6 quasars: Why do not we see them?" In: *MNRAS* 466, pp. 2131–2142. DOI: 10.1093/mnras/stw3243. arXiv: 1612.04188.

Pfister, Hugo et al. (2019). "The erratic dynamical life of black hole seeds in high-redshift galaxies". In: *MNRAS* 486.1, pp. 101–111. DOI: 10.1093/mnras/stz822. arXiv: 1902.01297 [astro-ph.GA].

Piconcelli, E. et al. (2005). "The XMM-Newton view of PG quasars. I. X-ray continuum and absorption". In: *A&A* 432, pp. 15–30. DOI: 10.1051/0004-6361:20041621. eprint: astro-ph/0411051.

Pierre, M. et al. (2016). "The XXL Survey. I. Scientific motivations - XMM-Newton observing plan - Follow-up observations and simulation programme". In: *A&A* 592, A1, A1. DOI: 10.1051/0004-6361/201526766. arXiv: 1512.04317.

Pizzati, Elia et al. (2020). "Outflows and extended [CII] halos in high redshift galaxies". In: *arXiv e-prints*, arXiv:2001.10547, arXiv:2001.10547. arXiv: 2001.10547 [astro-ph.GA].

Planck Collaboration et al. (2016). "Planck 2015 results. XIII. Cosmological parameters". In: *A&A* 594, A13, A13. DOI: 10.1051/0004-6361/201525830. arXiv: 1502.01589.

Planck Collaboration, N. Aghanim, and ... (2018). "Planck 2018 results. VI. Cosmological parameters". In: *arXiv e-prints*, arXiv:1807.06209, arXiv:1807.06209. arXiv: 1807.06209 [astro-ph.CO].

Pontzen, A. and F. Governato (2012). "How supernova feedback turns dark matter cusps into cores". In: *MNRAS* 421, pp. 3464–3471. DOI: 10.1111/j.1365-2966.2012.20571.x. arXiv: 1106.0499.

Pouliasis, E et al. (2020). "An obscured AGN population hidden in the VIPERS galaxies: identification through spectral energy distribution decomposition*". In: *Monthly Notices of the Royal Astronomical Society*. ISSN: 1365-2966. DOI: 10.1093/mnras/staa1263. URL: http://dx.doi.org/10.1093/mnras/staa1263.

Prada, F. et al. (2012). "Halo concentrations in the standard Λ cold dark matter cosmology". In: *MNRAS* 423, pp. 3018–3030. DOI: 10.1111/j.1365-2966.2012.21007.x. arXiv: 1104.5130.

Press, W. H. and P. Schechter (1974). "Formation of Galaxies and Clusters of Galaxies by Self-Similar Gravitational Condensation". In: *ApJ* 187, pp. 425–438. DOI: 10.1086/152650.

Quinlan, G. D. and S. L. Shapiro (1990). "The dynamical evolution of dense star clusters in galactic nuclei". In: *ApJ* 356, pp. 483–500. DOI: 10.1086/168856.

Rees, M. J. (1984). "Black Hole Models for Active Galactic Nuclei". In: *ARA&A* 22, pp. 471–506. DOI: 10.1146/annurev.aa.22.090184.002351.

Regan, John A. et al. (2019). "Super-Eddington accretion and feedback from the first massive seed black holes". In: *MNRAS* 486.3, pp. 3892–3906. DOI: 10.1093/mnras/stz1045. arXiv: 1811.04953 [astro-ph.GA].

Reines, Amy E. and Marta Volonteri (2016). "Relations Between Black Hole Mass and Total Galaxy Stellar Mass in the Local Universe". In: *American Astronomical Society Meeting Abstracts #227*. Vol. 227. American Astronomical Society Meeting Abstracts, p. 119.01.

Rephaeli, Y., D. Gruber, and M. Persic (1995). "X-ray study of starburst galaxies." In: *A&A* 300, p. 91.

Ride, S. K. and A. B. C. Walker Jr. (1977). "Absorption of X-rays in the interstellar medium". In: *A&A* 61, pp. 339–346.

Riechers, D. A. et al. (2009). "Imaging Atomic and Highly Excited Molecular Gas in a z = 6.42 Quasar Host Galaxy: Copious Fuel for an Eddington-limited Starburst at the End of Cosmic Reionization". In: *ApJ* 703, pp. 1338–1345. DOI: 10.1088/0004-637X/703/2/1338. arXiv: 0908.0018 [astro-ph.CO].

Robishaw, T., E. Quataert, and C. Heiles (2008). "Extragalactic Zeeman Detections in OH Megamasers". In: *ApJ* 680, 981-998, pp. 981–998. DOI: 10.1086/588031. arXiv: 0803.1832.

Romero, G.E. and G.S. Vila (2013). *Introduction to Black Hole Astrophysics*. Lecture Notes in Physics. Springer Berlin Heidelberg. ISBN: 9783642395963. URL: https://books.google.it/books?id=sCm6BQAAQBAJ.

Rybicki, G.B. and A.P. Lightman (1979). *Radiative Processes in Astrophysics*. A Wiley-Interscience publication. Wiley. ISBN: 9780471827597. URL: https://books.google.it/books?id=LtdEjNABMlsC.

Salviander, S. et al. (2007). "The Black Hole Mass-Galaxy Bulge Relationship for QSOs in the Sloan Digital Sky Survey Data Release 3". In: *ApJ* 662.1, pp. 131–144. DOI: 10.1086/513086. arXiv: astro-ph/0612568 [astro-ph].

Schindler, Jan-Torge, Xiaohui Fan, and Wolfgang J. Duschl (2016). "Stellar and Black Hole Mass Densities as Empirical Tracers of Co-evolution Show Lock-step Growth since Z 3". In: *ApJ* 826.1, 67, p. 67. DOI: 10.3847/0004-637X/826/1/67. arXiv: 1604.05333 [astro-ph.GA].

Schneider, R. et al. (2003). "Low-mass relics of early star formation". In: *Nature* 422, pp. 869–871. DOI: 10.1038/nature01579. eprint: astro-ph/0304254.

Schneider, R. et al. (2006). "Constraints on the initial mass function of the first stars". In: *MNRAS* 369, pp. 825–834. DOI: 10.1111/j.1365-2966.2006.10331.x. eprint: astro-ph/0510685.

Schneider, R. et al. (2015). "The origin of the far-infrared continuum of z ˜ 6 quasars. A radiative transfer model for SDSS J1148+5251". In: *A&A* 579, A60, A60. DOI: 10.1051/0004-6361/201526105. arXiv: 1402.2279.

Schnittman, Jeremy D. and Alessandra Buonanno (2007). "The Distribution of Recoil Velocities from Merging Black Holes". In: *ApJ* 662.2, pp. L63–L66. DOI: 10.1086/519309. arXiv: astro-ph/0702641 [astro-ph].

Schutz, B.F. (1985). *A First Course in General Relativity*. Series in physics. Cambridge University Press. ISBN: 9780521277037. URL: https://books.google.it/books?id=qhDFuWbLlgQC.

Shankar, Francesco, David H. Weinberg, and Yue Shen (2010). "Constraints on black hole duty cycles and the black hole-halo relation from SDSS quasar clustering". In: *MNRAS* 406.3, pp. 1959–1966. DOI: 10.1111/j.1365-2966.2010.16801.x. arXiv: 1004.1173 [astro-ph.CO].

Shapiro, S. L. (1973). "Accretion onto Black Holes: the Emergent Radiation Spectrum". In: *ApJ* 180, pp. 531–546. DOI: 10.1086/151982.

Shapiro, S. L., S. A. Teukolsky, and Alan P. Lightman (1983). "Black Holes, White Dwarfs, and Neutron Stars: The Physics of Compact Objects". In: *Physics Today* 36.10, p. 89. DOI: 10.1063/1.2915325.

Shen, Xuejian et al. (2020). "The Bolometric Quasar Luminosity Function at z = 0-7". In: *arXiv e-prints*, arXiv:2001.02696, arXiv:2001.02696. arXiv: 2001.02696 [astro-ph.GA].

Sheth, R. K. and G. Tormen (1999). "Large-scale bias and the peak background split". In: *MNRAS* 308, pp. 119–126. DOI: 10.1046/j.1365-8711.1999.02692.x, eprint: astro-ph/9901122.

Sheth, Ravi K., H. J. Mo, and Giuseppe Tormen (2001). "Ellipsoidal collapse and an improved model for the number and spatial distribution of dark matter haloes". In: *MNRAS* 323.1, pp. 1–12. DOI: 10.1046/j.1365-8711.2001.04006.x. arXiv: astro-ph/9907024 [astro-ph].

Shibuya, T. et al. (2017). "SILVERRUSH. III. Deep Optical and Near-Infrared Spectroscopy for Lya and UV-Nebular Lines of Bright Lya Emitters at z=6-7". In: *ArXiv e-prints*. arXiv: 1705.00733.

Shu, Frank H. (1991). "The Physics of Astrophysics: Radiation". In:

Shull, J. M. and M. E. van Steenberg (1985). "X-ray secondary heating and ionization in quasar emission-line clouds". In: *ApJ* 298, pp. 268–274. DOI: 10.1086/163605.

Shvartsman, V. F. (1971). "Halos around "Black Holes"." In: *Soviet Ast.* 15, p. 377.

Smidt, J., B. K. Wiggins, and J. L. Johnson (2016). "Ab Initio Cosmological Simulations of CR7 as an Active Black Hole". In: *ApJ* 829, L6, p. L6. DOI: 10.3847/2041-8205/829/1/L6. arXiv: 1603.00888.

Smith, A., V. Bromm, and A. Loeb (2016). "Evidence for a direct collapse black hole in the Lyman α source CR7". In: *MNRAS* 460, pp. 3143–3151. DOI: 10.1093/mnras/stw1129. arXiv: 1602.07639.

Smith, B. D. et al. (2015). "The first Population II stars formed in externally enriched mini-haloes". In: *MNRAS* 452, pp. 2822–2836. DOI: 10.1093/mnras/stv1509. arXiv: 1504.07639.

Sobral, D. et al. (2015). "Evidence for PopIII-like Stellar Populations in the Most Luminous Lyman-α Emitters at the Epoch of Reionization: Spectroscopic Confirmation". In: *ApJ* 808, 139, p. 139. DOI: 10.1088/0004-637X/808/2/139. arXiv: 1504.01734.

Solomon, P. M. et al. (1987). "Mass, luminosity, and line width relations of Galactic molecular clouds". In: *ApJ* 319, pp. 730–741. DOI: 10.1086/165493.

Souza Lima, R. et al. (2017). "The Pairing of Accreting Massive Black Holes in Multiphase Circumnuclear Disks: the Interplay Between Radiative Cooling, Star Formation, and Feedback Processes". In: *ApJ* 838, 13, p. 13. DOI: 10.3847/1538-4357/aa5d19. arXiv: 1610.01600.

Spitzer Jr., L. (1969). "Equipartition and the Formation of Compact Nuclei in Spherical Stellar Systems". In: *ApJ* 158, p. L139. DOI: 10.1086/180451.

Stark, Daniel P. et al. (2015). "Spectroscopic detection of C IV λ1548 in a galaxy at z = 7.045: implications for the ionizing spectra of reionization-era galaxies". In: *MNRAS* 454.2, pp. 1393–1403. DOI: 10.1093/mnras/stv1907. arXiv: 1504.06881 [astro-ph.GA].

Stefan, I. I. et al. (2015). "Imaging the cold molecular gas in SDSS J1148 + 5251 at z = 6.4". In: *MNRAS* 451, pp. 1713–1718. DOI: 10.1093/mnras/stv1108. arXiv: 1505.07669.

Stevans, Matthew L. et al. (2018). "Bridging Star-forming Galaxy and AGN Ultraviolet Luminosity Functions at z = 4 with the SHELA Wide-field Survey". In: *ApJ* 863.1, 63, p. 63. DOI: 10.3847/1538-4357/aacbd7. arXiv: 1806.05187 [astro-ph.GA].

Sugahara, Yuma et al. (2019). "Fast Outflows Identified in Early Star-forming Galaxies at z=56". In: *ApJ* 886.1, 29, p. 29. DOI: 10.3847/1538-4357/ab49fe. arXiv: 1904.03106 [astro-ph.GA].

Sugimura, K. et al. (2017). "Rapid black hole growth under anisotropic radiation feedback". In: *MNRAS* 469, pp. 62–79. DOI: 10.1093/mnras/stx769. arXiv: 1610.03482.

Sugimura, Kazuyuki and Massimo Ricotti (2020). "Structure and Instability of the Ionization Fronts around Moving Black Holes". In: *arXiv e-prints*, arXiv:2003.05625, arXiv:2003.05625. arXiv: 2003.05625 [astro-ph.GA].

Sugimura, Kazuyuki, Kazuyuki Omukai, and Akio K. Inoue (2014). "The critical radiation intensity for direct collapse black hole formation: dependence on the radiation spectral shape". In: *MNRAS* 445.1, pp. 544–553. DOI: 10.1093/mnras/stu1778. arXiv: 1407.4039 [astro-ph.GA].

Suh, Hyewon et al. (2019). "Multi-wavelength Properties of Type 1 and Type 2 AGN Host Galaxies in the Chandra-COSMOS Legacy Survey". In: *ApJ* 872.2, 168, p. 168. DOI: 10.3847/1538-4357/ab01fb. arXiv: 1902.03244 [astro-ph.GA].

Sur, S. et al. (2010). "The Generation of Strong Magnetic Fields During the Formation of the First Stars". In: *ApJ* 721, pp. L134–L138. DOI: 10.1088/2041-8205/721/2/L134. arXiv: 1008.3481.

Swartz, D. A. et al. (2004). "The Ultraluminous X-Ray Source Population from the Chandra Archive of Galaxies". In: *ApJS* 154, pp. 519–539. DOI: 10.1086/422842. eprint: astro-ph/0405498.

Tagawa, H., M. Umemura, and N. Gouda (2016). "Mergers of accreting stellar-mass black holes". In: *MNRAS* 462, pp. 3812–3822. DOI: 10.1093/mnras/stw1877. arXiv: 1602.08767.

Takeo, Eishun, Kohei Inayoshi, and Shin Mineshige (2020). "Hyper-Eddington accretion flows onto black holes accompanied by powerful outflows". In: *arXiv e-prints*, arXiv:2002.07187, arXiv:2002.07187. arXiv: 2002.07187 [astro-ph.HE].

Tamburello, V. et al. (2017a). "Supermassive black hole pairs in clumpy galaxies at high redshift: delayed binary formation and concurrent mass growth". In: *MNRAS* 464, pp. 2952–2962. DOI: 10.1093/mnras/stw2561. arXiv: 1603.00021.

Tamburello, Valentina et al. (2017b). "Supermassive black hole pairs in clumpy galaxies at high redshift: delayed binary formation and concurrent mass growth". In: *MNRAS* 464.3, pp. 2952–2962. DOI: 10.1093/mnras/stw2561. arXiv: 1603.00021 [astro-ph.GA].

Tanaka, Takamitsu and Zoltán Haiman (2009). "The Assembly of Supermassive Black Holes at High Redshifts". In: *ApJ* 696.2, pp. 1798–1822. DOI: 10.1088/0004-637X/696/2/1798. arXiv: 0807.4702 [astro-ph].

Tanaka, Takamitsu L. (2014). "Driving the growth of the earliest supermassive black holes with major mergers of host galaxies". In: *Classical and Quantum Gravity* 31.24, 244005, p. 244005. DOI: 10.1088/0264-9381/31/24/244005. arXiv: 1406.3023 [astro-ph.GA].

Targett, Thomas A., James S. Dunlop, and Ross J. McLure (2012). "The host galaxies and black hole-to-galaxy mass ratios of luminous quasars at z 4". In: *MNRAS* 420.4, pp. 3621–3631. DOI: 10.1111/j.1365-2966.2011.20286.x. arXiv: 1107.2397 [astro-ph.CO].

Thorne, K. S. (1974). "Disk-Accretion onto a Black Hole. II. Evolution of the Hole". In: *ApJ* 191, pp. 507–520. DOI: 10.1086/152991.

Toomre, A. (1963). "On the Distribution of Matter Within Highly Flattened Galaxies." In: *ApJ* 138, p. 385. DOI: 10.1086/147653.

Toyouchi, Daisuke et al. (2020). "Gaseous dynamical friction under radiative feedback: do intermediate-mass black holes speed up or down?" In: *arXiv e-prints*, arXiv:2002.08017, arXiv:2002.08017. arXiv: 2002.08017 [astro-ph.GA].

Trebitsch, Maxime, Marta Volonteri, and Yohan Dubois (2019a). "Black hole obscuration and duty-cycles mediated by AGN feedback in high-redshift galaxies". In: *MNRAS* 487.1, pp. 819–831. DOI: 10.1093/mnras/stz1280. arXiv: 1901.01261 [astro-ph.GA].

Trebitsch, Maxime, Marta Volonteri, and Yohan Dubois (2019b). "Black hole obscuration and duty-cycles mediated by AGN feedback in high-redshift galaxies". In: *MNRAS* 487.1, pp. 819–831. DOI: 10.1093/mnras/stz1280. arXiv: 1901.01261 [astro-ph.GA].

Trebitsch, Maxime, Marta Volonteri, and Yohan Dubois (2020). *Modelling a bright $z = 6$ galaxy at the faint end of the AGN luminosity function*. arXiv: 2004.03611 [astro-ph.GA].

Treister, E. et al. (2013). "New Observational Constraints on the Growth of the First Supermassive Black Holes". In: *ApJ* 778, 130, p. 130. DOI: 10.1088/0004-637X/778/2/130. arXiv: 1310.2249.

Turner, M. S. and L. M. Widrow (1988). "Inflation-produced, large-scale magnetic fields". In: *Phys. Rev. D* 37, pp. 2743–2754. DOI: 10.1103/PhysRevD.37.2743.

Valdés, M. et al. (2007). "Constraining dark matter through 21-cm observations". In: *MNRAS* 377, pp. 245–252. DOI: 10.1111/j.1365-2966.2007.11594.x. eprint: astro-ph/0701301.

Valiante, R. et al. (2011). "The origin of the dust in high-redshift quasars: the case of SDSS J1148+5251". In: *MNRAS* 416, pp. 1916–1935. DOI: 10.1111/j.1365-2966.2011.19168.x. arXiv: 1106.1418.

Vietri, M. (2006). *Astrofisica delle alte energie*. Programma di matematica, fisica, elettronica. Bollati Boringhieri. ISBN: 9788833957739. URL: https://books.google.it/books?id=Qd5tAAAACAAJ.

Visbal, E., Z. Haiman, and G. L. Bryan (2016). "Formation of massive Population III galaxies through photoionization feedback: a possible explanation for CR 7". In: *MNRAS* 460, pp. L59–L63. DOI: 10.1093/mnrasl/slw071. arXiv: 1602.04843.

Vishniac, E. T. (1978). "A necessary condition for equilibrium in stellar systems with a continuous mass spectrum". In: *ApJ* 223, pp. 986–990. DOI: 10.1086/156332.

Vito, F. et al. (2016). "The deepest X-ray view of high-redshift galaxies: constraints on low-rate black hole accretion". In: *MNRAS* 463, pp. 348–374. DOI: 10.1093/mnras/stw1998. arXiv: 1608.02614.

Vito, F. et al. (2018). "High-redshift AGN in the Chandra Deep Fields: the obscured fraction and space density of the sub-L_* population". In: *MNRAS* 473.2, pp. 2378–2406. DOI: 10.1093/mnras/stx2486. arXiv: 1709.07892 [astro-ph.GA].

Volonteri, M. (2010a). "Formation of supermassive black holes". In: *A&A Rev.* 18, pp. 279–315. DOI: 10.1007/s00159-010-0029-x. arXiv: 1003.4404.

— (2010b). "Formation of supermassive black holes". In: *A&A Rev.* 18, pp. 279–315. DOI: 10.1007/s00159-010-0029-x. arXiv: 1003.4404.

Volonteri, M. and J. Bellovary (2012). "Black holes in the early Universe". In: *Reports on Progress in Physics* 75.12, 124901, p. 124901. DOI: 10.1088/0034-4885/75/12/124901. arXiv: 1209.2243.

Volonteri, M. and D. P. Stark (2011). "Assessing the redshift evolution of massive black holes and their hosts". In: *MNRAS* 417, pp. 2085–2093. DOI: 10.1111/j.1365-2966.2011.19391.x. arXiv: 1107.1946.

Volonteri, M., F. Haardt, and P. Madau (2003a). "The Assembly and Merging History of Supermassive Black Holes in Hierarchical Models of Galaxy Formation". In: *ApJ* 582, pp. 559–573. DOI: 10.1086/344675. eprint: astro-ph/0207276.

Volonteri, M., P. Madau, and F. Haardt (2003b). "The Formation of Galaxy Stellar Cores by the Hierarchical Merging of Supermassive Black Holes". In: *ApJ* 593, pp. 661–666. DOI: 10.1086/376722. eprint: astro-ph/0304389.

Volonteri, M., J. Silk, and G. Dubus (2015). "The Case for Supercritical Accretion onto Massive Black Holes at High Redshift". In: *ApJ* 804, 148, p. 148. DOI: 10.1088/0004-637X/804/2/148. arXiv: 1401.3513.

Volonteri, M. et al. (2016). "The cosmic evolution of massive black holes in the Horizon-AGN simulation". In: *MNRAS* 460.3, pp. 2979–2996. DOI: 10.1093/mnras/stw1123. arXiv: 1602.01941 [astro-ph.GA].

Volonteri, Marta and Martin J. Rees (2006). "Quasars at z=6: The Survival of the Fittest". In: *ApJ* 650.2, pp. 669–678. DOI: 10.1086/507444. arXiv: astro-ph/0607093 [astro-ph].

Volonteri, Marta et al. (2017a). "High-redshift Galaxies and Black Holes Detectable with the JWST: A Population Synthesis Model from Infrared to X-Rays". In: *ApJ* 849.2, 155, p. 155. DOI: 10.3847/1538-4357/aa93f1. arXiv: 1704.00753 [astro-ph.GA].

Volonteri, Marta et al. (2017b). "High-redshift Galaxies and Black Holes Detectable with the JWST: A Population Synthesis Model from Infrared to X-Rays". In: *ApJ* 849.2, 155, p. 155. DOI: 10.3847/1538-4357/aa93f1. arXiv: 1704.00753 [astro-ph.GA].

Walter, F. et al. (2003). "Molecular gas in the host galaxy of a quasar at redshift z = 6.42". In: *Nature* 424, pp. 406–408. DOI: 10.1038/nature01821. eprint: astro-ph/0307410.

Walter, F. et al. (2004). "Resolved Molecular Gas in a Quasar Host Galaxy at Redshift z=6.42". In: *ApJ* 615, pp. L17–L20. DOI: 10.1086/426017. eprint: astro-ph/0410229.

Wang, Ran et al. (2010). "Molecular Gas in z ~6 Quasar Host Galaxies". In: *ApJ* 714.1, pp. 699–712. DOI: 10.1088/0004-637X/714/1/699. arXiv: 1002.1561 [astro-ph.CO].

Weigel, A. K. et al. (2015). "The systematic search for z $\gtrsim$ 5 active galactic nuclei in the Chandra Deep Field South". In: *MNRAS* 448, pp. 3167–3195. DOI: 10.1093/mnras/stv184. arXiv: 1501.06580.

Weingartner, Joseph C. and B. T. Draine (2001). "Dust Grain-Size Distributions and Extinction in the Milky Way, Large Magellanic Cloud, and Small Magellanic Cloud". In: *ApJ* 548.1, pp. 296–309. DOI: 10.1086/318651. arXiv: astro-ph/0008146 [astro-ph].

Wheeler, J. C. and V. Johnson (2011). "Stellar-mass Black Holes in Young Galaxies". In: *ApJ* 738, 163, p. 163. DOI: 10.1088/0004-637X/738/2/163. arXiv: 1107.3165.

White, R. L. et al. (2003). "Probing the Ionization State of the Universe at z¿6". In: *AJ* 126, pp. 1–14. DOI: 10.1086/375547. eprint: astro-ph/0303476.

Willott, C. J., R. J. McLure, and M. J. Jarvis (2003). "A $3 \times 10^9 M_{solar}$ Black Hole in the Quasar SDSS J1148+5251 at z=6.41". In: *ApJ* 587, pp. L15–L18. DOI: 10.1086/375126. eprint: astro-ph/0303062.

Willott, C. J. et al. (2007a). "Four Quasars above Redshift 6 Discovered by the Canada-France High-z Quasar Survey". In: *AJ* 134, pp. 2435–2450. DOI: 10.1086/522962. arXiv: 0706.0914.

Willott, C. J. et al. (2010). "Eddington-limited Accretion and the Black Hole Mass Function at Redshift 6". In: *AJ* 140, pp. 546–560. DOI: 10.1088/0004-6256/140/2/546. arXiv: 1006.1342.

Willott, Chris J. et al. (2007b). "Four Quasars above Redshift 6 Discovered by the Canada-France High-z Quasar Survey". In: *AJ* 134.6, pp. 2435–2450. DOI: 10.1086/522962. arXiv: 0706.0914 [astro-ph].

Willott, Chris J., Jacqueline Bergeron, and Alain Omont (2015). "Star Formation Rate and Dynamical Mass of 10^8 Solar Mass Black Hole Host Galaxies At Redshift 6". In: *ApJ* 801.2, 123, p. 123. DOI: 10.1088/0004-637X/801/2/123. arXiv: 1501.07538 [astro-ph.GA].

Wu, X.-B. et al. (2015). "An ultraluminous quasar with a twelve-billion-solar-mass black hole at redshift 6.30". In: *Nature* 518, pp. 512–515. DOI: 10.1038/nature14241. arXiv: 1502.07418.

Xue, Y. Q. et al. (2011). "The Chandra Deep Field-South Survey: 4 Ms Source Catalogs". In: *ApJS* 195, 10, p. 10. DOI: 10.1088/0067-0049/195/1/10. arXiv: 1105.5643.

Yaqoob, T. (1997). "X-Ray Transmission in Cold Matter: Nonrelativistic Corrections for Compton Scattering". In: *ApJ* 479, pp. 184–189.

Yue, B. et al. (2015). "Intensity mapping of [C II] emission from early galaxies". In: *MNRAS* 450, pp. 3829–3839. DOI: 10.1093/mnras/stv933. arXiv: 1504.06530.

Yue, Bin et al. (2014). "The brief era of direct collapse black hole formation". In: *MNRAS* 440.2, pp. 1263–1273. DOI: 10.1093/mnras/stu351. arXiv: 1402.5675 [astro-ph.CO].

Zel'dovich, Y. B. and I. D. Novikov (1971). *Theory of gravitation and the evolution of stars.*